NOAA Technical Memorandum ERL AL-12

HEAT AND MOMENTUM FLUX MEASUREMENTS IN THE PLANETARY BOUNDARY LAYER WITH A WIND PROFILING RADAR/RADIO ACOUSTIC SOUNDING SYSTEM

Wayne M. Angevine

Aeronomy Laboratory
Boulder, Colorado
January 1994

noaa NATIONAL OCEANIC AND ATMOSPHERIC ADMINISTRATION / Environmental Research Laboratories

NOAA Technical Memorandum ERL AL-12

HEAT AND MOMENTUM FLUX MEASUREMENTS IN THE PLANETARY BOUNDARY LAYER WITH A WIND PROFILING RADAR/RADIO ACOUSTIC SOUNDING SYSTEM

Wayne M. Angevine

Cooperative Institute for Research in Environmental Sciences
University of Colorado
Boulder, Colorado

Aeronomy Laboratory
Boulder, Colorado
January 1994

UNITED STATES
DEPARTMENT OF COMMERCE

Ronald H. Brown
Secretary

NATIONAL OCEANIC AND
ATMOSPHERIC ADMINISTRATION

D. James Baker
Under Secretary for Oceans
and Atmosphere/Administrator

Environmental Research
Laboratories

Alan R. Thomas
Director

NOTICE

Mention of a commercial company or product does not constitute an endorsement by NOAA/ERL. Use of information from this publication concerning proprietary products or the tests of such products for publicity or advertising purposes is not authorized.

For sale by the National Technical Information Service, 5285 Port Royal Road
Springfield, VA 22161

Table of Contents

Table of Tables

Table of Figures

Heat and Momentum Flux Measurements in the Planetary Boundary Layer with a Wind Profiling Radar / Radio Acoustic Sounding System

Wayne M. Angevine
Cooperative Institute for Research in Environmental Sciences

Abstract:

The planetary or atmospheric boundary layer is the lowest 100 - 2000 m of the atmosphere, and contains the sources of most energy and pollutants that affect the entire atmosphere. Boundary-layer structure and dynamics are key to understanding, modeling, and predicting climate, weather, and pollution. New and improved techniques for measuring the dynamics of the boundary layer are needed. One of the most important needs is for improved methods of measuring the turbulent fluxes of heat and momentum. Existing methods involving towers, surface measurements, or aircraft have limited flexibility or are expensive.

This memorandum describes methods for measuring heat flux (virtual temperature flux) and momentum flux in convective boundary layers. The instrument used is the 915 MHz boundary-layer radar wind profiler radio acoustic sounding system (profiler/RASS). As the name suggests, the profiler was developed to make wind measurements, and this work is an expansion of its capabilities. The radio acoustic sounding system uses the profiler and attachments to measure virtual temperature.

Before the profiler/RASS could be used to make flux measurements, the ability to make simultaneous measurements of wind velocity and temperature had to be developed. A feasibility study was conducted at Platteville, Colorado, in June 1991 to determine if flux measurements were a practical application of the profiler, with encouraging results. The Rural Oxidants in the Southern Environment II (ROSE II) experiment in Alabama in June 1992 provided the opportunity to compare flux measurements from the profiler/RASS to those made by a surface sonic anemometer and an aircraft, the National Center for Atmospheric Research (NCAR) King Air.

The results indicate that the profiler/RASS is capable of making heat flux measurements that compare well with aircraft and surface measurements. The primary limitation on the precision of the measurements is the sampling uncertainty of the turbulence, a limitation that is the same for any fixed instrument. The feasibility of making momentum flux measurements needs to be explored further in more favorable conditions. In the course of analyzing the flux measurements, methods of determining the mixing depth (boundary layer height) and improved data quality control techniques were developed.

1. Introduction

The planetary or atmospheric boundary layer (PBL) is "that part of the troposphere that is directly influenced by the presence of the earth's surface, and responds to surface forcings with a timescale of about an hour or less," (Stull, 1988, p.2) or "the turbulent region adjacent to the earth's surface" (Wyngaard, 1986). Much of the energy in the atmosphere has its source within the PBL, due to solar heating of the surface, evaporation of surface moisture, and turbulent interaction of the wind with surface irregularities. Understanding the energy budget in the PBL is therefore vital to any effort to understand or model the atmosphere as a whole for weather and climate prediction. Most sources and sinks of pollutant species are also at the surface, and the PBL mediates pollutant transport between the free atmosphere and those sources and sinks.

Heat and momentum fluxes are key terms in the PBL energy budget, but current methods for measuring them are not completely satisfactory: Surface measurements may not be representative of large areas; meteorological towers are expensive, difficult to site, and inflexible; aircraft are expensive, suffer from short endurance, and can only measure one height at a time. On the other hand, remote sensing of fluxes could provide continuous measurements over a range of heights at relatively low cost for field campaigns and long-term monitoring.

This memorandum reports results of a study on the measurement of heat and momentum fluxes in the atmospheric boundary layer with a boundary-layer wind profiler radio acoustic sounding system (profiler/RASS). The objective was to answer the following questions:

1. Is it possible to measure the fluxes of heat and momentum with this instrument?

2. What technique is best used for making such measurements?

3. What are the limitations of the instrument and technique?

The answers to these questions can be stated briefly here. It is possible to measure heat flux with the profiler/RASS using the techniques described herein. The feasibility of momentum flux measurements is not established, but the measurements reported here were conducted under unfavorable conditions. The major limitation of the instrument and technique is that flux measurements cannot be made in precipitation. The nature of turbulence itself and the uncertainties associated with sampling are also important limitations, but are shared with all other fixed instruments.

In the course of the study, other techniques were also explored and developed. In particular, the use of the profiler to determine the height of the boundary layer was important for normalization of the flux measurements, and has other applications as well. Considerable effort also went into the development of data quality control techniques.

The remainder of this memorandum is organized as follows: In chapter 2 we review the

characteristics of the planetary (atmospheric) boundary layer and of turbulence, explore terminology, and discuss results of previous studies. In chapter 3 we describe the profiler and RASS used in the study. Data analysis and quality control procedures are discussed in chapter 4. In chapter 5 we report the results of preliminary flux measurements made at Platteville, Colorado. The heart of the work is found in chapter 6, where we discuss measurements made at the Rural Oxidants in the Southern Environment II (ROSE II) experiment and compare the fluxes measured by the profiler/RASS to those measured by aircraft and by surface instruments. We then summarize the conclusions of this work in chapter 7.

2. The Boundary Layer, Fluxes and Turbulence

In this chapter we describe the planetary or atmospheric boundary layer, define the fluxes of heat and momentum, explore terminology, and discuss previous remote-sensing measurements of boundary layer fluxes. We also discuss turbulence theory and its implications for the uncertainty of turbulence measurements.

2.1 Boundary layer definition and characteristics

In chapter 1, we introduced the atmospheric boundary layer as "that part of the troposphere that is directly influenced by the presence of the earth's surface, and responds to surface forcings with a timescale of about an hour or less," (Stull, 1988) and as "the turbulent region adjacent to the earth's surface" (Wyngaard, 1986). This region is also called the planetary boundary layer. Boundary layers may be described by several other terms, depending on their location, the time of year, and the time of day. For example, nocturnal, stable, and marine boundary layers are all discussed in the literature. This study is primarily concerned with the boundary layer as it exists in the summer in fair weather with light winds over a continental surface, and we call this a convective continental boundary layer (CBL).

Depending on the season and on the amount of cloud present, the convective boundary layer varies in thickness from a few hundred to a few thousand meters. The temperature lapse rate is near neutral or slightly superadiabatic, and the water vapor mixing ratio is nearly constant with height. The boundary layer is usually capped by a temperature inversion. As we will see in chapter 6, the CBL top is not always well defined, particularly in the presence of clouds or under synoptic low pressure conditions. The top of the boundary layer may be detected by several means in practice, not all of which give the same estimate of height. In sonde data, a sharp decrease in mixing ratio or an increase in temperature lapse rate indicates the CBL top. It may also be detected by a peak in the reflectivity measured by a clear-air radar as described in chapter 6 below. If good measurements of turbulence statistics such as vertical velocity variance or heat flux throughout the CBL are available, the CBL top may be detected from the profiles of those quantities.

Figure 2.1 is an actual sounding from the ROSE II experiment with the boundary layer structure nomenclature indicated. We show the virtual potential temperature because it directly indicates the stability of the air. The top of the convective boundary layer (CBL) is defined as z_i, standing for *inversion height*. Starting at the ground, the CBL is made up of a *surface layer* to approximately $0.1z_i$, a *mixed layer* from approximately 0.1 to 0.8 z_i, and an *entrainment zone* from approximately 0.8 to 1.2 z_i. The entrainment zone is also called the *interfacial layer* (Wyngaard and LeMone, 1980.) The top and bottom of the entrainment zone are denoted by h_2 and h_0, respectively. Above the CBL is the *free troposphere*. The overlying inversion may be strong or weak, and in some cases the top of the CBL may be very difficult to define.

At night, the CBL is replaced by a *stable* or *nocturnal* boundary layer. The height of the

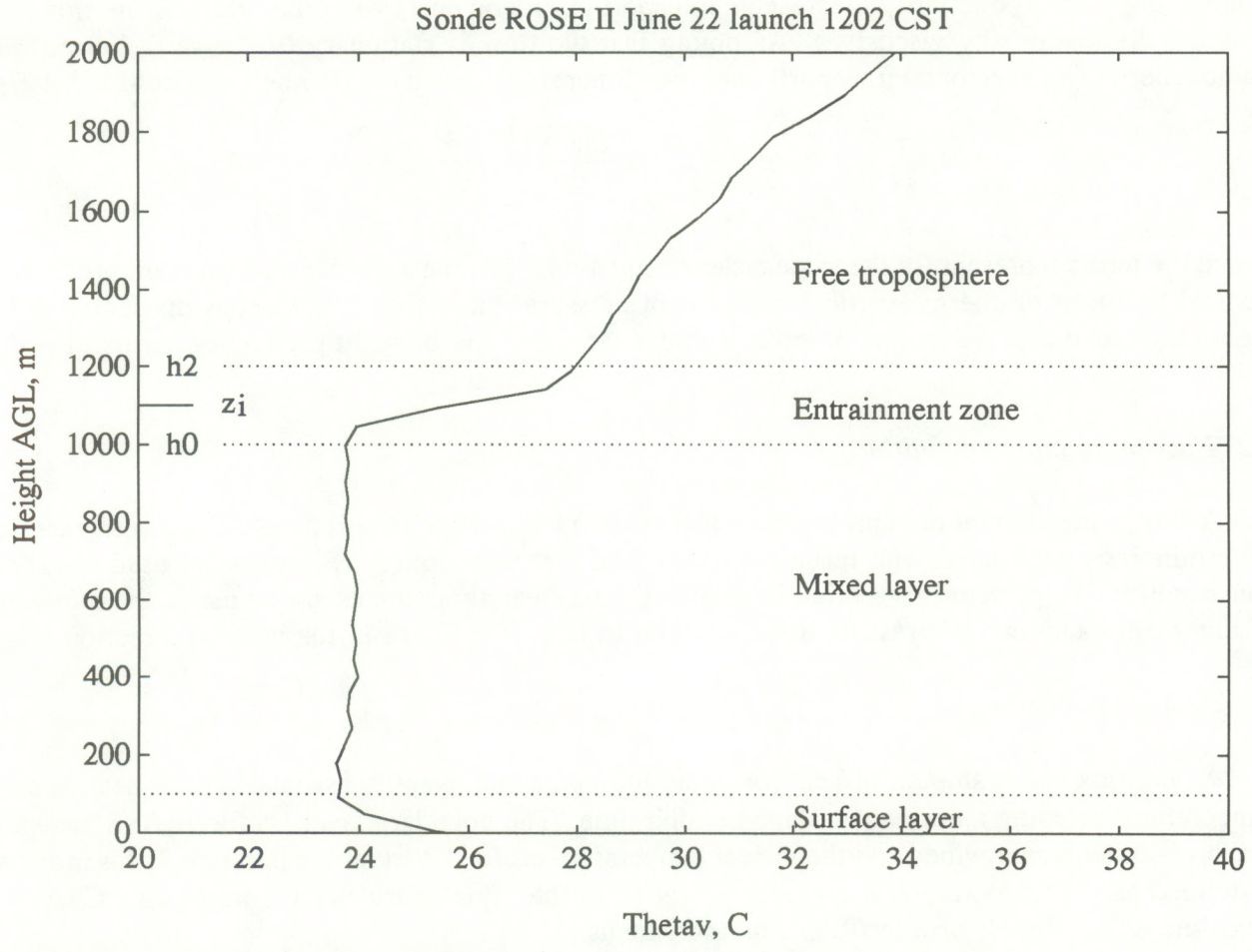

Figure 2.1: Sounding from ROSE II with convective boundary layer nomenclature.

nocturnal boundary layer is generally 100-200 m, and the turbulence is caused by wind shear or interaction of wind with surface roughness. After sunrise, the CBL forms and grows rapidly through the morning. The growth may continue into the afternoon or the CBL height may stabilize, depending on the synoptic conditions and the amount of surface heat flux. Sometime in the afternoon, the surface heat flux becomes insufficient to support the CBL, and the turbulence decays.

The boundary layer is the source of much of the energy of the total atmospheric system. If we hope to understand that system, we must therefore understand the production and consumption of energy in the PBL. Processes that produce and consume turbulent kinetic energy can be combined to produce a budget. It is described in general terms by (Arya 1988):

$$\frac{dE}{dt} = S + B + T_r - D \qquad (2.1)$$

where dE/dt is the time rate of change of the turbulence kinetic energy, S is the shear production,

B is the buoyant production, T_r represents transport of kinetic energy to other parts of the flow, and D is the dissipation (by viscosity.) Assuming that the flow is stationary ($dE/dt = 0$), horizontally homogeneous (no horizontal transport), and two-dimensional, we have (Pennell and LeMone, 1974):

$$- \overline{u'w'} \frac{\partial \overline{U}}{\partial z} + \frac{g}{T_v} \overline{w'T_v'} - \frac{\partial \overline{w'e'}}{\partial z} - \frac{\partial}{\partial z} \frac{\overline{w'p'}}{\rho} - \epsilon = 0 \qquad (2.2)$$

where the terms represent (in the same order as equation 2.1): shear production, buoyant production, vertical transport of energy, vertical transport of pressure fluctuation, and viscous dissipation. The measurements discussed in this proposal address the shear and buoyant production terms directly.

2.2 Flux terminology definitions

A flux is the amount of some quantity that crosses a boundary in unit time. There is a great deal of terminology associated with turbulent fluxes, and that terminology is not always used clearly or consistently. We present this section in an effort to be clear about the terms we use in the remainder of this memorandum. We restrict the discussion to turbulent fluxes in the vertical direction.

2.2.1 Heat fluxes

A heat flux is the amount of heat (or, more loosely, some quantity associated with heat, such as temperature) crossing a horizontal plane per unit time. The boundary layer profiler/RASS measures the three-dimensional winds and the virtual temperature profile. Virtual temperature T_v for moist air is defined as the temperature of a parcel of dry air at the same density as the moist air. Chapter 3 gives the details of the profiler/RASS measurements.

Traditionally, three turbulent fluxes associated with heat are defined, the sensible heat flux, latent heat flux, and buoyancy flux. For vertical fluxes, the definitions are:

$$\begin{array}{ll} \rho C_p \overline{w'T'} & \textit{Sensible heat flux} \\ \rho L_v \overline{w'q'} & \textit{Latent heat flux} \\ \frac{g}{T_v} \overline{w'T_v'} & \textit{Buoyancy flux} \end{array} \qquad (2.3)$$

where w' is the perturbation of vertical velocity, T' the perturbation of temperature, T_v' the perturbation of virtual temperature, ρ the air density, C_p the specific heat of air at constant pressure, and L_v the heat of vaporization of water. These fluxes also appear in kinematic form (Stull, 1988):

$$\begin{array}{ll} \overline{w'T'} & \textit{Kinematic sensible heat flux} \\ \overline{w'q'} & \textit{Moisture flux} \\ \overline{w'T_v'} & \textit{Virtual temperature flux} \end{array} \qquad (2.4)$$

The virtual temperature flux might also be called "kinematic buoyancy flux." The kinematic forms

use only the quantities measured in practice, that is, temperatures and wind speeds, and are free from any assumptions about other variables such as the specific heat or air density. In this memorandum, we will use the term "virtual temperature flux" defined as

$$Q_t = \overline{w'T_v'} \tag{2.5}$$

In previous publications (Angevine et al., 1993a,b), we have used the term "virtual heat flux" (Arya 1988, p.187), defined as

$$Q_v = \rho C_p \overline{w'T_v'} \tag{2.6}$$

This term retains a connection to the sensible heat flux measured by traditional ground- or aircraft-based instruments, and keeps the more intuitive units of watts per square meter.

The fluxes containing the virtual temperature are more useful than sensible and latent heat fluxes for studies of boundary layer dynamics because the virtual temperature is related to density and therefore to buoyancy, which drives convective mixing. The virtual temperature flux appears directly in the kinetic energy budget (equation 2.2).

The canonical profile of virtual temperature flux in the convective mixed layer shows a linear decrease from a maximum at the surface to about $0.8z_i$. This profile is seen in both observations (Stull, 1988 pp.99-101) as well as models (Moeng, 1984). Stull (1988, p.370) proposes the following empirical relationship between normalized virtual temperature flux and normalized height:

$$\frac{Q_t}{Q_{ts}} = 1 - \alpha \frac{z}{z_i} \tag{2.7}$$

where Q_t is the virtual temperature flux at height z, Q_{ts} is the surface virtual temperature flux, and α is a constant between 1.2 and 1.5.

2.2.2 Momentum flux

The momentum flux is the amount of momentum crossing a horizontal plane per unit time. The vertical turbulent flux of horizontal momentum is

$$\rho \overline{u'w'} \tag{2.8}$$

where u' and w' are the perturbations of horizontal and vertical velocity, respectively. As for the heat fluxes, we prefer to use the simpler kinematic form

$$F = \overline{u'w'}. \tag{2.9}$$

2.3 *Scaling*

Boundary layer data are customarily presented in scaled form, that is, normalized to suitable combinations of variables in order to reduce scatter in the measurements and to show fundamental relationships more clearly. Equation 2.7 above is an example of scaling. Where appropriate in chapters 5 and 6, we have used a simple mixed-layer scaling (Stull, 1988, p. 369). Virtual temperature fluxes were scaled to the surface virtual temperature flux. Momentum fluxes were scaled to the surface momentum flux. In addition, the measurement heights were scaled to the boundary layer height for some of the comparisons.

2.4 *Turbulence theory and basic observations*

The boundary layer is defined by turbulent mixing. The following brief review of points directly relevant to the measurements we present in this memorandum is based on discussions by Wyngaard (1986) and Arya (1988). The sizes of turbulent structures are particularly important in planning and interpreting PBL measurements.

Turbulence can be thought of as a superposition of eddies with a continuous spectrum of sizes. The spectrum is divided into three regions, the *energy-containing* or *input* subrange, the *inertial* subrange, and the *viscous* or *dissipative* subrange.

The energy-containing subrange is from the largest eddies present down to an ill-defined boundary somewhere below the integral scale. The integral scale is the integral of the autocorrelation of the turbulence, and is a measure of the correlation distance. Eddies in the energy-containing subrange carry the fluxes of heat and momentum (Priestly 1959). Lenschow and Stankov (1986) investigated the integral scale for fluxes in the convective boundary layer and found that the heat flux integral scale is

$$\lambda_{wT} = 0.16 z^{\frac{1}{3}} z_i^{\frac{2}{3}} \qquad (2.10)$$

the integral scale for momentum flux is

$$\lambda_{wu} = 0.12 z^{\frac{1}{3}} z_i^{\frac{2}{3}} \qquad (2.11)$$

and the integral scale for vertical velocity variance is

$$\lambda_{w^2} = 0.16 z^{\frac{1}{2}} z_i^{\frac{1}{2}} \qquad (2.12)$$

In the energy-containing subrange buoyant or shear instability produce large eddies, which then produce smaller eddies cascading down the scale until they are damped by viscosity.

The smallest eddies are in the viscous subrange. The larger end of this range is the size at which viscous effects begin to be important, which is taken to be the Taylor microscale

$$\lambda_T = (\nu q^2/\epsilon)^{1/2} \qquad (2.13)$$

where ν is the kinematic viscosity, q^2 here is the turbulence kinetic energy per unit mass, and ϵ is the turbulence dissipation rate per unit mass. In typical convective daytime conditions, λ_T is of the order of 0.1 m.

Intermediate eddy sizes are in the inertial subrange. In this range turbulent energy is neither created nor destroyed. The distinctive feature of this subrange is that the energy goes as the 5/3 power of the eddy size.

The radar wind profiler, and indeed most instruments except those on aircraft, makes a series of measurements in time at a fixed location rather than sampling spatially as the above discussion would indicate. To convert from space to time variation, the Taylor hypothesis is commonly invoked. This hypothesis is that the turbulent field is "frozen" and is advected past the instrument by the mean wind. Thus for distance in the above discussion we may substitute time multiplied by mean wind velocity. This substitution is valid in the limit as the mean wind becomes very much larger than the turbulent velocity components, but may be problematic otherwise. For example, thermals often are "attached" to terrain features and are not advected at all over some period of time. There is no known alternative that can be substituted for this assumption.

In practical terms for this study, the above discussion tells us that most of the fluxes will be carried by eddies whose sizes are within an order of magnitude of the boundary layer depth z_i. The ideal instrument for flux measurements would be able to measure fluctuations on scales of the order of ten to ten thousand meters. The boundary-layer winds will usually be of the order of several meters per second, so the time scales of interest will be one to ten thousand seconds (about three hours.)

2.5 Sampling uncertainty

Any turbulence measurement is subject to a fundamental uncertainty due to sampling. This uncertainty due to sampling of turbulence has been addressed theoretically by Wyngaard (1992) and

experimentally by Lenschow and Stankov (1986). The relative uncertainty is given by:

$$e^2 = \frac{2F\tau}{t} \tag{2.14}$$

or

$$e^2 = \frac{2F\lambda}{L} \tag{2.15}$$

where e is the relative uncertainty (the ratio of the standard deviation of the measurement to the mean), τ is the integral scale in time and λ the integral scale in space of the flux, t is the sampling time and L the sampling distance, and

$$F = \frac{\overline{T_v'^2}\ \overline{w'^2} + \left(\overline{T_v'w'}\right)^2}{\left(\overline{T_v'w'}\right)^2} \tag{2.16}$$

for heat flux,

$$F = \frac{\overline{u'^2}\ \overline{w'^2} + \left(\overline{u'w'}\right)^2}{\left(\overline{u'w'}\right)^2} \tag{2.17}$$

for momentum flux, and

$$F = 2 \tag{2.18}$$

for variances.

We shall refer to these equations regularly in the discussion of results in chapters 5 and 6. For the moment, note that to reduce the sampling uncertainty, we must increase the averaging time.

2.6 Previous boundary layer measurements

In this section, we briefly summarize some recent published measurements of fluxes in the boundary layer by remote sensors. For a comprehensive review, the reader should consult Stull (1988).

Rabin et al. (1982) reported measurements with dual Doppler radars in a cloudless convective boundary layer in Oklahoma. They found mean momentum fluxes of about 0.2 m^2s^{-2} in winds of about 15 m/s. Kropfli (1986) made measurements of the momentum flux in the convective boundary layer in Colorado with single X- and K-band Doppler radars. Average values of the flux over 70 minutes were reported to be 0.5 to 1 m^2s^{-2}. The mean winds were around 5 m/s.

Measurements with a single K-band Doppler radar were reported by Xu and Gal-Chen (1991) from an experiment in Colorado in the summer of 1984. They reported values for the momentum flux over intervals of about 30 minutes that vary from about -2.5 to 0.5 m^2s^{-2}. The large negative figure was a sharp peak at about 1200 m altitude in one interval, while the positive value occurred in another interval. The wind was weaker in the earlier interval. They also broke the momentum flux down into "large-eddy" and "sub-grid" fluxes (greater than and less than 100 m, respectively), both of which showed similar patterns.

The same researchers, along with W. Eberhard, report measurements with a Doppler lidar (Gal-Chen et al., 1992). The measurements were taken over grassland during the First ISLSCP Field Experiment (FIFE) in Manhattan, Kansas during July 1987. Two periods of 40-60 minutes around midday were examined. The surface wind was approximately 15 m/s, increasing to about 19 m/s at 1 km above ground level (AGL). Momentum fluxes in the mixed layer were around 0.5 m^2s^{-2} and agreed with an aircraft measurement at 50 m AGL, while those immediately above the mixed layer were 1 to 3 m^2s^{-2}. The authors interpret these large values as evidence of a critical layer just above the mixed layer.

All the measurements summarized in this section are from short campaigns, most from a single day. This precludes drawing any firm conclusions about whether the results are representative of some average behavior of the boundary layer. The comparison of the measurements to theory or model results, which do represent an average, is then difficult.

FIFE also included a large number of aircraft and surface flux measurements (Kelly et al., 1992; Betts et al., 1992; Grossman 1992; Smith et al., 1992). The FIFE results will be discussed further in chapter 6.

3. The Profiler/RASS Instrument

In this chapter we describe the boundary layer wind profiler radio acoustic sounding system (profiler/RASS) that was used to make the heat and momentum flux measurements. We also discuss a number of improvements to previous RASS techniques, including simultaneous measurement of winds and virtual temperature and the use of an integrated acoustic source.

3.1 The boundary layer profiler

A wind profiler is a Doppler radar that operates by measuring the velocity of patterns of fluctuations in the refractive index of the atmosphere. The radar is sensitive to fluctuations with spatial scales of half the radar wavelength. The refractive index can be expressed as (Gage 1990):

$$n-1 = \frac{3.73\times10^{-1}e}{T^2} + \frac{77.6\times10^{-6}p}{T} \qquad (3.1)$$

where e here is the partial pressure of water vapor in millibars, p is the atmospheric pressure in millibars, and T is the temperature in Kelvin. Under most conditions in the boundary layer, the first term (water vapor) dominates.

The 915 MHz wind profiler, developed by the NOAA Aeronomy Laboratory for use in the lowest few kilometers of the atmosphere, is described in detail by Ecklund et al. (1988). Table 3.1 lists important parameters.

Table 3.1: Boundary layer profiler/RASS parameters.

Frequency	915 MHz
Peak power	500 W
Antenna	Microstrip array
Beam width	9 degrees
Acoustic frequency	2 KHz (nominal)
Acoustic power	30 W

A large number of these relatively compact and portable systems have been built and deployed by various groups. The major variable among the various deployments has been the size and

configuration of the antenna or antennas. Each antenna panel is a square 0.91 m on a side. The system used at ROSE II and in the Platteville experiments had an antenna made up of four panels in a square configuration and pointed by a mechanical platform.

The height resolution of the radar is determined by its pulse width. The NOAA boundary layer profiler resolution can be selected to be 60, 100, 200, or 400 meters. Generally, the sensitivity of the profiler limits the maximum height of wind profiles to 2-3 km in most continental conditions, although much higher coverage is achieved in the tropics. In calm or cold conditions, the radar reflectivity of the atmosphere is low because there is little turbulence or little variation in temperature or humidity to produce refractive index fluctuations. Around sunrise when the air is stable and calm, and in the continental winter, the height coverage can be limited to a few hundred meters. Good average wind profiles can often be derived from sparse data, even if up to half of the readings are bad, but flux measurements cannot be made reliably under these conditions. Furthermore, in rain or snow the 915 MHz radar detects the fall speed of the hydrometeors, not the wind speed. With appropriate processing, horizontal winds can be retrieved in precipitation, but fluxes cannot. Ground clutter and airborne targets such as birds, insects, and aircraft can also contaminate the vertical wind measurement. Chapter 4 discusses data quality control techniques to deal with these types of contamination.

3.2 RASS background

A radio acoustic sounding system (RASS) is an adaptation of a wind profiler (or other radar system) to measure temperature. The temperature profile is calculated from a radar measurement of the speed of sound as a function of altitude. In addition to the radar, a RASS consists of an acoustic source, one or more transducers, and data processing enhancements. Figure 3.1 shows the arrangement of the profiler antenna and the four acoustic sources (horns or dishes) used in this study. The profiler antenna was enclosed in a shield to reduce the effects of ground clutter. The acoustic drivers were parabolic dishes or offset feed horns and were placed about 2 meters from the center of the antenna. All four sources were continuously driven.

The acoustic subsystem produces an acoustic wave in the atmosphere above the radar, the wavelength of which is nominally half the radar wavelength. This wave pattern reflects the radar signal in the same manner as clear air refractive index fluctuations. However, the acoustic wave is propagating at the (local) speed of sound. The Doppler frequency of the radar return from the acoustic wave train is the acoustic frequency, and the strength of the return depends on how closely the Bragg condition (acoustic wavelength equal to half the radar wavelength) is achieved. The strongest return, therefore, is at the Doppler frequency corresponding to the speed of sound. The

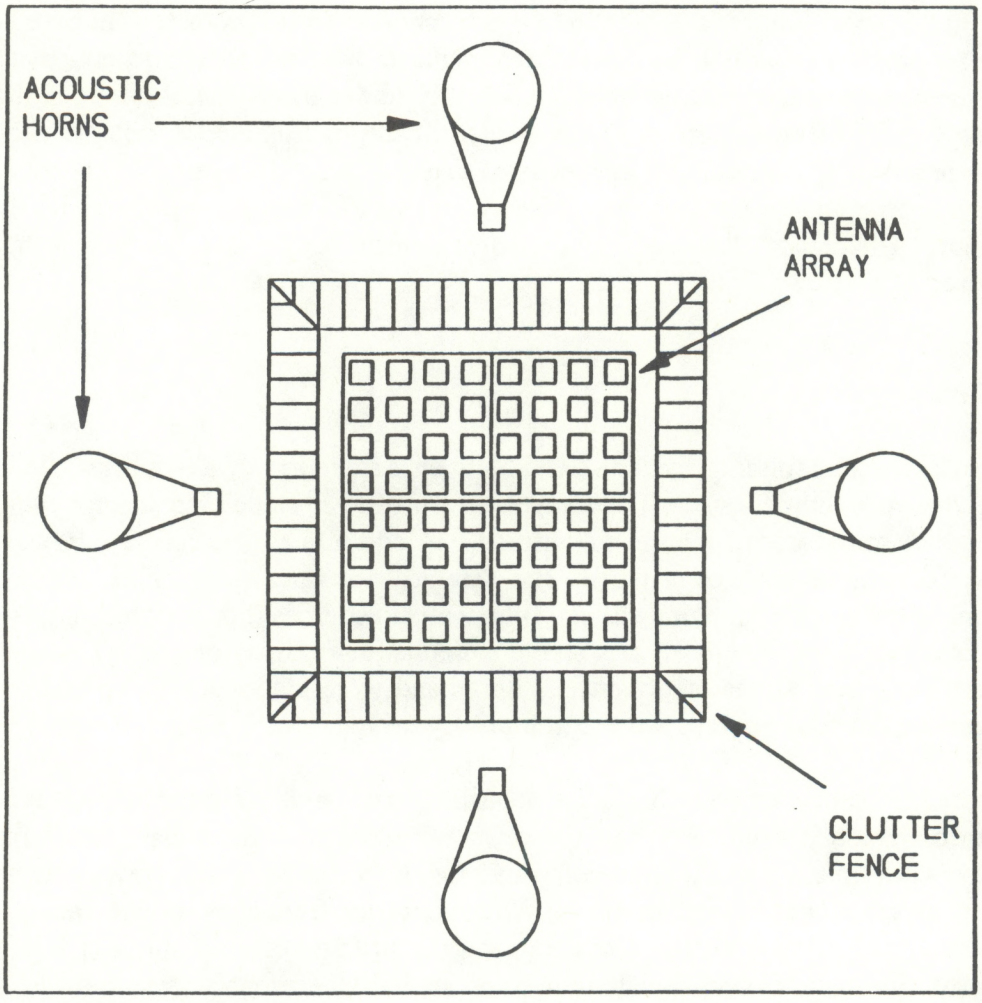

Figure 3.1: Schematic plan view of profiler/RASS system.

virtual temperature can then be calculated according to the relation for the sound speed of an ideal gas:

$$T_v = (C_a - v_r)^2 \cdot \frac{M_d}{\gamma_d R} \qquad (3.2)$$

where C_a is the acoustic velocity, v_r is the clear-air radial velocity, M_d is the molecular weight of dry air, and $\gamma_d = C_p/C_v$ is the ratio of specific heats for dry air. As we discussed in chapter 2, the virtual temperature is the temperature of dry air at the same density as the moist air, and is therefore the appropriate quantity to use when buoyancy is of interest.

The RASS idea dates back to at least the early 1970s (Marshall et al., 1972; North and Peterson, 1973), but practical application awaited the increased sensitivity of wind profiling radars.

3.3 Simultaneous correction for wind in RASS temperature measurements

Due to data processing limitations, a receiver frequency offset has been used in previous work to shift the response at the speed of sound to near zero frequency (May et al., 1990). Such systems then compute the speed of sound with a 64- or 128-point fast Fourier transform (FFT), and correct for the receiver offset. Recently, my colleagues at the Aeronomy Laboratory and I have developed a technique using a 2048-point Fast Fourier Transform for processing the profiler data to allow the radar to measure both C_a and v_r simultaneously (Angevine et al., 1994). As we will show, this significantly improves the accuracy of the measurement. The simultaneous measurement also provides the velocities needed for eddy correlation measurement of virtual temperature flux.

If RASS measurements are made with a vertically-pointing radar beam, it may be reasonable under some conditions to assume that the wind velocity averages to zero over a sufficiently long time (of the order of an hour). In the planetary boundary layer or in mountain wave conditions, however, the mean vertical velocity may not be zero. One may also want to make measurements on time scales less than an hour, or one may wish to make the temperature measurement on a beam that does not point vertically. In all these cases, a simultaneous measurement of the wind velocity and the acoustic velocity is required. Possible alternatives to simultaneous measurements include making alternating measurements of the acoustic and wind velocities or using wind measurements that bracket the time period during which the acoustic measurement is made. We have tested these methods and show below that simultaneous correction gives better measurements than any of the alternatives.

We will use wind and acoustic velocity data from a boundary-layer profiler deployed at the Boulder Atmospheric Observatory to show the need for the simultaneous correction. The site is near Erie, Colorado, on a rounded ridge in rolling cropland, 1580 meters above sea level and roughly 30 km east of the Rocky Mountains. The data cover thirty minutes around noon on September 7, 1990. The BAO tower was not in operation.

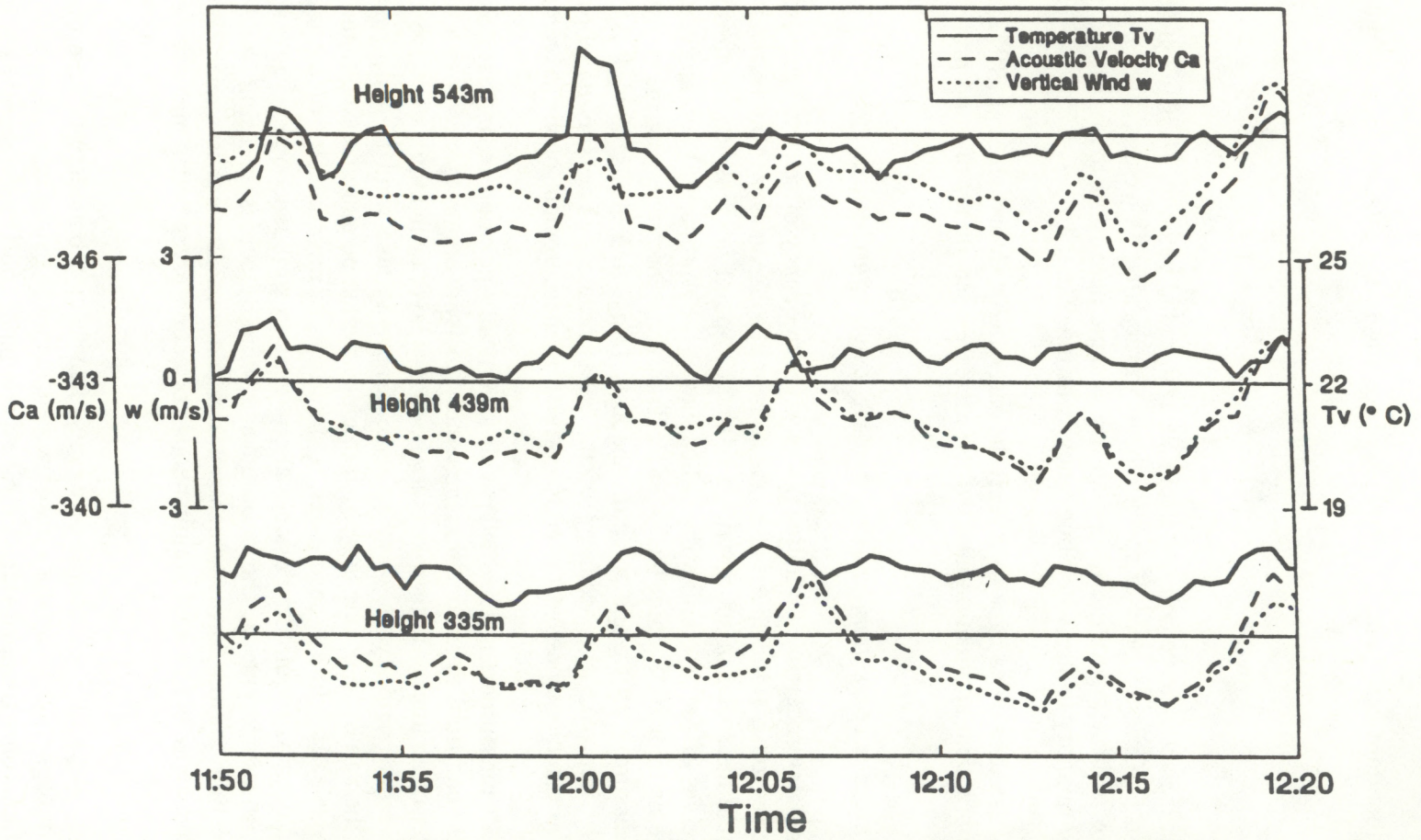

Figure 3.2: Virtual temperature, acoustic velocity, and vertical wind velocity at 3 heights during 7 September, 1990 at the Boulder Atmospheric Observatory. Times are MDT.

Figure 3.2 is a time series of observations at three heights. The data were taken at 26 second resolution. The time series were individually smoothed with a three-point moving average in order to improve the visual presentation. There are several interesting features in this plot. The air is sinking slowly most of the time, with occasional periods of rising air (for example, around 11:52, 12:01, and 12:07.) There is a classic thermal plume signature at 11:59 - 12:02, where the temperature rise and rising air appear slightly earlier at each higher range gate (Priestley 1959, p.70.) Note that the acoustic velocity and the vertical wind track closely, and temperature changes are associated with small changes in their difference. This illustrates the importance of simultaneous vertical wind measurement and correction. Without the correction, the apparent temperature fluctuations would be much larger. This is especially clear in the latter part of the plot, where there are large fluctuations in the vertical wind and the acoustic velocity that are not associated with actual temperature changes. If the vertical wind correction had been done, not on the basis of simultaneous measurements, but with measurements spaced in time even as much as thirty seconds, much of the detail of the thermal plumes would be lost. In fact, the results might be significantly in error if the vertical wind and acoustic velocity measurements were taken during different conditions, for example, during and after a thermal episode.

We can also show quantitatively the differences between the various methods of computing the temperature discussed above. Four different methods were examined using this data. The first method was to neglect the wind velocity entirely (assume $v_r = 0$ in equation 3.2). The second method divided the 30 minutes of data into 10-minute segments. The temperature was computed using the average wind velocity from the first and third segments to correct the acoustic velocity measured during the middle segment.

The third method used alternating measurements. Recall that the data consist of simultaneous measurements of wind and temperature at 30 s intervals. We conceptually assign each measurement a sequence number. Two temperatures were computed from this method, one using pairs made up of even-numbered acoustic (C_a) and odd-numbered wind (v_r) measurements, and the other using the odd-numbered acoustic and even-numbered wind measurements. Finally, the fourth method used simultaneous correction, that is, the value of the vertical wind velocity was subtracted from the value of the acoustic velocity to give a corrected value at each time point. The corrected values were then averaged. No quality control was applied to the data in any method.

Table 3.2 summarizes the results for the range gate at 335 m. T_{w0} is the result from the first method, neglecting the wind velocity. T_{brac} was computed by the second method, using the wind velocity from the first and last ten minutes of the data set to correct the acoustic velocity measured during the middle ten minutes. T_{eo} and T_{oe} are the results from the third method, using even-numbered wind and odd-numbered acoustic measurements (T_{eo}) or odd-numbered wind and even-numbered acoustic measurements (T_{oe}). T_{sc} is the simultaneous correction result. Table 3.2 also shows the differences between the temperatures computed by each method and T_{sc}, the simultaneous correction result. We compare the other methods to T_{sc} in the absence of an independent reference temperature, because we showed in the discussion above that T_{sc} was the most likely to be correct, arguing from first principles.

Table 3.2: Temperature results (°C) computed by four methods for height 335 m and their differences.

T_{w0}	22.28
T_{brac}	24.56
T_{eo}	23.84
T_{oe}	23.34
T_{sc}	23.59
T_{sc}-T_{w0}	1.30
T_{sc}-T_{brac}	1.06
T_{sc}-T_{eo}	-0.25
T_{sc}-T_{oe}	0.25
T_{eo}-T_{oe}	0.50

During the time covered by this data, the mean wind velocity was significantly downward (-0.76 m/s at 335 m.) Neglecting the wind velocity makes T_{w0} substantially lower than T_{sc}. Method two, using bracketing measurements, also differs substantially, because the wind velocity was more downward during the first and third segments than during the middle segment.

Method three, using alternating measurements, gives results that are much closer to the individual correction result. This is as we would expect, since only the smallest measurable scales are neglected in this method. However, it is interesting to note that computing the temperature using even-numbered or odd-numbered measurements of both the wind and acoustic velocity (not shown) gives much smaller differences (0.02 and -0.01 °C, respectively) from T_{sc}. This shows that it is the separation in time of the alternating measurements, not the reduction in sampling density, that causes T_{eo} and T_{oe} to differ from T_{sc}.

Simultaneous vertical wind and acoustic velocity measurements are clearly necessary if we wish to resolve thermal features in the convective boundary layer or make other measurements requiring time resolution of the order of minutes or less. The simultaneous correction is also needed if we wish to use an oblique beam (that is, a beam that does not point vertically) for RASS temperature measurements, which is desirable in some situations. In a system designed to profile winds in three dimensions as well as temperature, the radar usually cycles through two or four oblique beam directions between each measurement on the vertical beam. As a result, the vertical beam is sampled

infrequently. The available sampling rate using only the vertical beam may limit the time resolution that can be achieved, especially in convective or otherwise turbulent conditions. For flux measurements, good sampling density is even more vital.

The simultaneous correction technique has one drawback. It will only work when both the vertical wind and acoustic velocity measurements are available and uncontaminated. A possible way to avoid this problem is not to use the correction when rain is detected, but in many cases the radial velocity will not be zero in rain, leading to error in the measured temperature.

3.4 Acoustic source

The acoustic excitation must be carefully chosen for optimum RASS performance. If the acoustic bandwidth is too narrow, the signal returned will be biased toward the transmitted acoustic frequency rather than that corresponding to the speed of sound (May et al., 1990). On the other hand, if the bandwidth is too broad, there will be too little power at the Bragg frequency at any given height, the return signal will be weak, and height coverage will be reduced. Gaps in the acoustic spectrum as observed by the profiler may also cause random or systematic errors.

The pulsed Doppler radar does not sample uniformly in time. Between data acquisition intervals, there is a pause for computations. If a deterministic acoustic signal (such as a sweep) is accidentally synchronized with the radar sampling period, the acoustic energy satisfying the Bragg condition at some heights (temperatures) will be present only during the calculation time, and an artificial gap in the height coverage will result.

In order to have a flexible source, we use a second digital signal processor board similar to the one that processes the radar signals. This board is programmed to produce the acoustic signal through an on-board digital to analog converter and coder/decoder (CODEC) circuit. The signal is a series of single-frequency segments of a specified duration or "dwell time." At the end of each dwell time, a new frequency is selected. The frequency series can be either a series of steps of specified size, or a random choice. In either case, the user chooses a frequency range or window. The series of steps is usually done with a step size small enough to make the series approximate a linear sweep, and this is called the "sweep mode." In the current implementation, the step size can be selected in 1 Hz increments. The frequency is stepped across the window from the lowest to highest frequencies and then the sweep is repeated.

Pseudorandom frequencies are chosen in the "random hop" mode. The only constraint on the spacing of the frequencies is the resolution of a floating-point number in the signal processor. The choices are uniformly distributed across the selected frequency window. The random hop appears to give slightly better results when the radar sample time is relatively long, and the sweep works better for short sample times. These observations, described further below, come from experiments in the atmosphere itself and from direct measurements of the spectrum of the acoustic excitation by the radar.

A practical advantage of the integrated acoustic source is that it can be controlled by the same program that operates the radar, making it an integral part of the radar/RASS. We have programmed the computer to turn on the acoustic source for a selected period of time during each hour, for example, and to reconfigure the radar to operate in RASS mode during that time. This can be helpful at sites where continuous RASS operation might disturb nearby residents.

We conducted an experiment with a 915 MHz profiler at the BAO site on December 7, 1990 to compare the performance of the two acoustic excitation types. Frequency window widths of 30, 50, 100, and 150 Hz were used, and the dwell time was varied from 1 to 100 milliseconds. The number of spectra averaged by the radar was varied from 3 to 50. Due to the variability of the atmosphere, it is difficult to draw rigorous quantitative conclusions, however the qualititative results may be summarized as follows:

1) The signal-to-noise ratio of the acoustic return is stronger when the frequency window is narrower. This is as expected, since a larger window spreads acoustic energy over a larger range, most of which does not meet the Bragg condition.

2) Random hop gives stronger return signal than sweep for windows of 50 Hz or wider, but weaker for the 30 Hz window. The difference can be up to several dB. Again, this result is expected, since the random hop gives a more even distribution of energy over the wider windows during the sampling interval.

3) In the sweep mode, frequency step size as large as 5 Hz has no visible effect on the spectrum of the return signal. This is probably due to the bin size of the FFT (3 Hz) and spreading of the signal peak by atmospheric turbulence and wind.

4) When small numbers of spectra are averaged, as for example when high time resolution is required, the sweep mode works better, since it ensures that there is acoustic energy at all frequencies over a short time. With 10 spectra averaged, the sweep mode with very short dwell time (5 ms) and 1 Hz steps works well.

A second experiment used the radar as a spectrum analyzer to examine the spectrum of the transmitted acoustic signal. The output of the acoustic source was fed directly into the input of the radar analog-to-digital converters. The resulting output is the spectrum of the acoustic excitation as seen by the radar, including the effects of non-uniform sampling. The desired spectrum is flat over the range of frequencies corresponding to the temperature range of the atmosphere during our measurement, and contains no components outside that range.

Figure 3.3a shows a power spectrum determined by this method for a random hop excitation with a 100 Hz window and 25 ms dwell time. The radar averaged 25 spectra. Figure 3.3b shows the spectrum for the same 100 Hz window and 25 ms dwell time for sweep mode with a 1 Hz step size. The two spectra are similar, but the sweep mode spectrum has slightly sharper edges. The frequency window should therefore be set slightly larger for the random hop mode, negating some of the advantage that mode appeared to have in the real-atmosphere experiment described above.

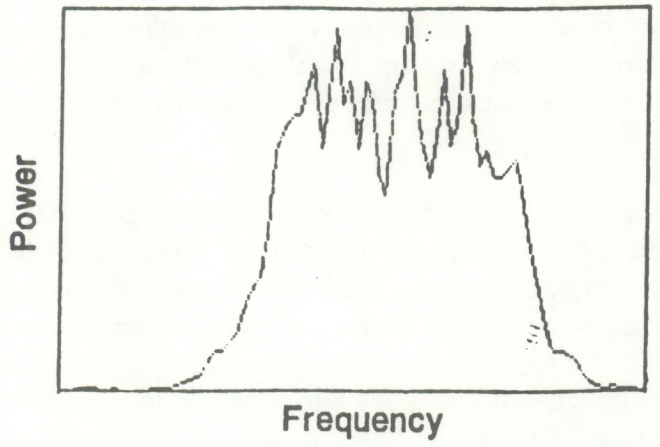

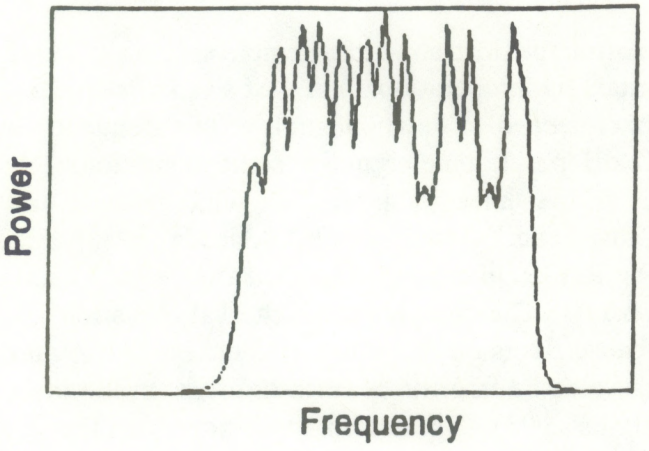

Figure 3.3: Spectra of the acoustic source as measured directly by the radar. Source parameters: Window 1950-2050 Hz, dwell time 25 ms, 25 spectra averaged. a) Random hop mode. b) Sweep mode with 1 Hz step.

It is important to note that the non-uniform spectra of figure 3.3 are fundamentally different in character. The random hop spectrum tends to uniformity for sufficiently long averaging times. The sweep mode, on the other hand, has a deterministic ripple, which does not average out. Any non-uniformity in the transmitted acoustic spectrum will be reflected in the radar return, and may bias the measurement. The effect is not clearly shown in the figure because the averaging times are relatively short.

Acoustic source parameters close to those used to produce figure 3.3 were used for the Platteville and ROSE II experiments reported in chapters 5 and 6. These parameters are a good compromise between high time resolution and good return power. A fairly wide frequency window (up to 150 Hz for the 915 MHz radar) was required for long-term operation over wide temperature ranges.

Some observers find the random hop mode less annoying to the ear than the sweep mode, which has been compared to a siren. Others find either mode equally annoying.

3.5 Summary

Systems incorporating simultaneous correction and the integrated acoustic source have been deployed by the Aeronomy Laboratory and Wave Propagation Laboratory (WPL) for field programs since January 1991. The programs include the Department of Energy Atmospheric Radiation Measurement Program (ARM), Winter Icing and Storms Project (WISP), the Front Range Air Quality Study, and the San Joaquin Valley Experiment. The profiler control system is also in use on the WPL 50 MHz research profiler at Platteville, Colorado.

While the RASS is an attractive instrument for remote sensing of temperature in the atmosphere, it is subject to serious limitations in operational use. At a radar frequency of 915 MHz, an acoustic frequency of about 2 KHz is needed. The attenuation of this frequency by the atmosphere is quite severe, ranging up to 40 dB per kilometer under some conditions (Harris, 1966). The height coverage of the RASS is further strongly limited in wind because the acoustic wavefronts are advected away from the radar beam. Lataitis (1993), Masuda (1988) and May et al. (1988) discuss these factors in detail. The RASS, like the clear air measurement, is subject to poor reflectivity in very dry air (equation 3.1). The temperature retrieval equation (3.2) makes use of some approximations that may cause errors on the order of 1° or less (Angevine and Ecklund, 1993). The calculated temperature may also be in error because of errors in the measurement of C_a caused by winds and turbulence (Lataitis 1993). These errors will not affect the flux measurements, but they should be accounted for if accuracies greater than 1° in the mean temperature are needed.

4. Data Analysis Procedures

In this chapter we describe how the profiler/RASS data are analyzed to produce flux estimates. We present the data quality control algorithms derived for this study and the methods we used to calculate heat and momentum fluxes from the profiler and aircraft data.

4.1 Profiler data analysis

4.1.1 Data quality control

Raw profiler/RASS data contain both correct and incorrect estimates of the wind and acoustic velocities. Incorrect velocity estimates may be due to ground clutter, birds, insects, aircraft, poor return signal power, rain, or radio-frequency interference. Before they can be used to calculate flux, the velocity time series must be cleaned to remove the incorrect data points. Traditional profiler data cleaning algorithms rely on continuity in height and/or time to distinguish bad data from good. In other words, in traditional methods, only velocity estimates that are reasonably similar to estimates above, below, before, and after the particular height and time in question are considered to be good. In the turbulent convective boundary layer, this assumption is too restrictive. The size of the radar resolution cell is within the range of scales of active turbulence, and so individual measurements are expected to differ substantially even in adjacent heights and times.

A "good" cleaning algorithm for the purposes of this study is one that is automatic, physically justifiable, produces reasonable flux results, and removes as few data as possible. An automatic algorithm removes any dependence on the training or vigilance of an operator, and may be economically and reliably used on large data sets. Reasonable flux results, as defined by previous observations, are less than about 0.2 Kms^{-1}, and are smooth and linear over the height range of the convective boundary layer. These criteria were used to choose the approach and parameters discussed here.

The approach used on the data presented here is to clean the data with a set of statistical filters. The filters are applied to each of the moments available from the profiler, that is, to the signal-to-noise ratio (SNR), the velocity, and the spectral width of the clear-air and acoustic velocity spectra. From hour to hour and day to day, the distributions of the six moments change as the strength, height, and scale sizes of the turbulence change. For example, early in the morning the variance of the velocity is likely to be much smaller than at midday. Also, the mean acoustic SNR will vary depending on the wind speed. Statistical filtering is automatically adaptive, that is, as the distributions of the moments change over time, the filters change width accordingly. This would not be the case if, for example, fixed windows were chosen to define good data.

Having chosen the statistical filtering approach, it remains to choose the parameters for each of the six moments. The parameters are the center (mean or median) and the width (in number of standard deviations) of the acceptable window for each moment. The acoustic SNR is a special case,

in that a single threshold is used, as discussed below. For simplicity, the moments from all five beams are treated identically. Figure 4.1 shows the distributions (that is, the number of occurrences of a given value) of the six moments for the two-hour period around noon on 13 days of ROSE II (16-28 June 1992). Some possible choices for filter limits are also shown. In the figures, the distributions are plotted with the baseline (zero occurrences) for each height at that height on the ordinate. The vertical distance between each succeeding height corresponds to approximately 800 occurrences of that value. The logarithm of the distribution is plotted.

In the clear-air velocity distribution (figure 4.1a), the mean and median are quite close. We chose to use the median because it is less influenced by outliers. If we chose limits of $\pm 2\sigma$, we would cut off points that are legitimately part of the main velocity distribution. A $\pm 3\sigma$ cutoff occasionally includes some points that are questionable, but this is preferable since the filter for each individual moment need not remove all outliers. The acoustic velocity distribution (figure 4.1b) shows fewer outliers, as we would expect because most of the sources of contamination discussed earlier in this section are not present near the speed of sound. Again, the $\pm 3\sigma$ limit was chosen to include all of the distribution.

The clear-air SNR distribution (figure 4.1c) has noticeable dips near $\pm 2\sigma$ at several heights, which may indicate the edges of the distribution of legitimate data. An unusually high clear-air SNR is probably due to a hard target (bird, insect, or aircraft), while an unusually low clear-air SNR is due to weak reflectivity or increased noise, and is unlikely to yield a good velocity estimate. A fixed threshold rather than a statistical filter is used for the acoustic SNR (figure 4.1d) since there is no source of high-SNR spurious data. The threshold of -25 dB was the smallest possible SNR that gave reasonable flux results.

The distributions of clear-air and acoustic spectral width (figures 4.1e and f) are similar. Both have long tails toward large width. Generally, very large spectral widths indicate contamination or weak signal, and small spectral widths indicate a point target such as a bird or aircraft. The $\pm 3\sigma$ limit is below zero in most cases, so the filter would not remove any narrow cases if this were chosen. Therefore, the mean $\pm 2\sigma$ was originally chosen as the filter limit for both clear-air and acoustic spectral widths. Testing with the flux calculations (see below) showed that using the median $\pm 3\sigma$ on the acoustic spectral width eliminated fewer points without affecting the flux results significantly.

Figure 4.2 shows calculated values of virtual temperature flux from the same period discussed for the distributions of figure 4.1, that is, the two hours around noon averaged over 13 days. The effects of several combinations of filters are shown. The flux computed without cleaning is unreasonably large (>0.2 Kms^{-1}) in the 250-350 m AGL range. The full cleaning (all six filters) gives a reasonably smooth profile. Using only the filters on velocity (figure 4.2a) improves the profile substantially over the unfiltered result. Only an average of approximately 3 points (out of 180) are removed from each two-hour time series by the velocity filters. This is by far the most important and efficient filtering.

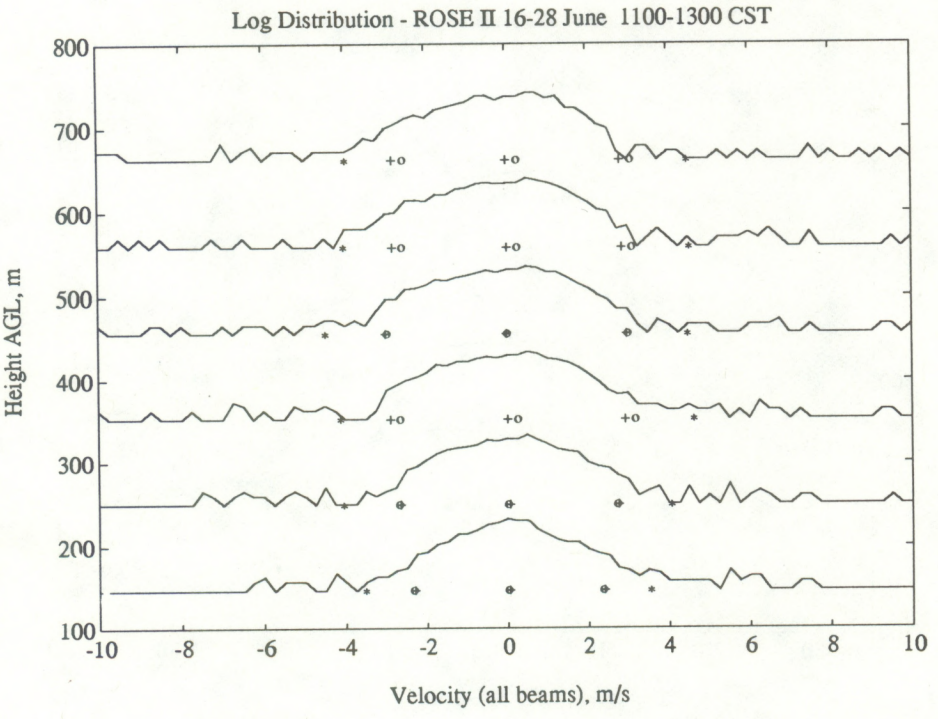

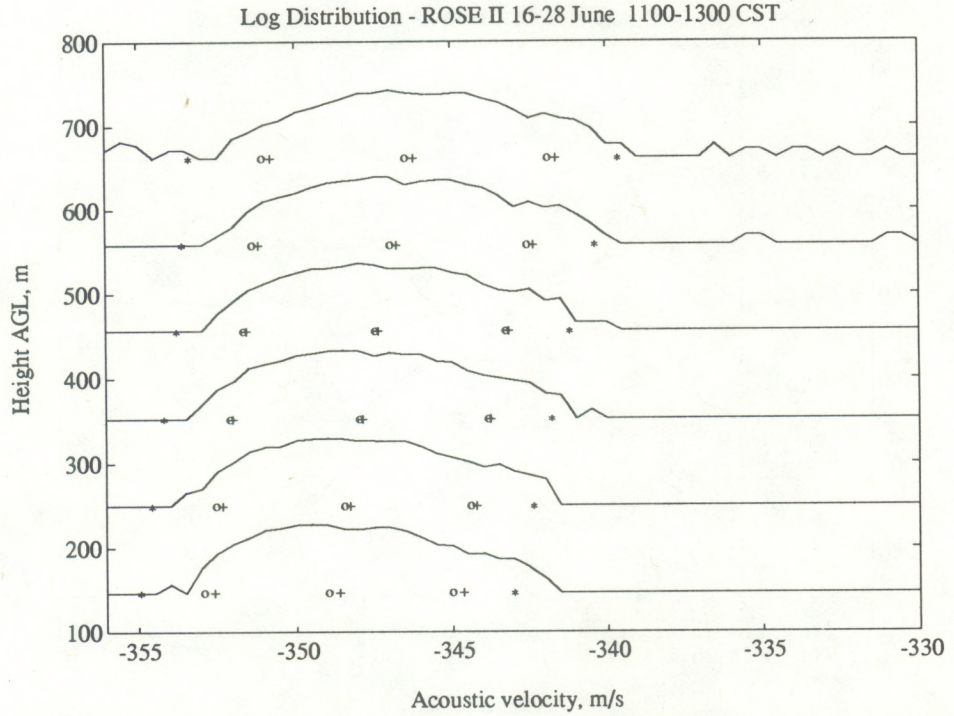

Figure 4.1a,b: Distributions of profiler/RASS moments: Clear-air and acoustic velocity. Filter parameters are also shown: + = mean and mean ± 2σ; o = median and median ± 2σ; * = median ± 3σ.

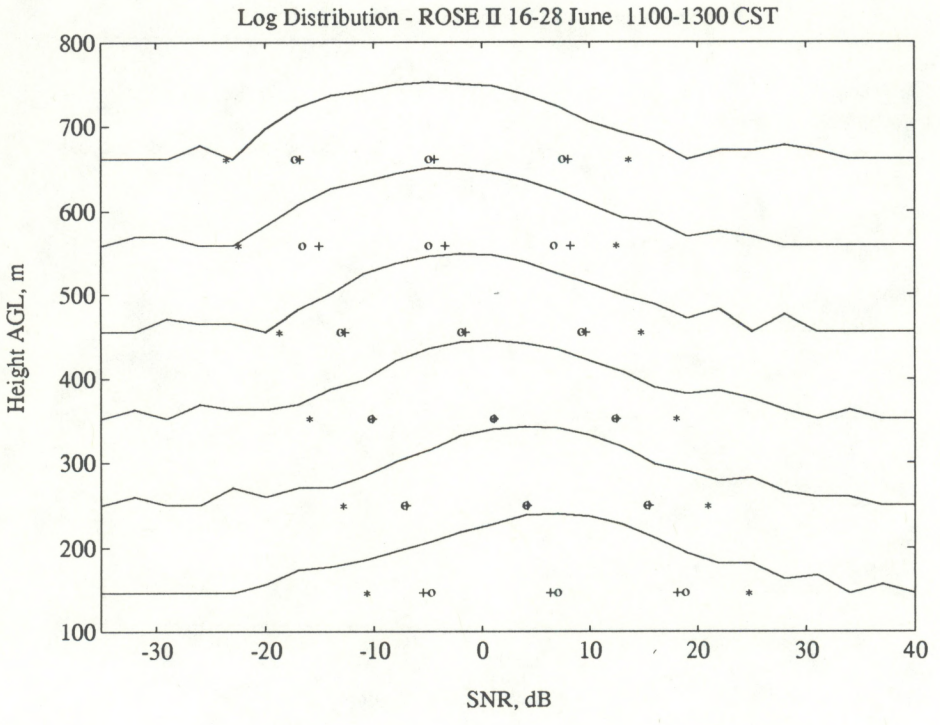

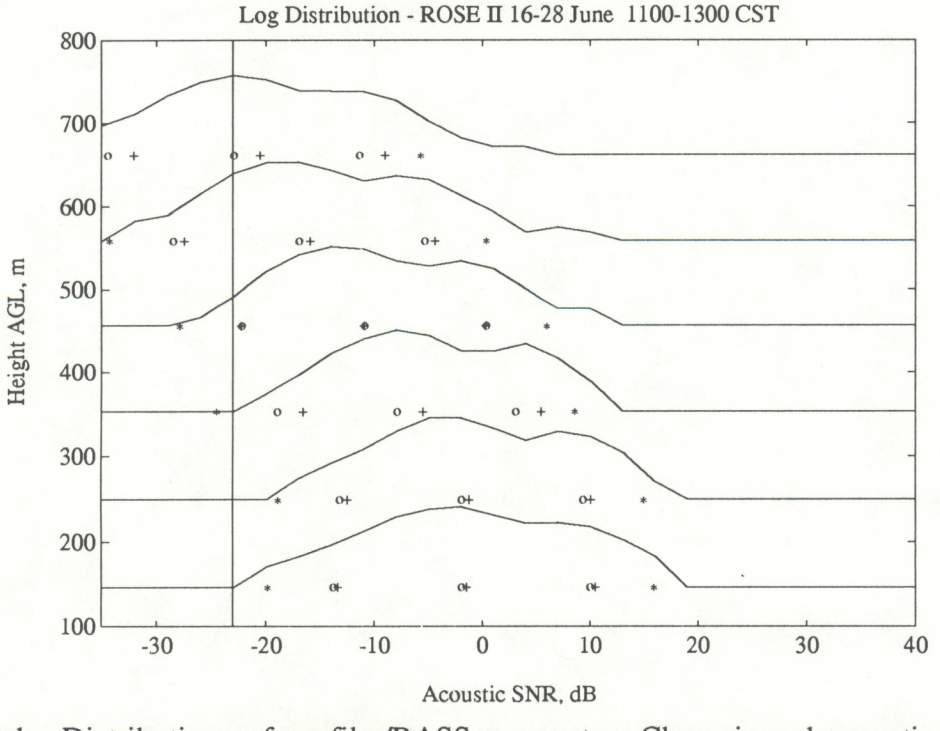

Figure 4.1c,d: Distributions of profiler/RASS moments: Clear-air and acoustic SNR. Filter parameters are also shown: + = mean and mean ± 2σ; o = median and median ± 2σ; * = median ± 3σ.

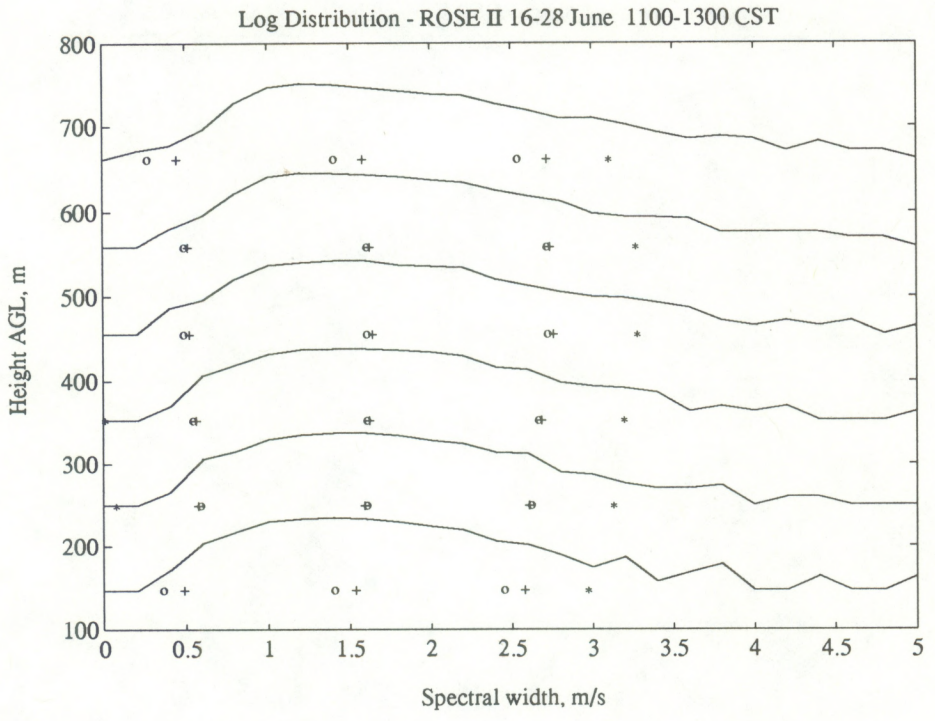

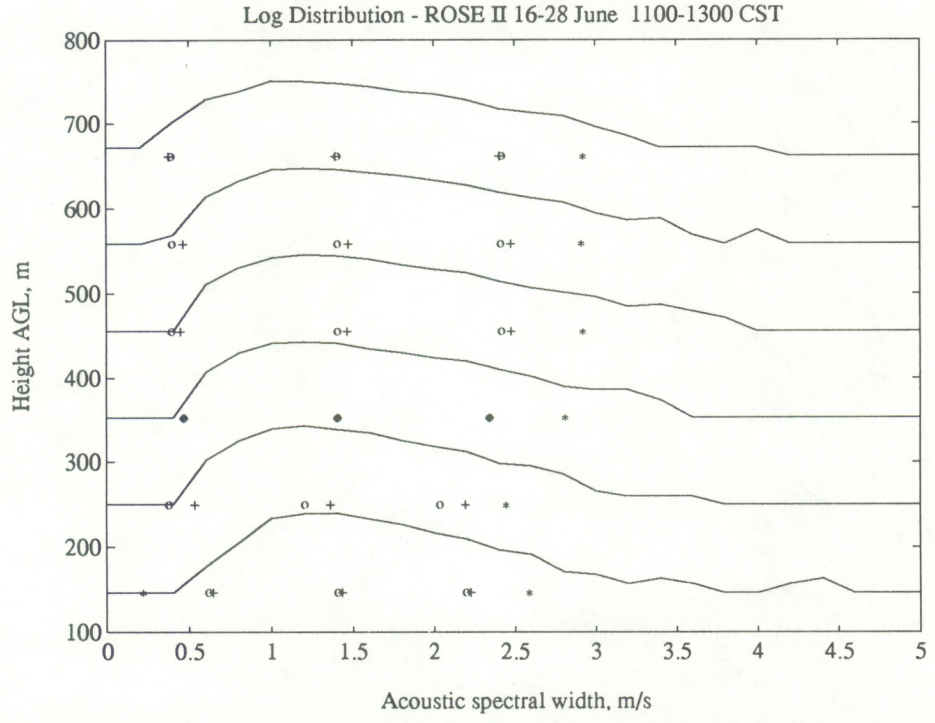

Figure 4.1e,f: Distributions of profiler/RASS moments: Clear-air and acoustic spectral width. Filter parameters are also shown: + = mean and mean ± 2σ; o = median and median ± 2σ; * = median ± 3σ.

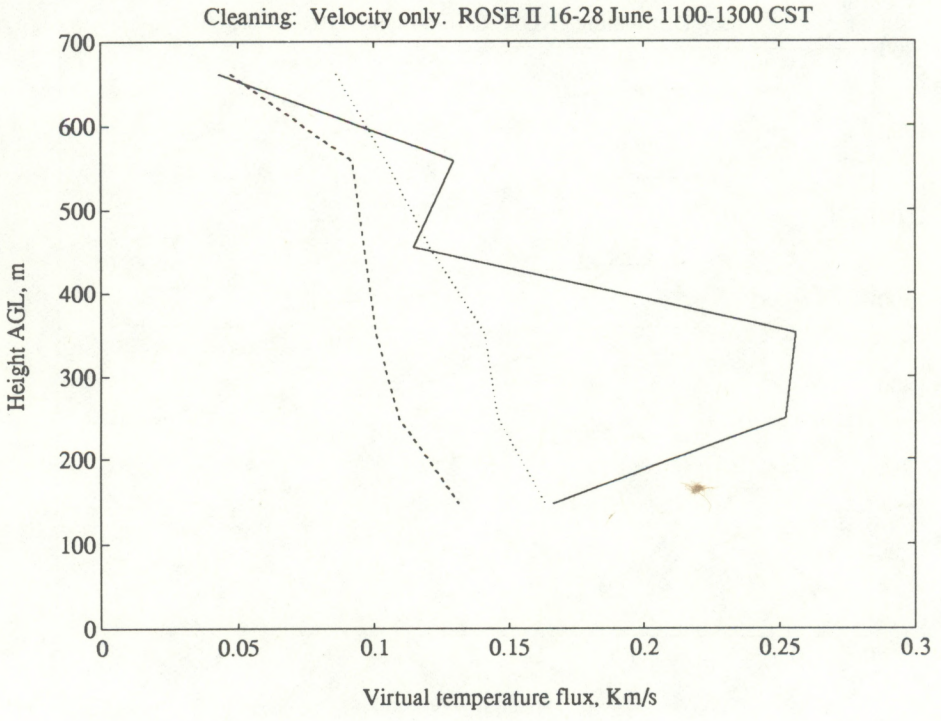

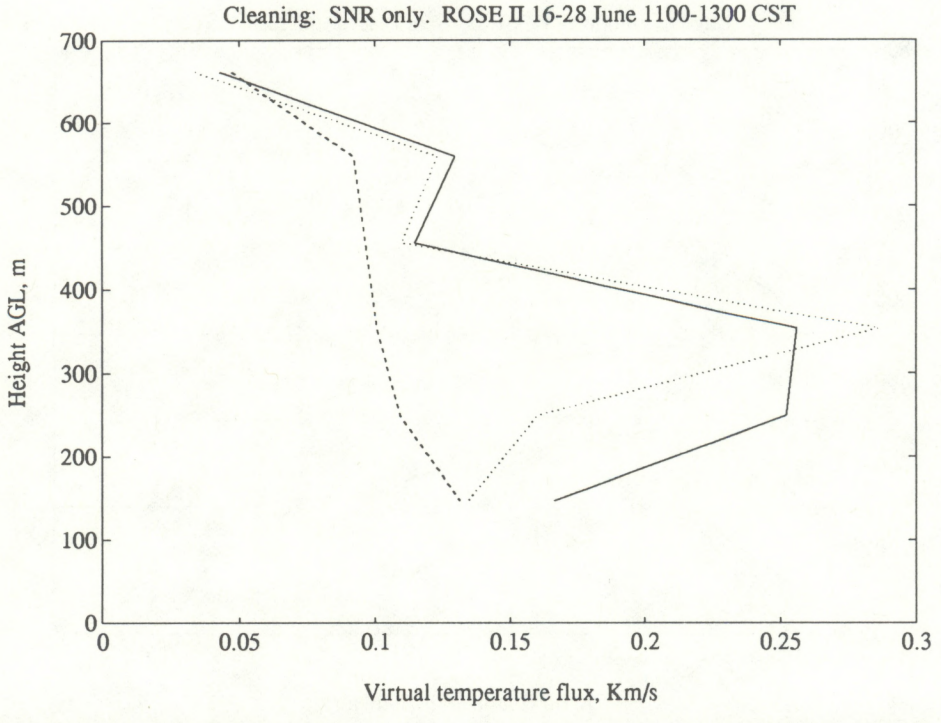

Figure 4.2a,b: Comparison of the effects of various cleaning methods (filter combinations) on the virtual heat flux. Solid: no cleaning. Dashed: full cleaning (see text). Dotted: Cleaning as described in title of each panel.

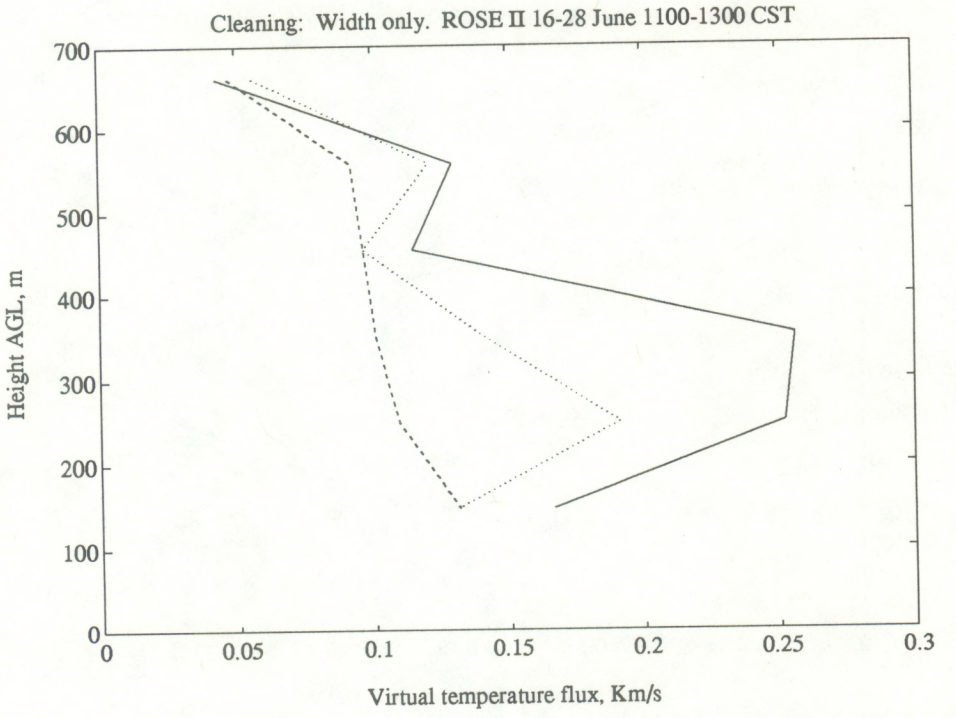

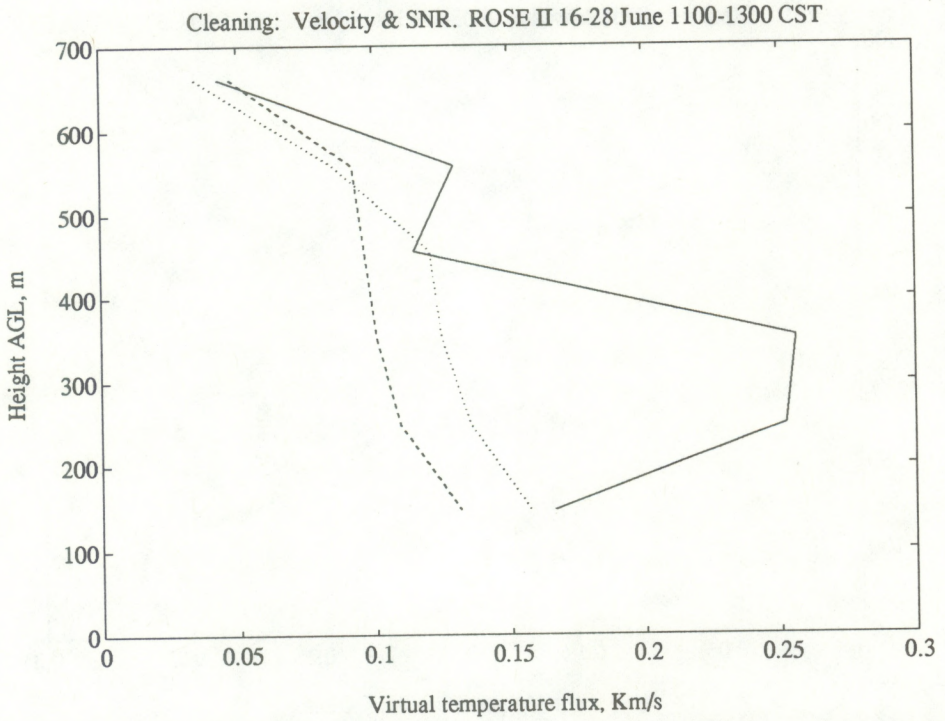

Figure 4.2c,d: Comparison of the effects of various cleaning methods (filter combinations) on the virtual heat flux. Solid: no cleaning. Dashed: full cleaning (see text). Dotted: Cleaning as described in title of each panel.

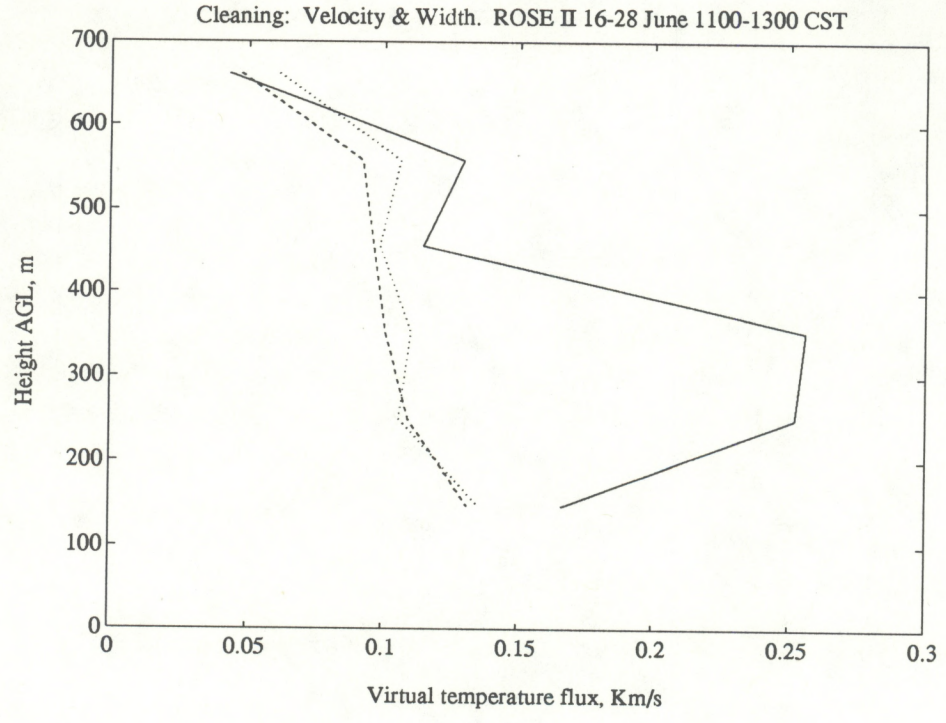

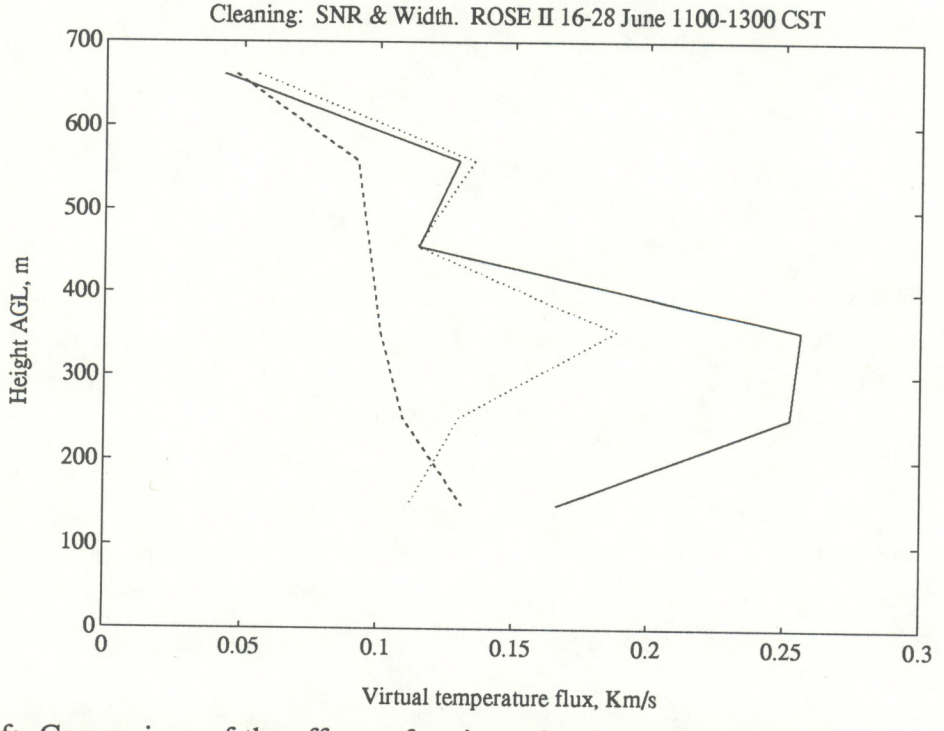

Figure 4.2e,f: Comparison of the effects of various cleaning methods (filter combinations) on the virtual heat flux. Solid: no cleaning. Dashed: full cleaning (see text). Dotted: Cleaning as described in title of each panel.

Filtering only on the signal-to-noise ratios (figure 4.2b) does not improve the profile, and removes approximately 10 points per two hours in the lower heights. The number of points removed rises rapidly above the fifth height as the acoustic SNR threshold takes effect. Filtering only on the spectral widths (figure 4.2c) does improve the profile, but not as much as the velocity-only filtering. Width-only filtering removes 12-13 points per two hours. Using the filters in pairs, velocity and SNR filtering (figure 4.2d) does not improve the profile much over filtering on velocity only, and removes approximately 10 points per two hours in the lower heights. SNR and width filtering (figure 4.2f) does not result in a very smooth profile. Velocity and width filtering (figure 4.2e) gives nearly the same result as the full cleaning (all six filters). The total suite of filters removes an average of 16-17 points in the lower heights, increasing rapidly above 550 m AGL. The number of points removed by each filter combination is not the sum of those removed by the individual filters, since the same point may be removed by more than one filter.

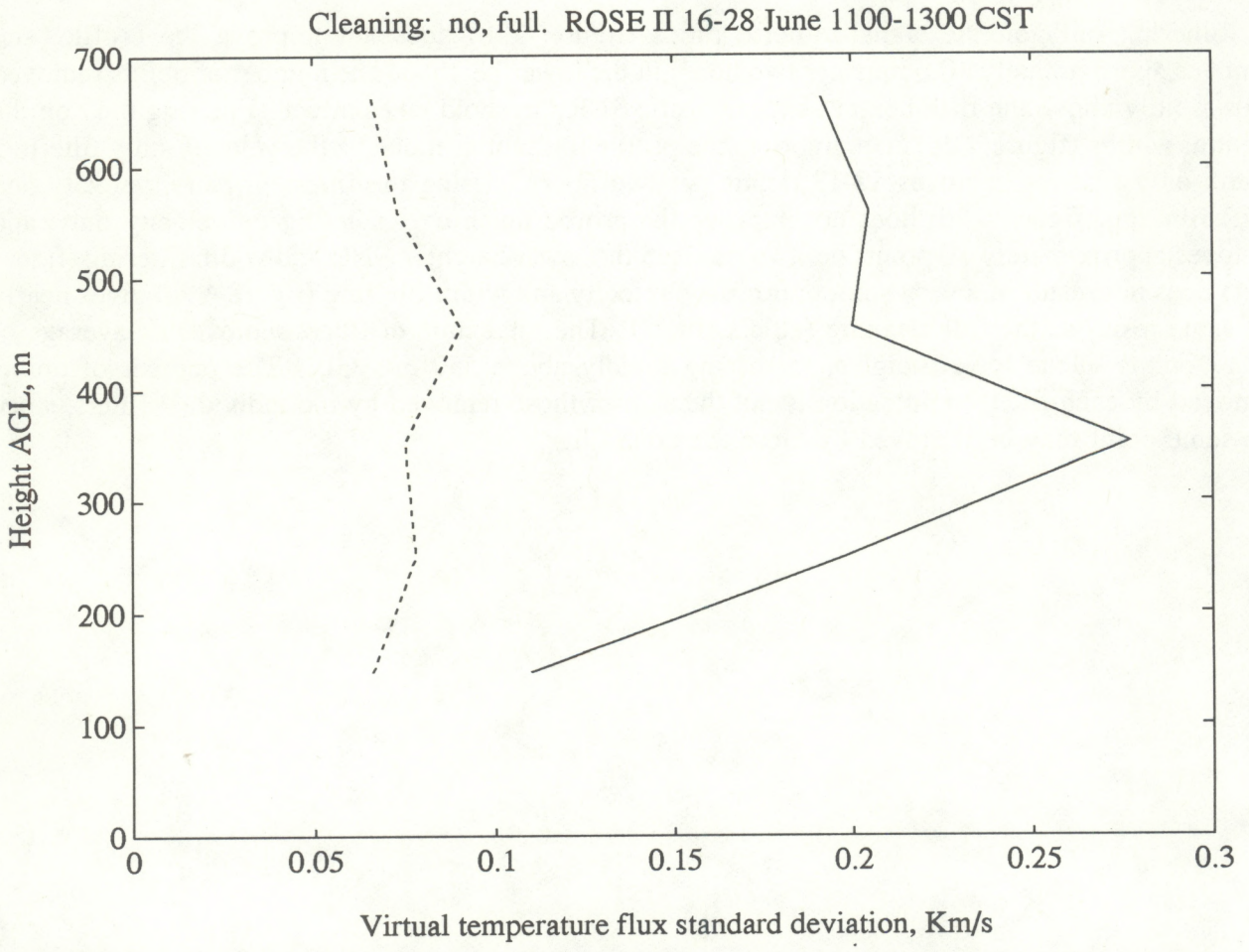

Figure 4.3: Standard deviation of virtual heat flux over 13 days without cleaning (solid) and with full cleaning (dashed).

One would prefer to be able to use flux measurements from individual periods, not just averages over many days. The averages examined so far could be hiding great day-to-day variations, and in fact this is the case for some of the combinations. Figure 4.3 shows the standard deviation of the virtual temperature flux over the 13-day average. With no cleaning, the standard deviation is quite large. The full cleaning suite reduces the variation substantially. These data are unscaled, so some of the variation is due to differences in the actual flux from day to day. The number of two-hour periods (days) with absolute values of virtual temperature flux more than some large threshold in the first six heights (range gates) is an indication of the ability of the cleaning algorithm to reduce variation due to errors. We chose 0.4 Kms^{-1} as the threshold for this comparison. With no cleaning, 13 of the 78 flux measurements are outside the acceptable range. Velocity-only filtering reduces the number of bad flux values to 3. Ten are bad with SNR-only filtering, 9 with width only, and 6 with SNR and width filtering. Velocity and SNR filtering reduces the number of bad values to 1, while velocity and width filtering leaves no bad values. The full cleaning suite also leaves no bad values.

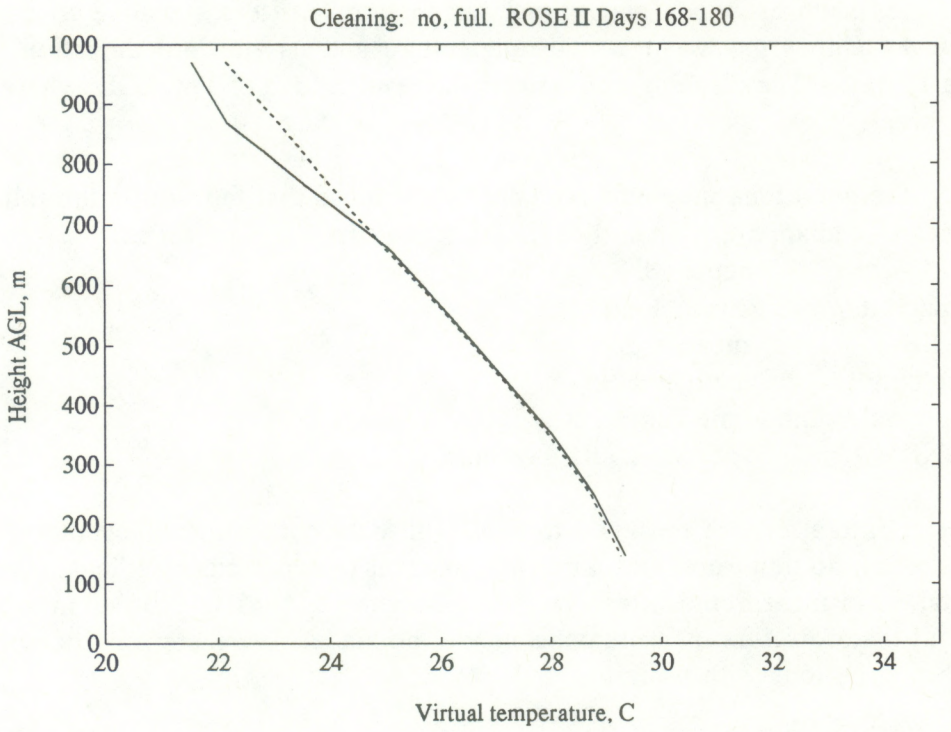

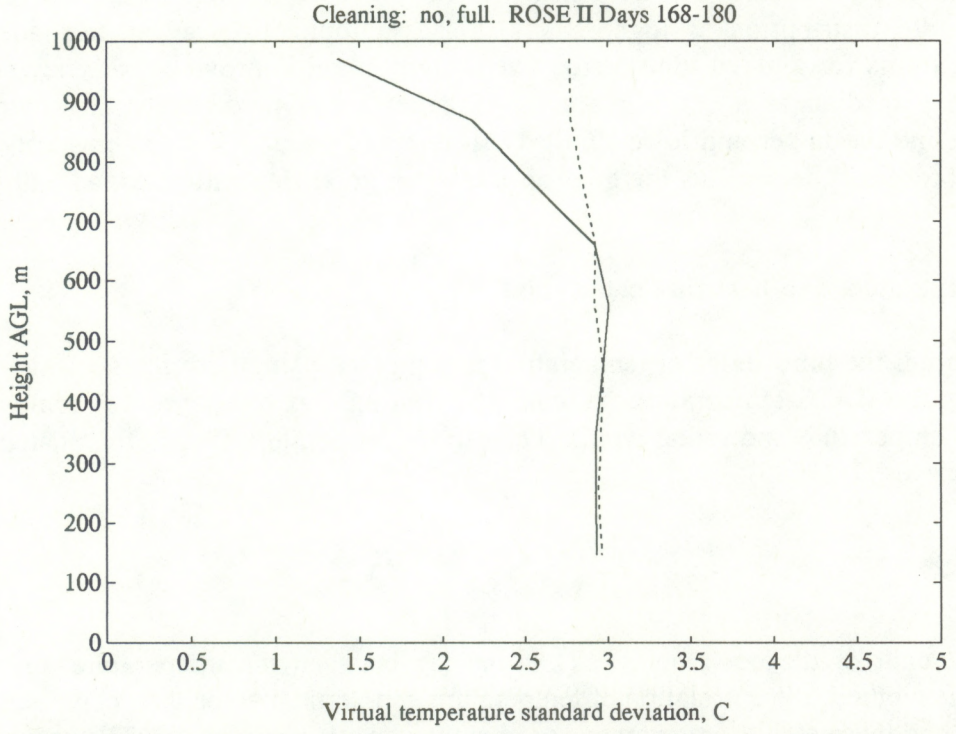

Figure 4.4: Mean and standard deviation of virtual temperature for 1100-1300 CST averaged over 13 days. Solid line is result with no cleaning, dashed line with full cleaning (see text).

Mean quantities such as winds and virtual temperature are less sensitive to bad data. For example, figure 4.4 shows the mean virtual temperature and its standard deviation for the noon period over the 13 days. The cleaning only affects the result above 650 m AGL, where the acoustic return signal is weak.

In summary, the good measurements are taken to be those that fall within the following limits based on the mean, median, and standard deviation (σ) of the 2 h time series:

Clear-air velocity:	median ± 3σ
Clear-air spectral width:	mean ± 2σ
Clear-air SNR:	mean ± 2σ
Acoustic velocity:	median ± 3σ
Acoustic spectral width:	median ± 3σ
Acoustic SNR:	above -25dB threshold

The statistical filters are not designed to deal with data contaminated by rain. The profiler responds very strongly to raindrops, and rain tends to occur over periods of at least several minutes. While horizontal wind measurements can be made with the 915 MHz profiler in stratiform rain, vertical wind and therefore flux measurements cannot be made. We therefore attempt to calculate the flux only during periods with no rain.

The purpose of the cleaning algorithm presented here is to produce flux estimates. Further refinement of these algorithms is certainly possible. For example, it might be reasonable to consider the spectral width distribution as lognormal and use multiplicative rather than additive limits. Smoothing the limits for a given time period over height might improve consistency slightly. The filters that use a median as a center point might better use a percentile rather than a standard deviation to define the upper and lower limits. All of these possible refinements notwithstanding, the algorithm presented here meets the goal of producing good flux estimates, as will be shown in chapter 6.

4.1.2 Temperature and heat flux calculation

After cleaning, the time series of temperature is computed using both the acoustic and clear-air velocities using the RASS temperature retrieval equation 3.2. A linear trend is removed from the time series of temperature and radial wind. The virtual temperature flux is then calculated by the method of Peters et al. (1985):

$$Q_v = \frac{1}{2}\left[cov(T_v', w')\,(-1) + cov(T_v', w')\,(1)\right] \qquad (4.1)$$

where the argument of the covariance (±1) is the lag between the temperature and the vertical velocity. In this method, the correlation of temperature and vertical velocity is computed at plus and minus one lag, and these results are averaged to give the correlation estimate. The covariance at zero lag is not used because it is contaminated by any errors that remain in the radial wind measurement, which enters into the temperature measurement as well (equation 3.2). The minimum fully

resolvable scale in the along-wind direction is therefore twice the profiler resolution cell size in that direction.

The 2 h averaging time was chosen as the longest possible time over which the atmosphere might be considered reasonably stationary. Flux estimates were made for each hour by overlapping the 2 h intervals.

4.1.3 Momentum flux calculation

The turbulent vertical flux of horizontal momentum on scales larger than the radar resolution cell is computed by the method of Vincent and Reid (1983):

$$\overline{u'w'}_{>res} = \frac{\overline{u_{r1}^2} - \overline{u_{r2}^2}}{2\sin 2\theta} \qquad (4.2)$$

where u_r are the radial-velocity fluctuations in two coplanar beam directions and θ is the zenith angle of the beams. This method uses the difference of the velocity variance measured by two beams aimed at the same zenith angle and opposite azimuth angles. A similar technique (Reid, 1987) is used to compute the sub-resolution momentum flux (the flux on scales less than the radar resolution cell) by subtracting the mean spectral widths of the two coplanar beams:

$$\overline{u'w'}_{<res} = \frac{\sigma_1^2 - \sigma_2^2}{2\sin 2\theta} \qquad (4.3)$$

where $\sigma_{1,2}$ are the Doppler spectral widths measured by beams in two coplanar directions. Both methods require the assumption that the statistics of the wind in the volumes illuminated by the two beams are the same. The spectral widths are contributed to by various aspects of the radar system as well as the turbulence, but all these contributions are assumed to be the same in both beams and therefore are removed by the subtraction in the Reid method.

The sampling uncertainty (equation 2.14) can be applied to the momentum flux calculation by computing the sampling uncertainty of the variances and propagating the uncertainties, giving

$$e_m = \frac{e_{r^2}}{\sqrt{2}\sin 2\theta} \qquad (4.4)$$

where e_m is the relative uncertainty of the derived momentum flux and e_{r2} is the relative uncertainty of the radial velocity variance. This result shows that the uncertainty is magnified by the beam geometry factor $\sin 2\theta$.

4.2 Aircraft data analysis

The NCAR King Air flew 8 flight legs during the 18-25 June 1992 intensive period of ROSE II that met all the criteria for use in this study. The criteria were that the flight path was over the forest and site, the flight altitude was within the boundary layer, all necessary instruments were operating, and the leg length was at least 10 minutes (48 km along the flight track).

Data from each of the flight legs were checked at NCAR for gross sensor failure. Each leg was then carefully trimmed to include only straight and level flight. The data were then extracted from the NCAR format at 20 Hz rate. The Lyman-α hygrometer data were scaled to the chilled-mirror dewpoint instrument for each flight leg in order to eliminate flight-to-flight drift of the Lyman-α instrument (Friehe et al., 1986). For comparison with the profiler, the kinetic temperature, humidity, and vertical wind data were block averaged to 1 s (approximately 80 m along the flight track.) A linear trend was removed from the time series and the virtual temperature flux and momentum flux were then computed directly.

5. Feasibility Study - the Platteville Experiment

In this chapter we describe the first heat and momentum flux measurements made to establish the feasibility of the profiler/RASS flux technique. We describe the experiment site and setup, and show the winds, temperature, heat flux, and momentum flux results. Finally, we discuss briefly the uncertainties of these measurements. The results of this experiment have been published (Angevine et al., 1993a).

5.1 Experiment description

During the summer and fall of 1991, the NOAA Aeronomy Laboratory operated a boundary layer wind profiler radio acoustic sounding system (profiler/RASS) at Platteville, Colorado. The purpose of the experiment was to determine whether this instrument could be used to measure profiles of heat and momentum fluxes as well as the more usual wind and temperature profiles. The Platteville site is located atop a shallow ridge at 1523 m above sea level. Vegetation is limited to low grasses with widely spaced stands of trees.

The boundary layer wind profiler was described in chapter 3. In the Platteville experiment discussed here, the acoustic velocity and wind velocity were measured on all four or five beams in order to sample the temperature as often as possible. The radar was operated at 60 m vertical resolution, and the height range covered was from 160 to 914 m. The sampling time for each measurement was about 30 seconds, and the total time for each measurement was about 40 seconds, including time for calculations and for the mechanically steered antenna to move and stabilize. The acoustic excitation was by random hop, where the acoustic frequency is chosen randomly from within a selected window. A new frequency was selected every 25 ms. The frequency window was 2020-2180 Hz, corresponding to a temperature range of 0 to 45 degrees Celsius.

The operating mode used in this experiment is not optimal for any individual measurement with this system. For example, the average height coverage of the RASS could be increased by 300 to 400 m by using only the vertical radar beam direction, since the acoustic sources were directed vertically and their half-power beamwidth is only about 10 degrees. On the other hand, the wind measurements could have been made to much higher heights if the system was not also running as a RASS, since computer memory limitations restricted the number of range gates that could be used in the RASS mode. Since the time of the Platteville experiment, the digital signal processing program has been changed to allow more heights. The operating mode was chosen to explore the use of the system for a large set of measurements.

5.2 Results

Time series of winds and virtual temperature were calculated over 2 h bins, producing 2 h average winds, temperatures, and fluxes for each day, and then composites were formed of these bins

over a 9 day period. The composites are used to simplify the presentation and to reduce the sampling uncertainty by increasing the effective averaging time. These results are from 13-24 June 1991 (day of year 166-177), a period that includes the summer solstice. Nine days in the period (days 166, 168-171, and 174-177) had no rain, and therefore were chosen for the analysis.

In all figures, each time point represents a 2 h average over the nine days. The 2 h average period is centered about the indicated local standard time. The 9 day average is used to reduce the scatter in the data, which would otherwise be very large. The reader will recall the discussion of sampling uncertainty in chapter 2.

5.2.1 Winds

Figure 5.1 shows the average horizontal wind speed and direction profiles. In this period, the average winds were fairly light and steady, and primarily toward the west or northwest at the surface, toward the north at the upper heights. There are no strong shears in the wind speed. The direction veers with height during most times.

Figure 5.2 shows the vertical wind velocity and standard deviation time series. The vertical velocity is generally slightly downward. Downward velocities are often measured with UHF profilers, and the cause is still under discussion. A possible explanation is that particles with a small fall velocity influence the measurement. The large deviations measured during the hours around sunrise (0400-0800) in the upper heights are an anomaly due to poor radar reflectivity at those times, when the atmosphere is very stable and quiet. Otherwise, the standard deviation is larger during midday than in other periods due to turbulence.

5.2.2 Virtual temperature

The virtual temperature was computed according to equation 3.2 using simultaneously measured vertical velocities. Velocity measurements from each coplanar beam pair were combined to produce a vertical acoustic velocity and a vertical wind velocity. This results in an equivalent sample spacing of 60 seconds in the five-beam mode. Outliers more than three standard deviations from the median over each two-hour time bin were removed from the temperature time series. Figure 5.3 shows time series of the virtual temperature at each height as measured by the RASS. The temperature shows a diurnal variation, which decreases with height.

5.2.3 Heat flux

The virtual temperature flux (equation 2.5) is computed by the technique of Peters et al. (1985) as discussed in chapter 4, equation 4.1. The virtual temperature and the wind velocity used in this calculation were calculated from all individual oblique beams. This measurement represents the flux on time scales longer than twice the radar sample time (80 s) and shorter than the two-hour time bin. The total flux is larger than that measured because of contributions on smaller time scales not

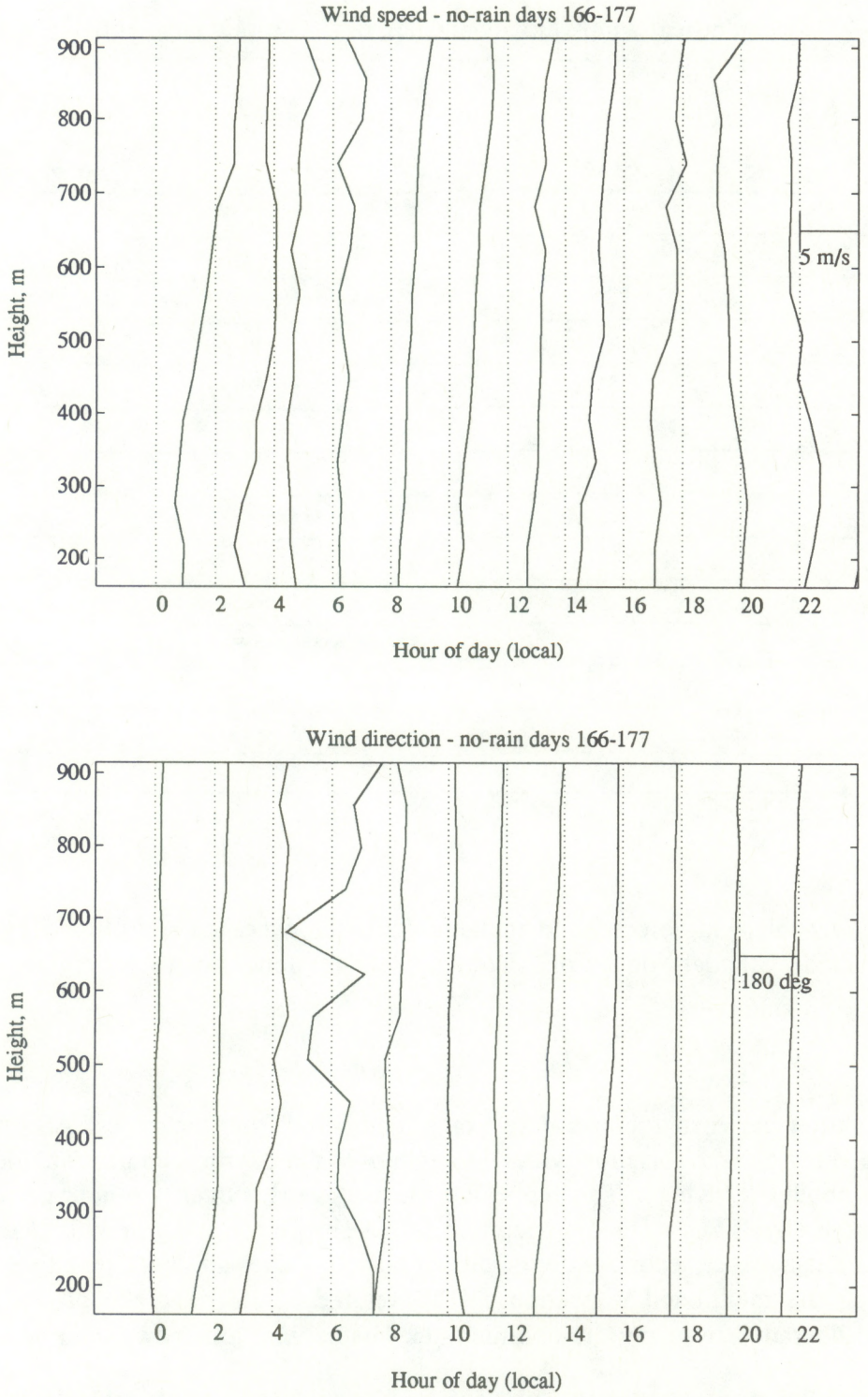

Figure 5.1: Horizontal wind speed and direction profiles for 2-h time bins averaged over 9 rain-free days during 13-24 June 1991 (see text). Dotted: zero reference for each time. In the direction plot, zero is northward.

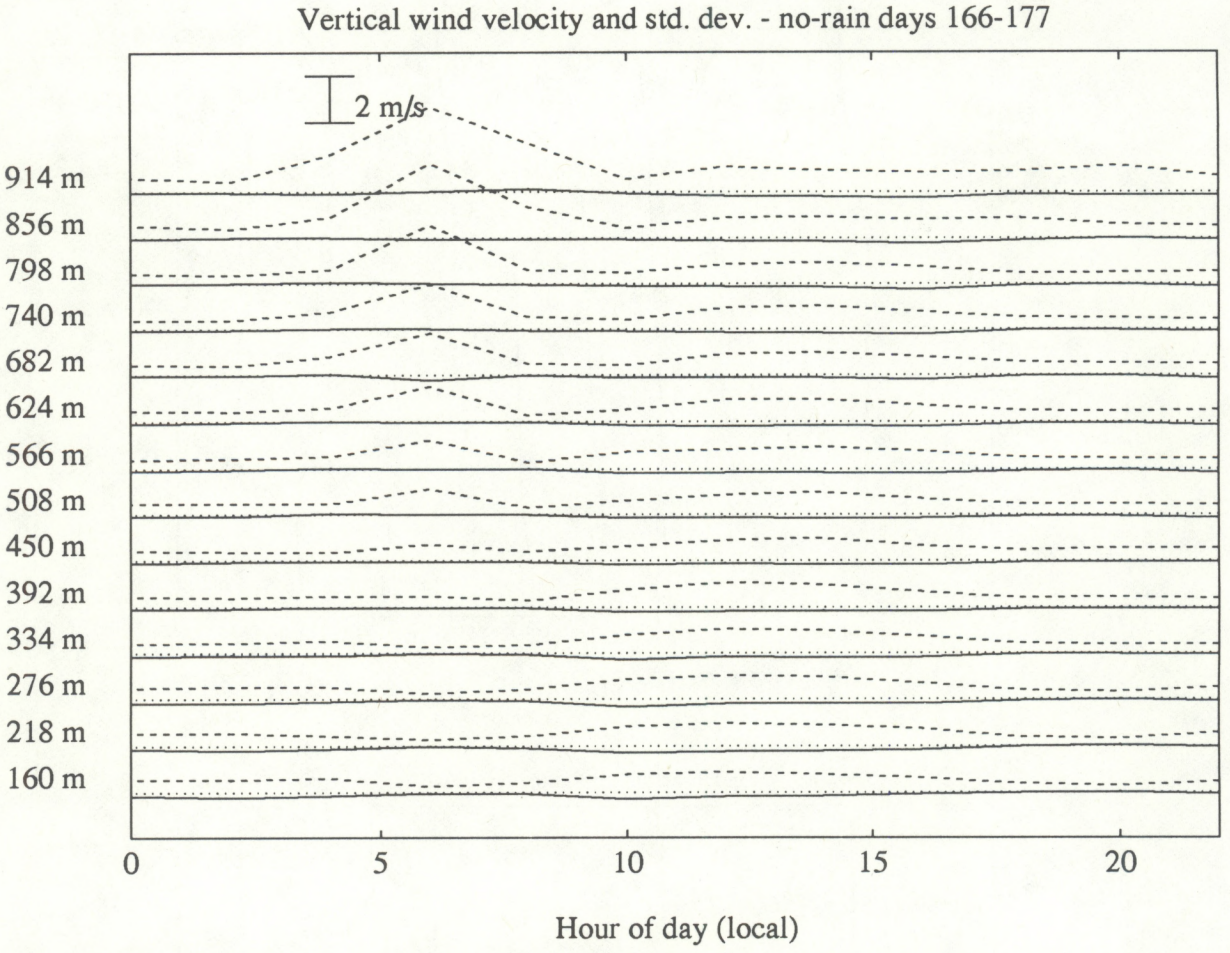

Figure 5.2: Vertical wind velocity and standard deviation averaged as in Fig. 5.1. Solid: Mean velocity. Dashed: Standard deviation. Dotted: Zero reference for each height.

resolvable by the profiler/RASS.

Figure 5.4 shows the virtual temperature flux as computed from the radar/RASS measurements. The time series show a clear variation with sun angle over the daytime hours. The peak flux at the lowest height is about 0.12 Kms^{-1}. This represents the average flux over two-hour periods at midday, averaged over nine days. The virtual temperature flux is shown for fewer heights than the wind and temperature profiles because second-order quantities such as fluxes are more sensitive to data quality and availability. As mentioned in section 5.1 above, the height coverage of the RASS in this experiment was degraded by using the oblique radar beams with a narrow-beam acoustic source.

5.2.4 Momentum flux

The turbulent vertical flux of horizontal momentum (equation 2.9) on scales larger than the radar resolution volume is computed by the method of Vincent and Reid (1983) as discussed in chapter

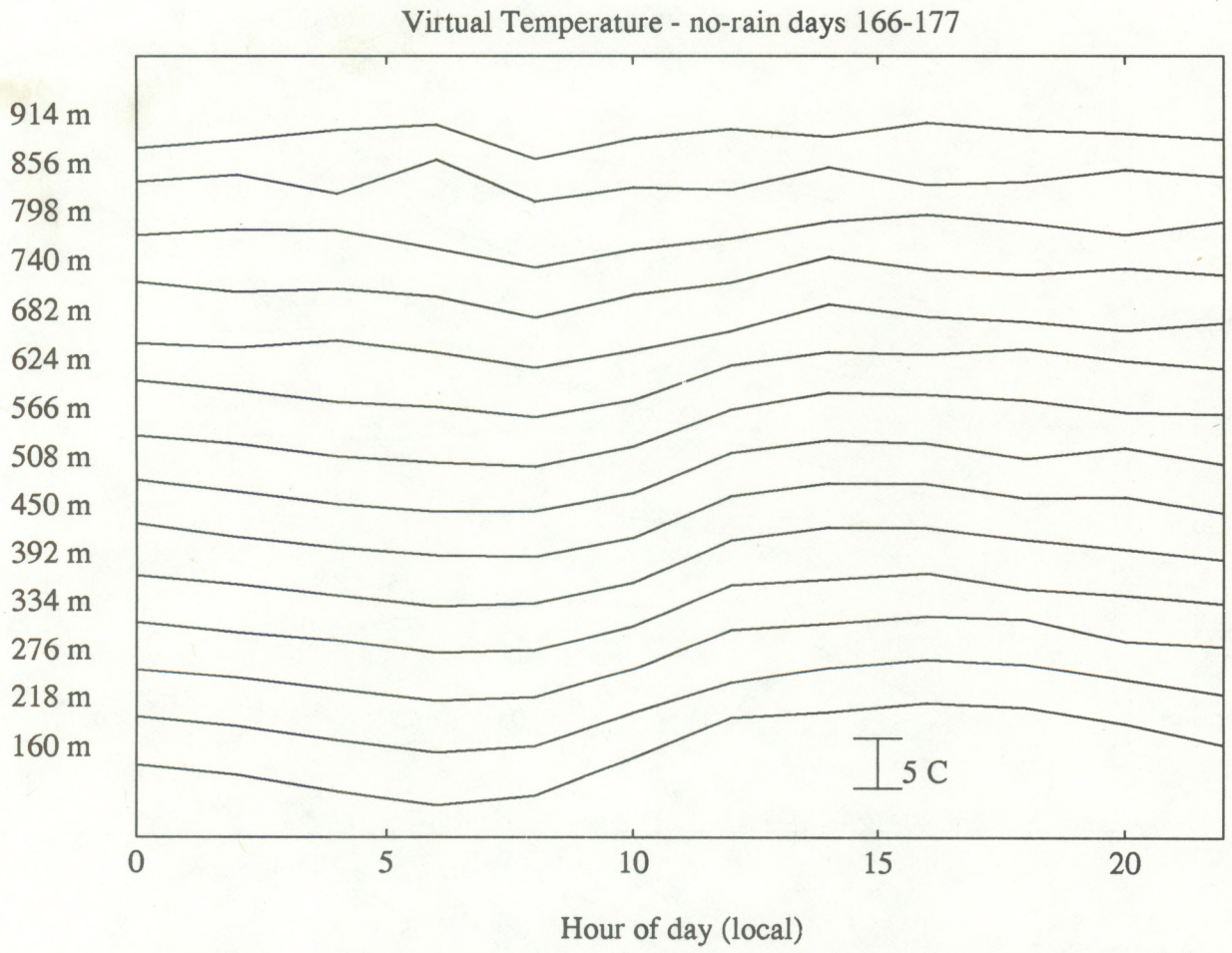

Figure 5.3: Virtual-temperature time series averaged as in Fig. 5.1. Each height is offset by 5° C. The horizontal axis represents 15° C at the lowest height.

4, equation 4.2. This method uses the difference of the velocity variance measured by two beams aimed at the same zenith angle and opposite azimuth angles. The velocity variance is governed by the mean motion of all the scatterers (in this case, refractive index fluctuations) in the volume illuminated by the radar. The Reid technique (Reid 1987) (equation 4.3) is used to compute the sub-resolution momentum flux by subtracting the mean spectral widths of the two coplanar beams. Figure 5.5 shows the momentum flux for the component aligned with the wind and the component across the wind (+90 degrees from the wind direction.) The wind direction used is the average over the three lowest radar range heights for each two-hour period. The flux is calculated for time scales longer and shorter than the radar sampling time (and therefore also for length scales larger and smaller than the radar resolution volume.) The longest scale represented is limited by the two-hour time window. Figure 5.5a shows the fluxes for scales larger than the radar resolution, figure 5.5b is for smaller scales, and figure 5.5c is the total flux on all scales less than two hours. The total flux is the sum of the large and small scale fluxes. The solid lines are computed from the clear air wind velocities, and the dashed lines are computed from the acoustic velocities measured by the RASS.

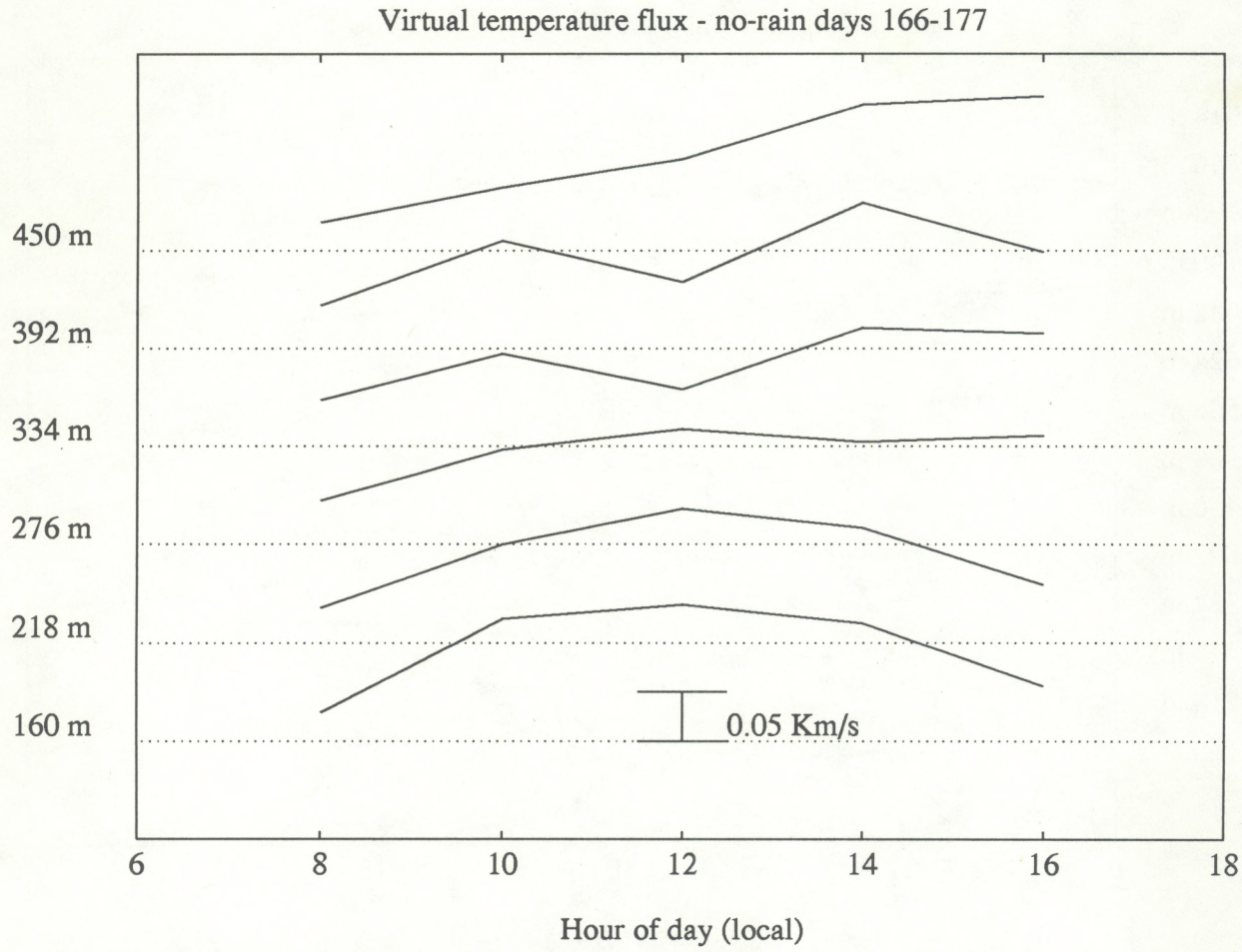

Figure 5.4: Virtual temperature flux for the lowest six heights. The dotted line is the zero reference for each height. Each height is offset by 0.1 Kms^{-1}.

Six heights are plotted for the acoustic-derived fluxes, although the higher heights are less reliable. The fluxes are plotted only for the middle of the day. The measurements at other times are not reliable because of low reflectivity.

The flux of momentum in the direction of the surface wind is expected to be negative (downward), and the results shown here support that expectation. The wind-aligned component is generally negative. The crosswind component is often significant. This non-negligible magnitude may be because the wind direction used to resolve the two components is that at 160-330 m, not at the surface.

The agreement between the fluxes computed from the clear-air and acoustic velocities is sometimes good, especially in the superresolution crosswind component. At other times and in the wind-aligned component, the acoustic measurement differs substantially from the clear-air measurement. Several reasons could account for this discrepancy. These are two largely

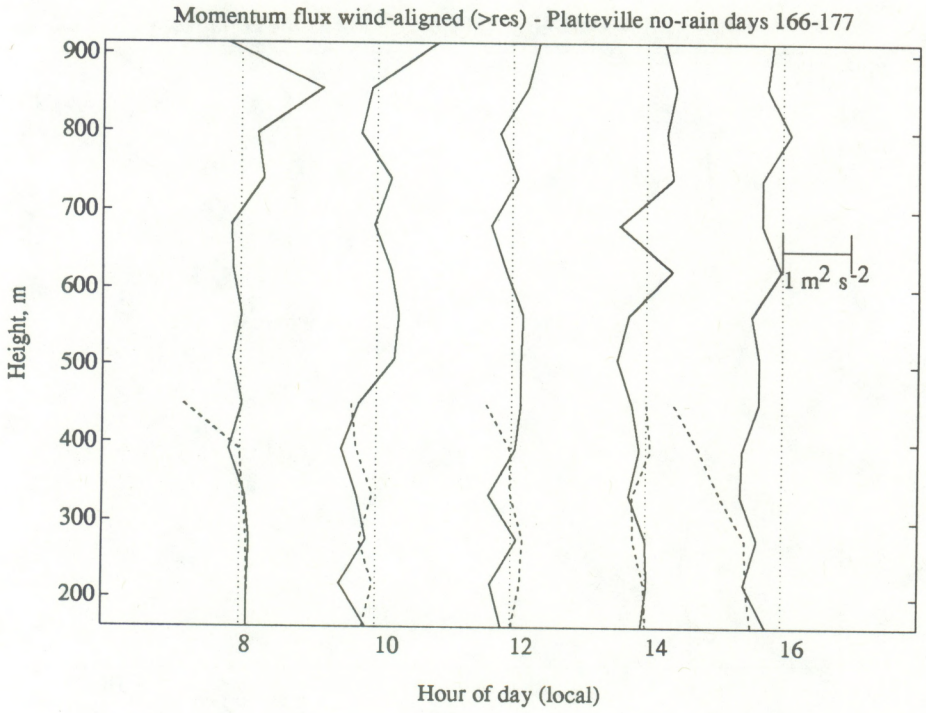

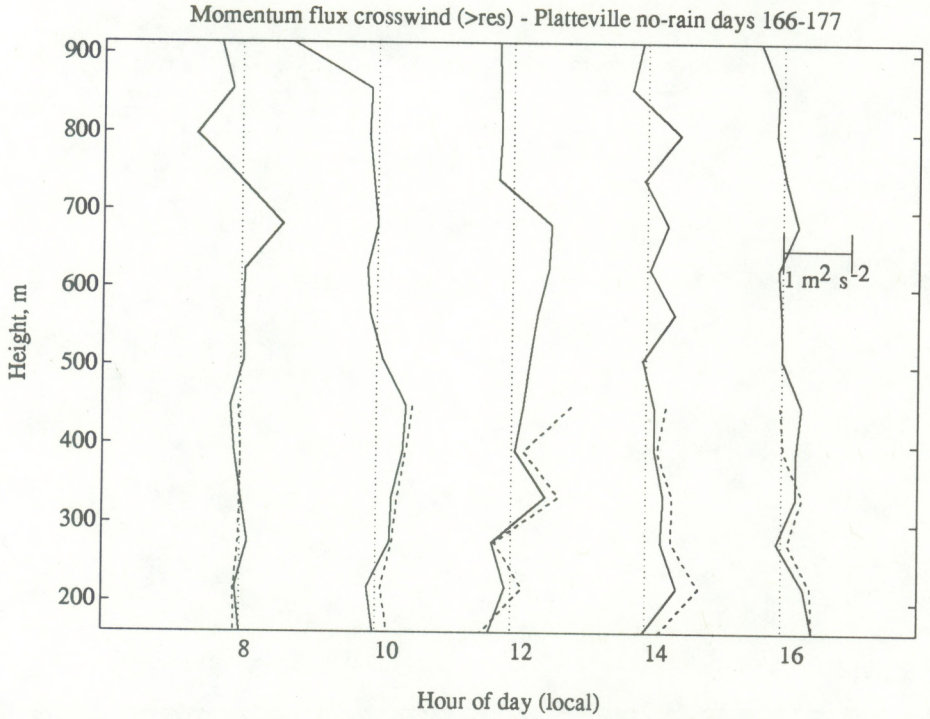

Figure 5.5a: Momentum flux on scales greater than the profiler resolution cell size. Solid lines are computed from the clear-air velocities; dashed lines are computed from the acoustic (RASS) velocities.

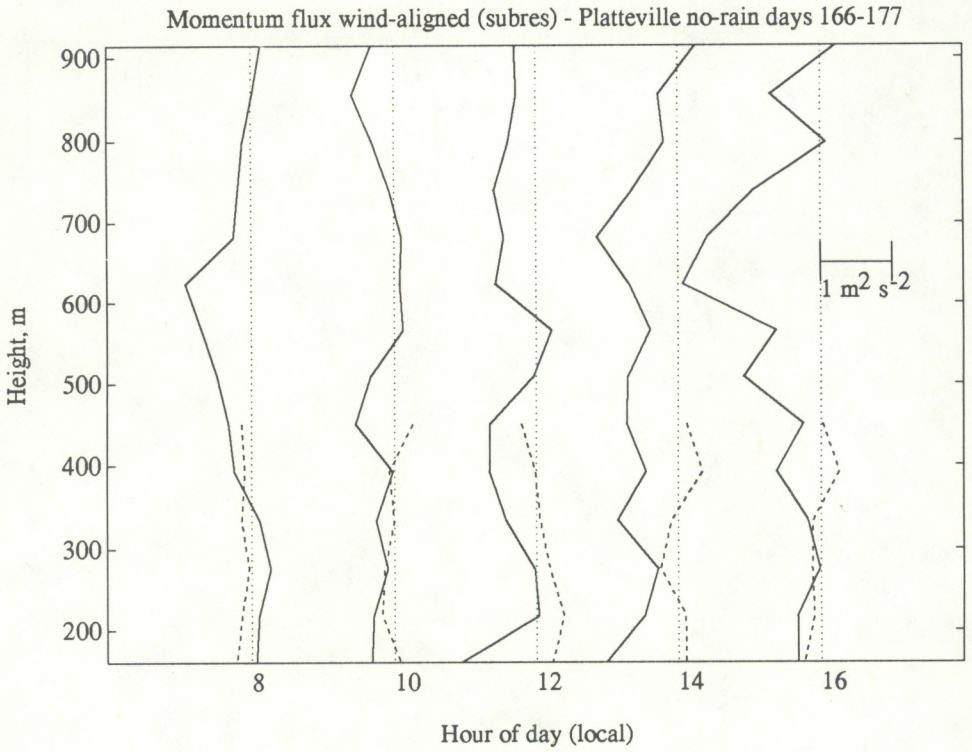

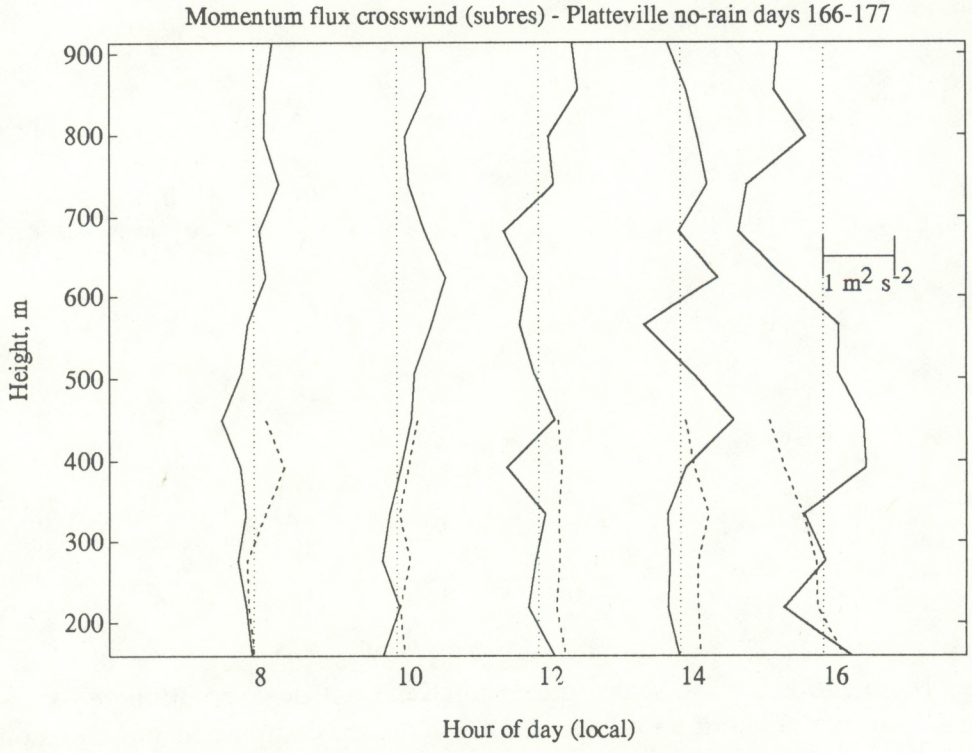

Figure 5.5b: Momentum flux on scales less than the resolution cell size.

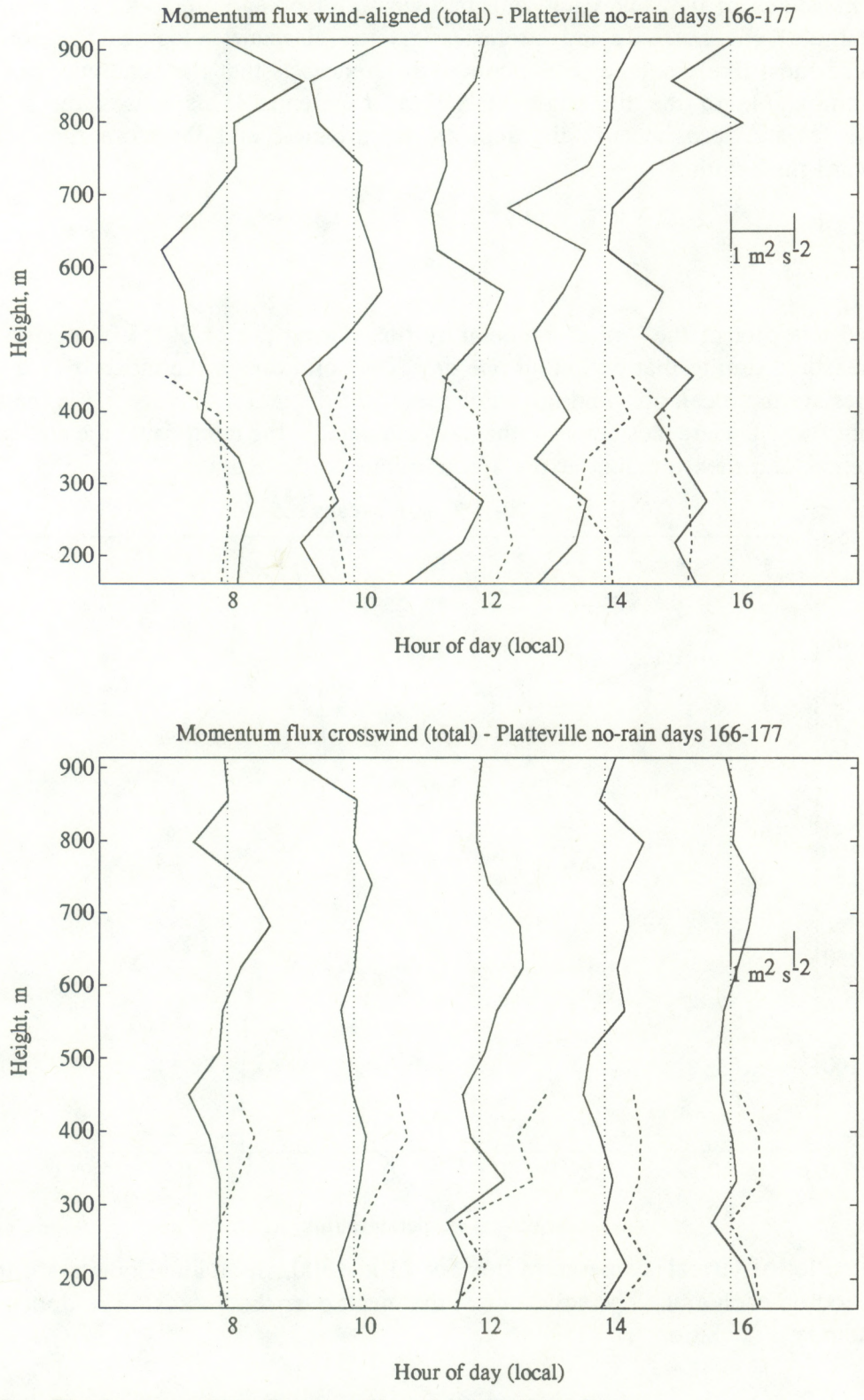

Figure 5.5c: Total momentum flux on all scales less than 2 h.

independent measures of the flux, each with its own set of potential errors. For example, ground clutter and targets such as birds and aircraft affect the clear-air velocities but not the acoustic velocities. The most likely source of systematic differences is that the beamwidth of the acoustic sources is comparable to the tilt angle of the radar antenna. This biases the RASS velocity measurements toward zero because the acoustic disturbance, and therefore the radar return, is strongest toward the zenith.

5.3 Error Analysis

Figure 5.6 is a plot of the virtual temperature flux during the 11:00-13:00 period. Each point is the flux measured during that period on one day. The solid line is the mean over the 9 days, and the dotted lines are the mean plus and minus one standard deviation. Figure 5.7 is the same plot for the momentum flux. Differences between the days included in the composite, the statistical behavior of the turbulence, and measurement errors all contribute to the scatter.

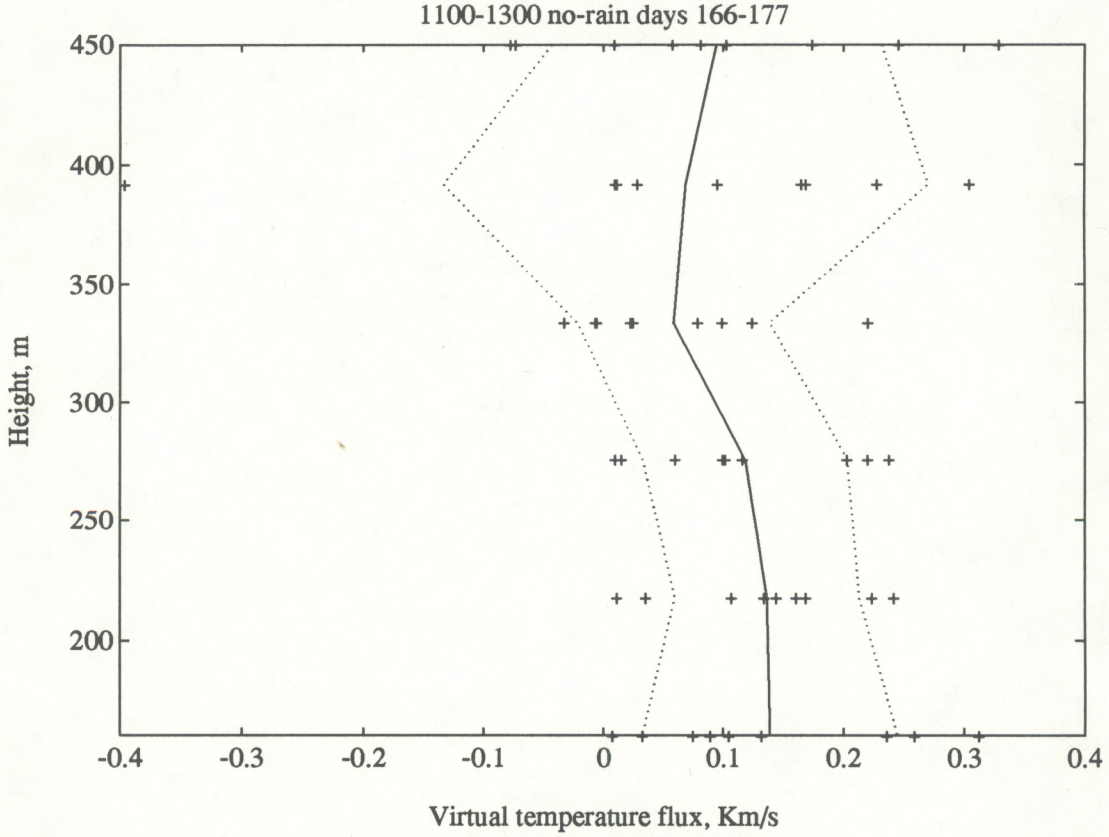

Figure 5.6: Plot of virtual temperature flux for 1100-1300. Individual points are the values for the 2-h period on each day. The solid line is the mean over the 9 days. The dotted lines are the mean ±1 standard deviation.

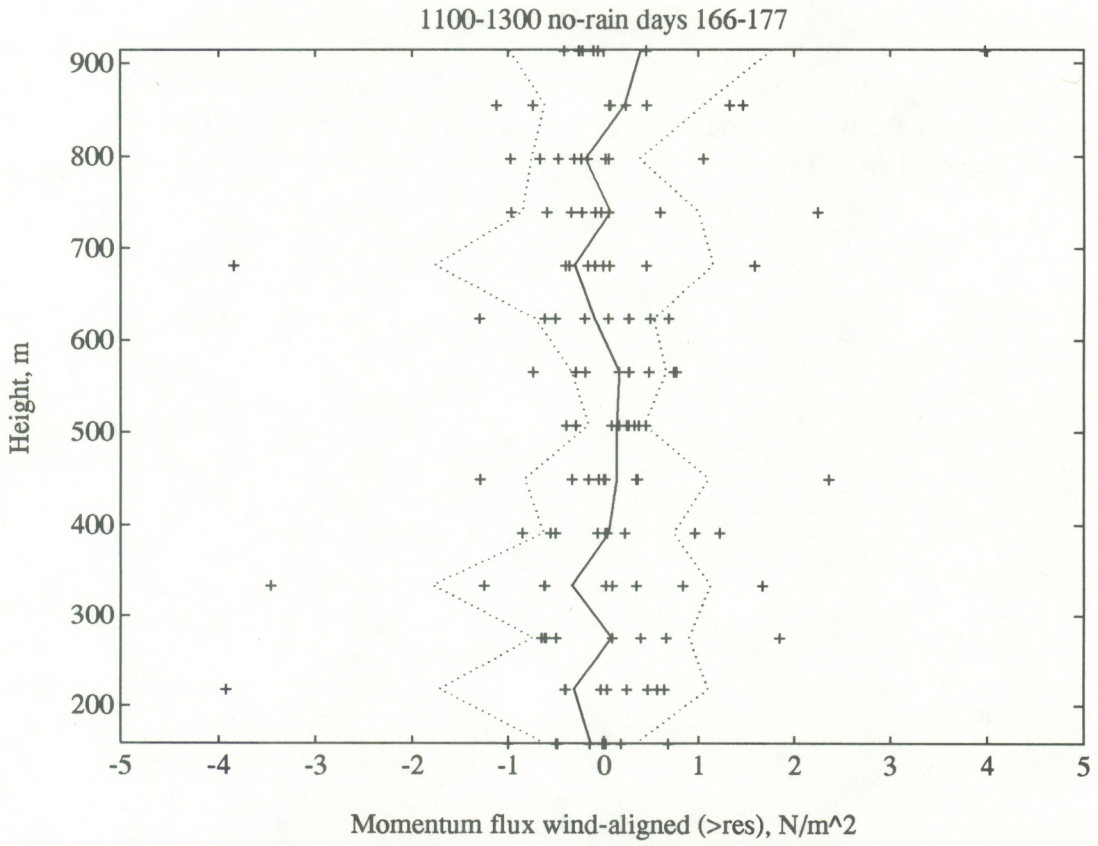

Figure 5.7: Plot of momentum flux for 1100-1300. Individual points are the values for the 2-h period on each day. The solid line is the mean over the 9 days. The dotted lines are the mean ±1 standard deviation.

The uncertainty due to sampling was discussed in chapter 2 (equation 2.14). We can make a rough estimate of the sampling uncertainty for these data. For the results presented here, t is 18 hours (2 hours on each of 9 days). Taking the integral scale in space to be 100 m, using the measured mean wind to convert this to the time integral scale τ, and computing F from the mean fluxes in the 11:00-13:00 period, we derive a relative uncertainty of 0.4 for the virtual temperature flux and 0.6 for the momentum flux on scales greater than the radar resolution. In other words, the expected standard deviation due solely to atmospheric variability is 40% of the mean for the virtual temperature flux and 60% of the mean for the momentum flux. This is only an estimate of the sampling uncertainty because we do not have a direct measurement of the integral scale (which would be subject to similar uncertainty) and because the estimate depends on the uncertain measurement itself. It is nonetheless suggestive that the error estimated by this method is comparable to the standard deviation shown on the scatter plots. The uncertainties inherent in the measurement of heat and momentum flux will be explored further in chapter 6 using the more complete ROSE II data set.

5.4 Summary

We found the Platteville results shown above to be quite encouraging, and therefore proceeded to plan and execute a study that would let us compare flux results with an established technique. That study is presented in chapter 6.

6. ROSE II Results

In previous chapters we described data analysis procedures and preliminary measurements of heat and momentum flux in the convective atmospheric boundary layer using the boundary layer profiler radio acoustic sounding system (profiler/RASS). The Platteville experiment (chapter 5) established the feasibility of making heat and momentum flux measurements with the profiler/RASS. The key question remaining was whether the measurements were accurate. As part of the Rural Oxidants in the Southern Environment II (ROSE II) experiment, an aircraft and a surface sonic anemometer made flux measurements for comparison to the profiler/RASS measurements. In this chapter, we discuss the heat flux and momentum flux results from the profiler/RASS and compare them to fluxes measured by the two more traditional techniques. In addition, we present a technique for determining the boundary layer height from the profiler data and compare it with radiosonde soundings. The results presented in this chapter have been published (Angevine et al., 1993b).

6.1 Experiment description

The ROSE II experiment was conducted in a rural area of Alabama during June, 1992. As the name indicates, ROSE II was primarily an atmospheric chemistry experiment, exploring the processes that contribute to ozone formation in the rural Southeast. The experiment site was within a managed pine forest, sections of which had been cut and replanted at various times leaving a patchwork of various sizes of trees. The profiler/RASS was located in an area that had been cleared about four years earlier and had pine trees about 2 m high and other lower brush.

The profiler/RASS operated continuously from 9 June through 3 July. The King Air aircraft from the National Center for Atmospheric Research (NCAR) Research Aviation Facility made several research flights over the ROSE II site during 10-25 June. Table 6.1 shows characteristics of the flight legs selected for this study, and figure 6.1 shows the flight tracks superimposed on a map of the site, including surrounding towns, the Mississippi-Alabama border, and the Tombigbee river. The two flight tracks running east-west are flights 8A and 10B. A sonic anemometer operated by the Atmospheric Turbulence and Diffusion Division (ATDD) of the National Oceanic and Atmospheric Administration Air Resources Laboratory on a tower just above the forest canopy near the profiler/RASS site operated from 18-26 June. A Cross-chain Loran Atmospheric Sounding System (CLASS) provided by the National Center for Atmospheric Research (NCAR) was collocated with the profiler for balloon-borne pressure, temperature, humidity, and wind soundings. Forty-eight sondes were flown, three to six per day during 16-23 June.

The profiler/RASS was described in chapter 3. For ROSE II, the profiler sampled each beam position for 30 s and then spent 10 s performing calculations and allowing the mechanically steered antenna to move and stabilize. Therefore a temperature profile was available every 40 s. The range resolution was 100 m and the lowest range gate was centered at 150 m. The profiler/RASS and aircraft data were processed as described in chapter 4.

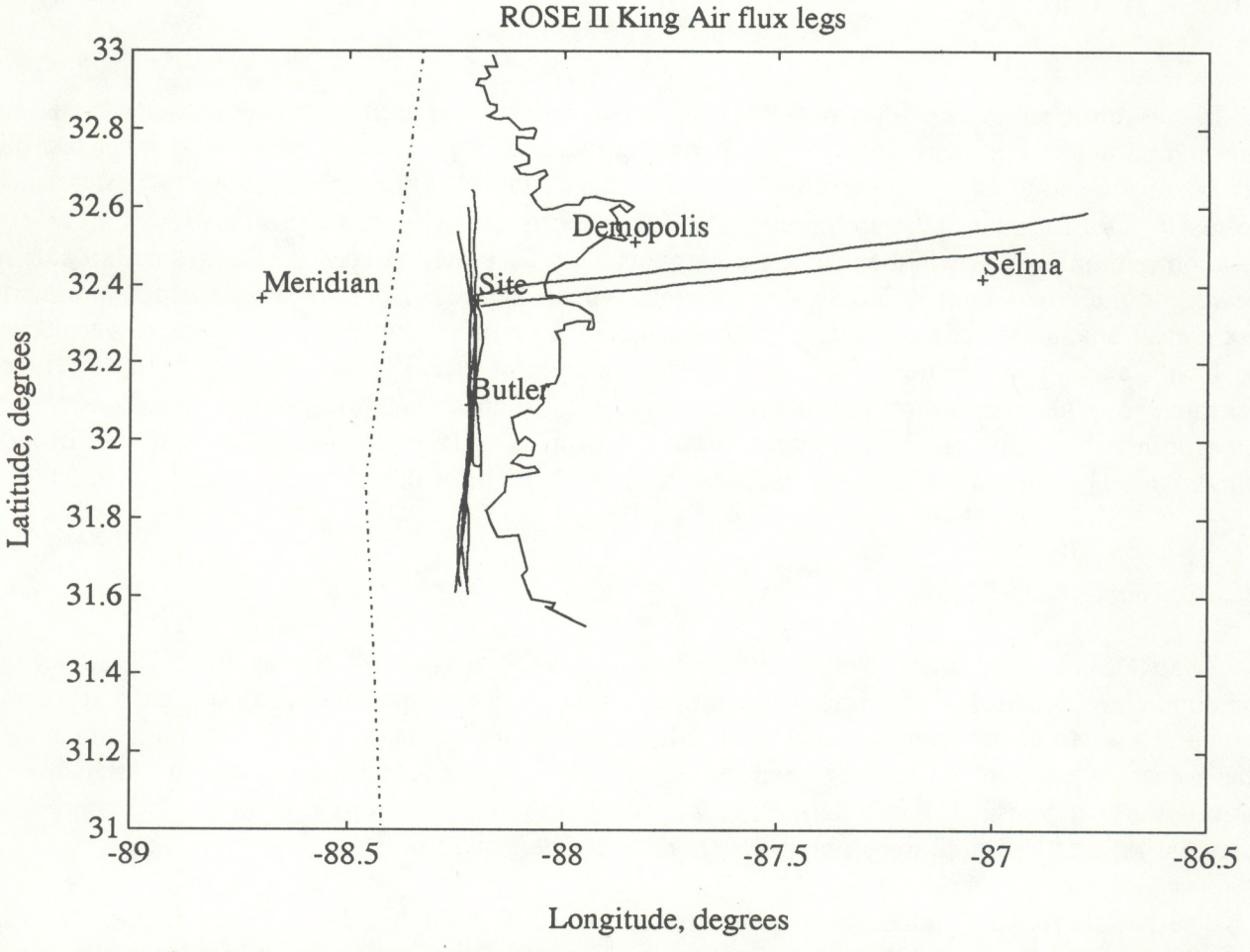

Figure 6.1: Site vicinity map showing King Air flight tracks and nearby towns. Dash-dot line is the Mississippi-Alabama border. Irregular line is the Tombigbee river. The east-west legs are 8A and 10B.

Table 6.1: Characteristics of King Air flight legs.

Leg	Date	Start time, CST	Duration, min	Height AGL, m
6D	18 June	1222	17	160
7A	20 June	0959	21	380
7B	20 June	1022	19	250
7C	20 June	1048	22	170
7D	20 June	1112	17	80
8A	21 June	0911	25	180
10A	23 June	0906	10	160
10B	23 June	1014	29	170

6.2 Meteorological conditions

In this section we briefly describe the general meteorological conditions during the 18-25 June period at ROSE II. Figure 6.2 is a vector plot of 6-hour average winds measured by the profiler. The afternoon winds in the boundary layer were generally light but varied in direction on the various days. Winds at night were stronger (5-8 m/s) and generally from the northwest to southwest. Winds above the boundary layer were mostly from the northwest.

Figures 6.3 and 6.4 show the winds for 19 June and 22 June, respectively, in more detail, with half-hour averages. On 19 June the winds within and above the boundary layer are not very different, while there is a strong shear at the boundary layer top on 22 June (see section 6.4). A low-level jet was observed on the night of 21-22 June below approximately 750 m with a maximum speed of approximately 12 m/s, and can be clearly seen between 0000 and 0800 CDT in figure 6.4. Such nocturnal jets are commonly observed over the central United States and are important for chemical transport, among other processes. This jet is somewhat unusual in that it is from the northeast.

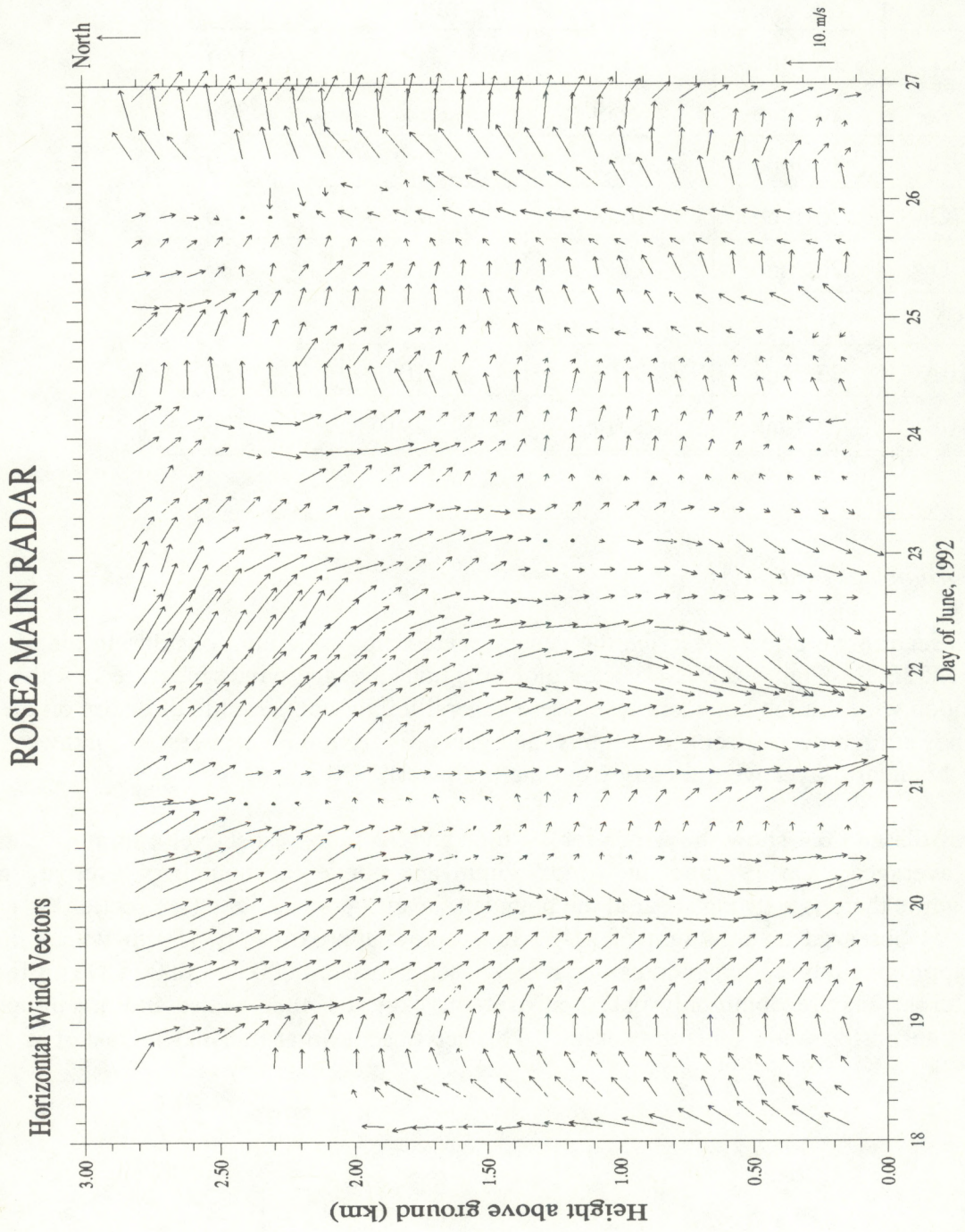

Figure 6.2: Wind vectors from profiler for 18-25 June.

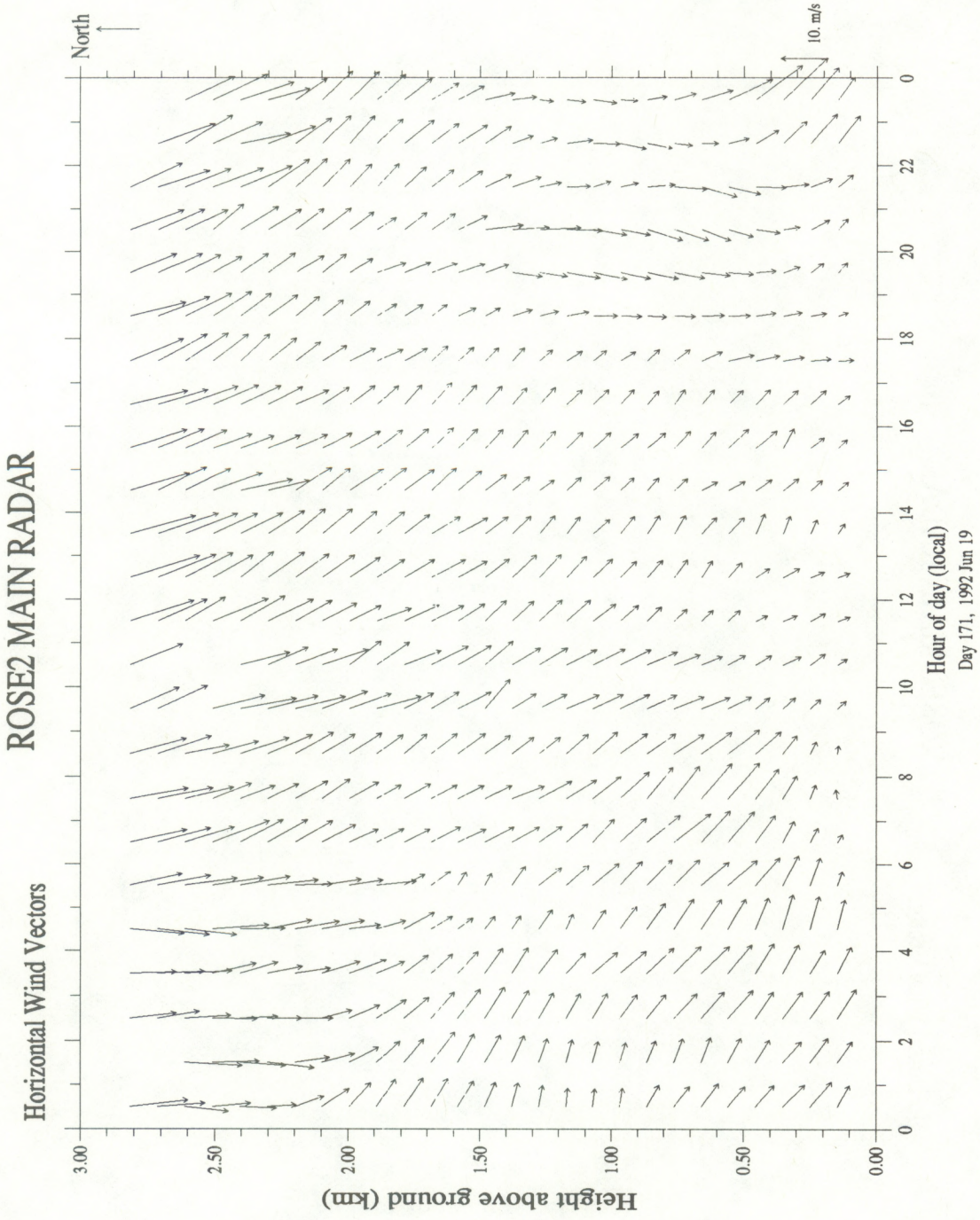

Figure 6.3: Wind vector plot from profiler for 19 June. One-hour average winds are shown.

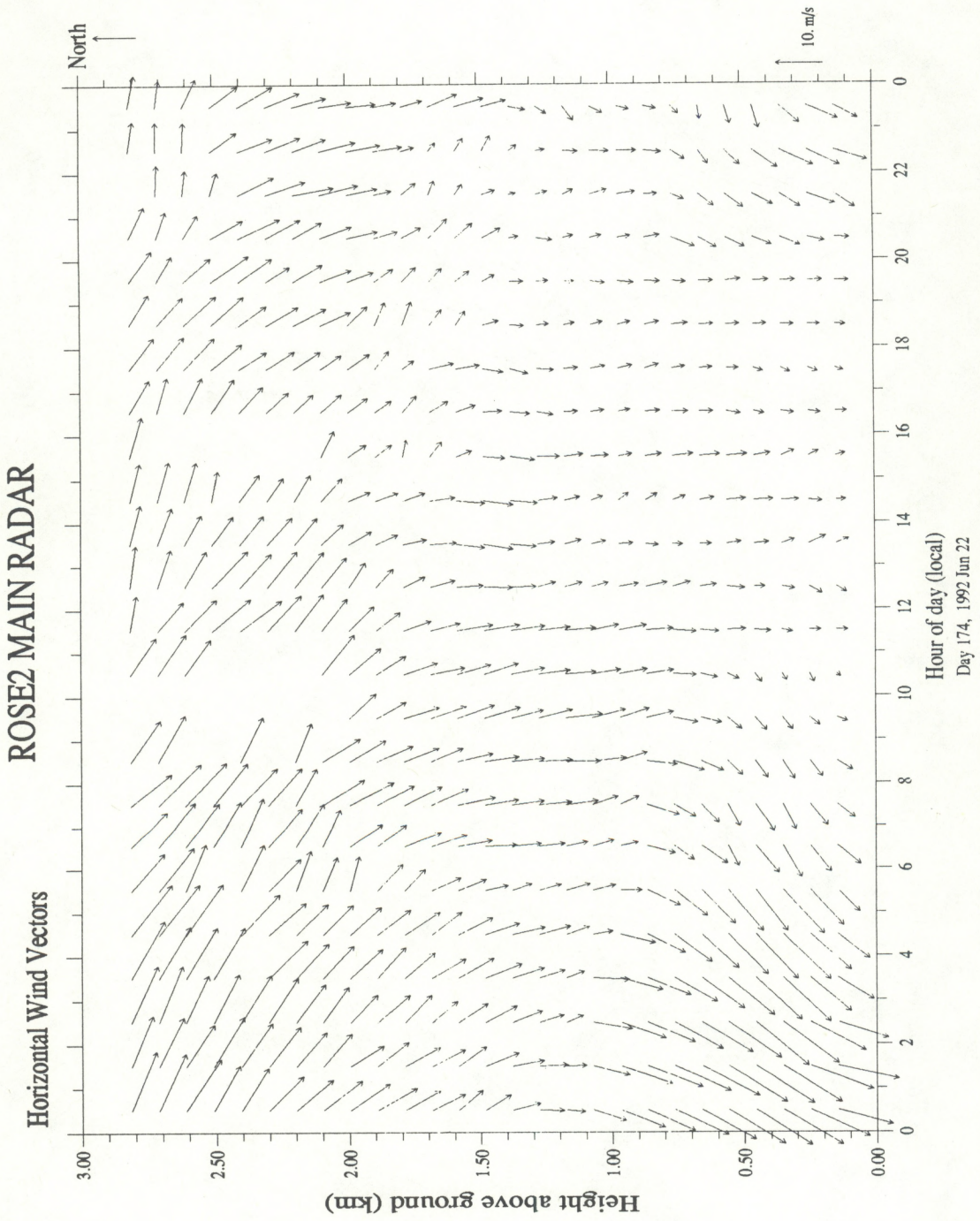

Figure 6.4: Wind vector plot from profiler for 22 June. One-hour averages are shown.

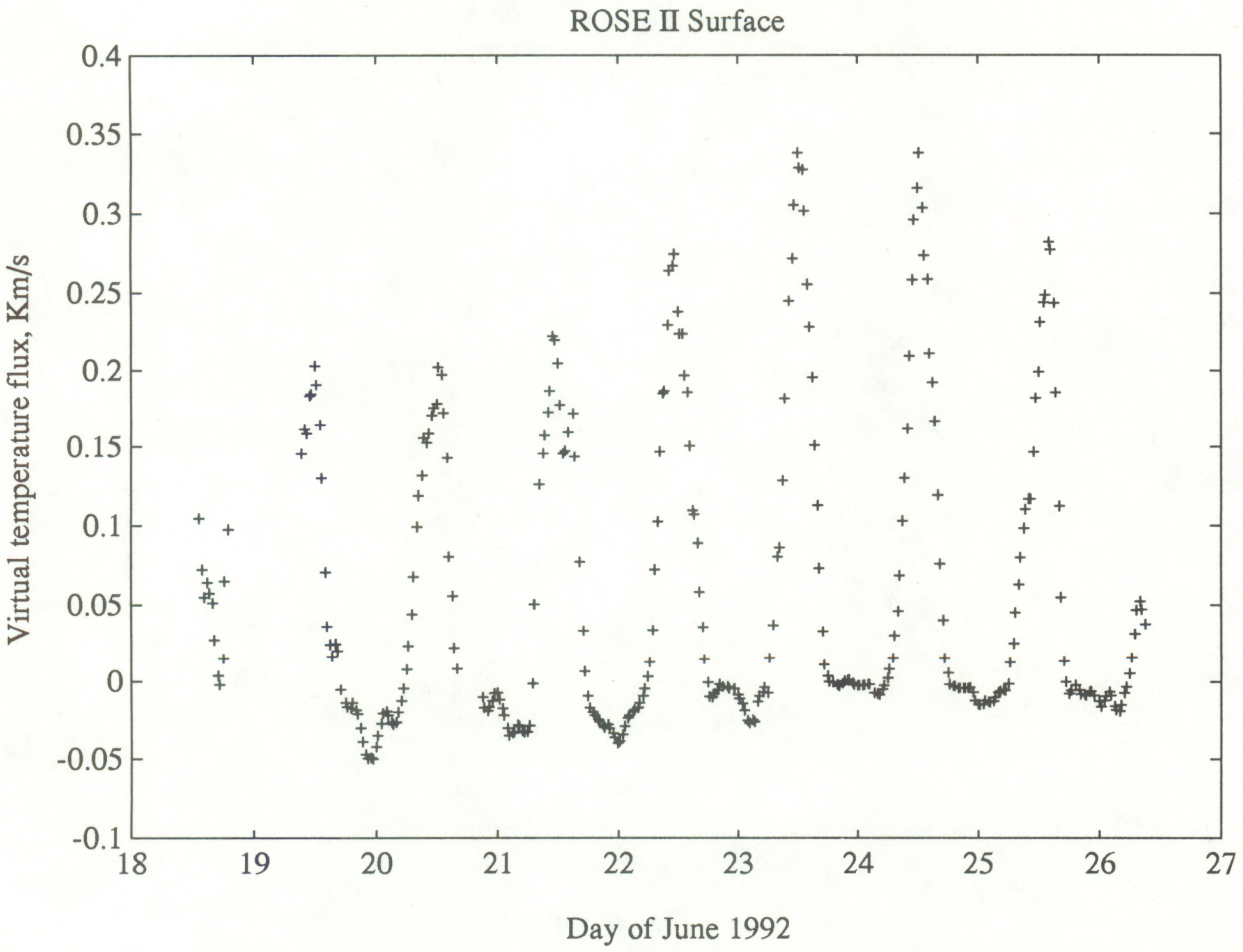

Figure 6.5: Virtual temperature flux measured just above the forest canopy by a sonic anemometer. Two-hour averages on a half-hour grid are shown.

Strong convective turbulence was present throughout the 18-25 June period, as shown in figures 6.5, 6.6, and 6.7, which show turbulence parameters measured by the near-surface sonic anemometer. Figure 6.5 is the surface virtual temperature flux, figure 6.6 is the vertical velocity variance, and figure 6.7 is the friction velocity u* (the square root of the surface stress). All show strong diurnal cycles, which are especially clear after 22 June. The surface virtual temperature flux and friction velocity were used to normalize the fluxes measured by the profiler/RASS and the aircraft, as discussed below.

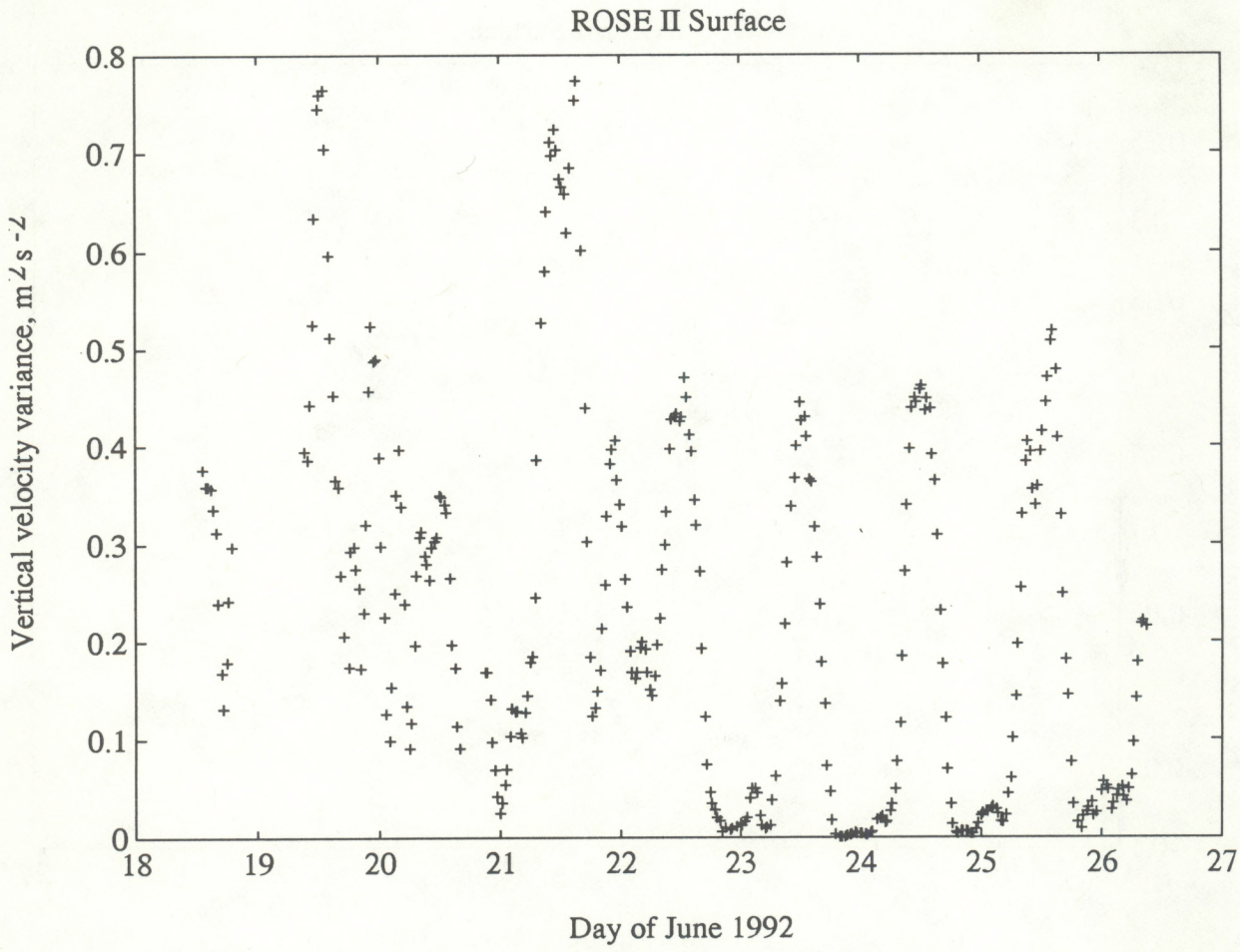

Figure 6.6: Vertical velocity variance measured just above the forest canopy by a sonic anemometer. Two-hour averages on a half-hour grid are shown.

6.3 Heat flux measurements and comparisons

The following sections discuss three different comparisons of the profiler/RASS and aircraft virtual temperature flux measurements. First, aircraft measurements are compared to profiler/RASS flux measurements from individual two-hour periods surrounding the flight time. Because two-hour measurements are subject to considerable sampling uncertainty, the second comparison is between the aircraft measurements and composite multi-day average profiler/RASS fluxes. Finally, average profiles of the normalized flux measured by the aircraft and the profiler/RASS, constructed by least-squares fitting, are compared. The results are discussed after all three comparisons have been presented.

All of the following comparisons use the vertical turbulent virtual temperature flux as defined by equation 2.5, calculated from the profiler/RASS data by the Peters method as described in chapter

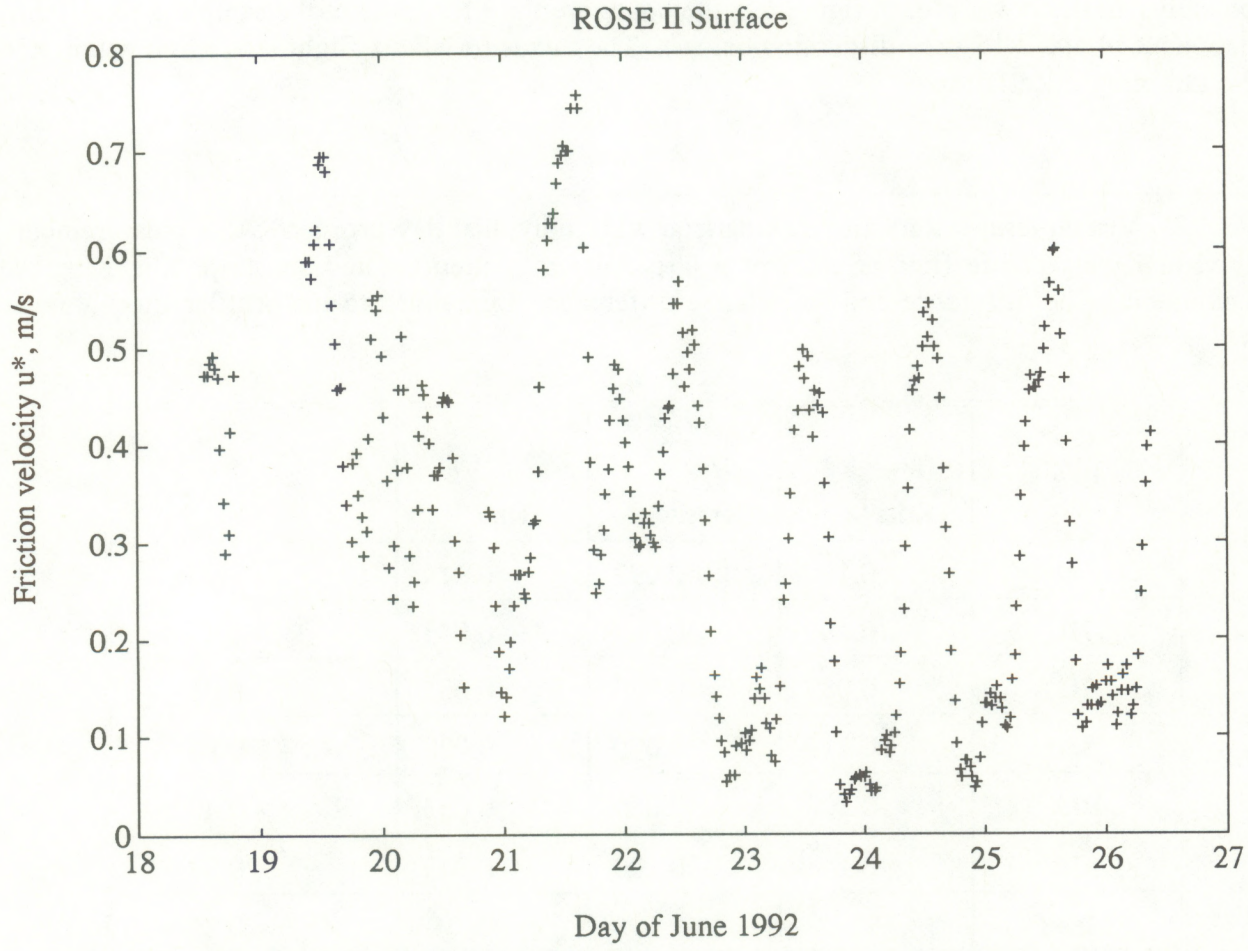

Figure 6.7: Friction velocity u^* measured just above the forest canopy by a sonic anemometer. Two-hour averages on a half-hour grid are shown.

4, equation 4.1. The same flux was also calculated from the aircraft data as described in chapter 4.

6.3.1 Individual day comparisons

In Table 6.2 we compare the virtual temperature flux from six flight legs to that measured by the profiler/RASS at the same time on the same day as the flight. Q_{tp} is the flux measured by the profiler and Q_{ta} is the flux measured by the aircraft. The profiler/RASS flux is interpolated between adjacent 2 h averages. For statistical comparison, the relative difference is used, that is, the difference between the flux measured by the profiler/RASS and that measured by the aircraft normalized to the profiler measurement. The mean relative difference $\overline{\left(\frac{Q_{vp}-Q_{va}}{Q_{vp}}\right)}$ is 0.26, and the standard deviation of the relative difference is 0.18. Figure 6.8 shows the same comparison

graphically. In the lower plot of figure 6.8, the boxes are the ±1σ limits of the sampling uncertainty (equations 2.14 and 2.15 - see discussion below). The fluxes for all six flight legs agree within ±1σ of the sampling uncertainty.

Table 6.2: Virtual temperature flux comparison with individual day profiler/RASS measurements. Q_t is virtual temperature flux. Subscript p is profiler measurement and subscript a is King Air measurement. The difference and the relative difference (normalized to the profiler flux) are also shown.

Leg	Q_{tp} Kms^{-1}	Q_{ta} Kms^{-1}	$Q_{tp}-Q_{ta}$ Kms^{-1}	$\frac{Q_{tp}-Q_{ta}}{Q_{tp}}$
6D	0.106	0.092	0.014	0.13
7B	0.107	0.063	0.043	0.41
7C	0.089	0.089	-0.001	-0.01
8A	0.117	0.090	0.027	0.23
10A	0.108	0.055	0.053	0.49
10B	0.148	0.100	0.047	0.32
Mean				0.26
Std.Dev.				0.18

6.3.2 Multi-day average comparison

In order to reduce the sampling uncertainty, we must average over a longer time period. We cannot simply use a longer period on the same day, since the strong diurnal cycle changes the turbulence characteristics. Therefore, we average the results for the same time period on several days. To reduce the variation from day to day, we scale (normalize) the flux for each 2 h period to the surface flux for that same period. In figure 6.9 we compare the virtual temperature flux for five flight legs near 150 m above ground level (AGL) with the profiler/RASS virtual temperature flux in the range gate centered at 150 m AGL averaged over the period 18-25 June. Each 1 h point of the profiler/RASS measurement is an average of the 2 h measurements centered at the indicated time for all days of the period on which surface data were available at that time. Therefore each point is an average over 5-7 days of 2 h measurements. The dotted lines are the ±1σ sampling uncertainty (equation 2.14 - see discussion below) for the profiler, and the vertical bars are the same for the aircraft legs (equation 2.15).

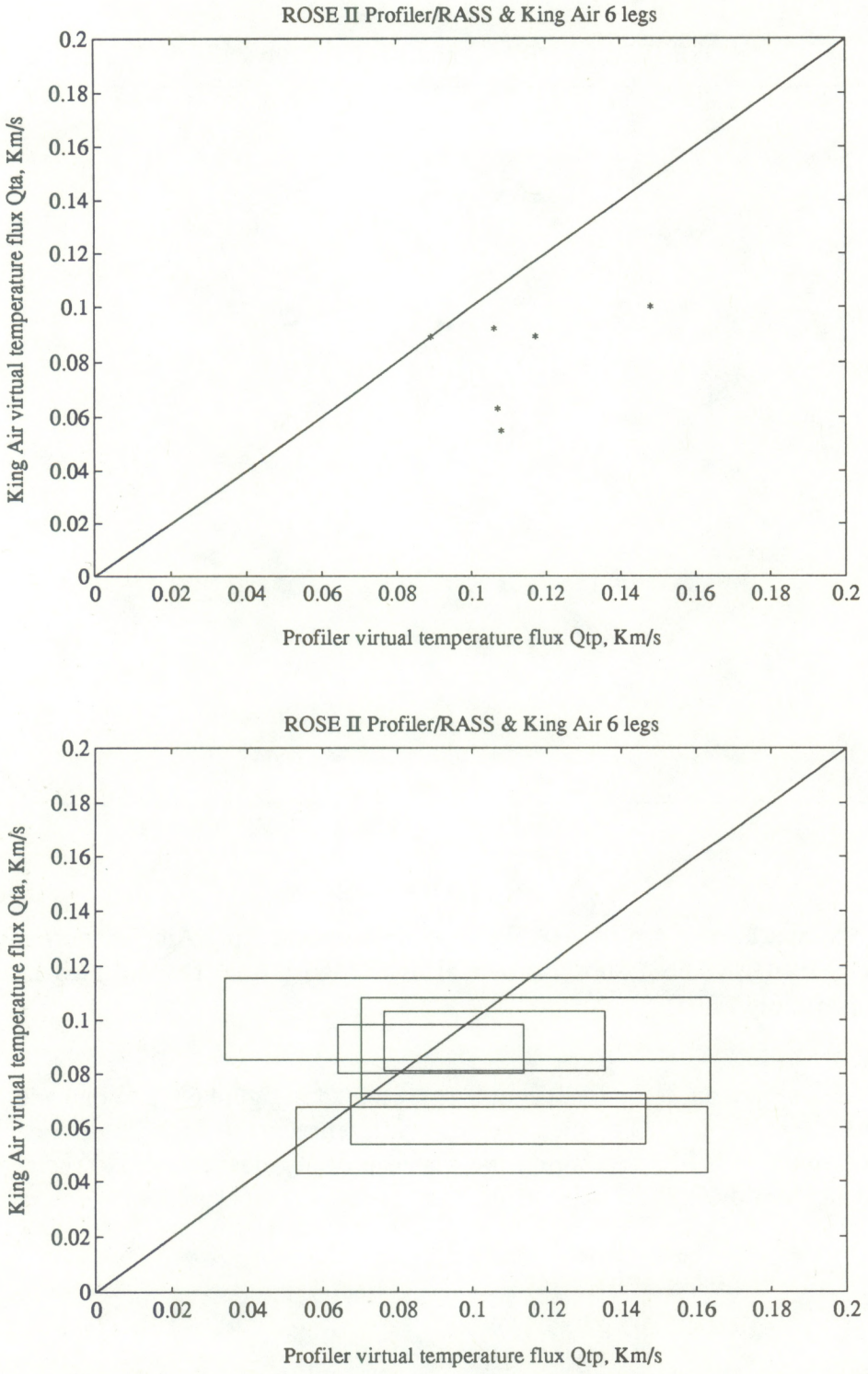

Figure 6.8: Individual day comparisons of profiler/RASS and King Air virtual temperature flux. The solid line is 1:1. The measurements are shown in the upper plot. In the lower plot, the $\pm 1\sigma$ limits of the sampling uncertainty are shown.

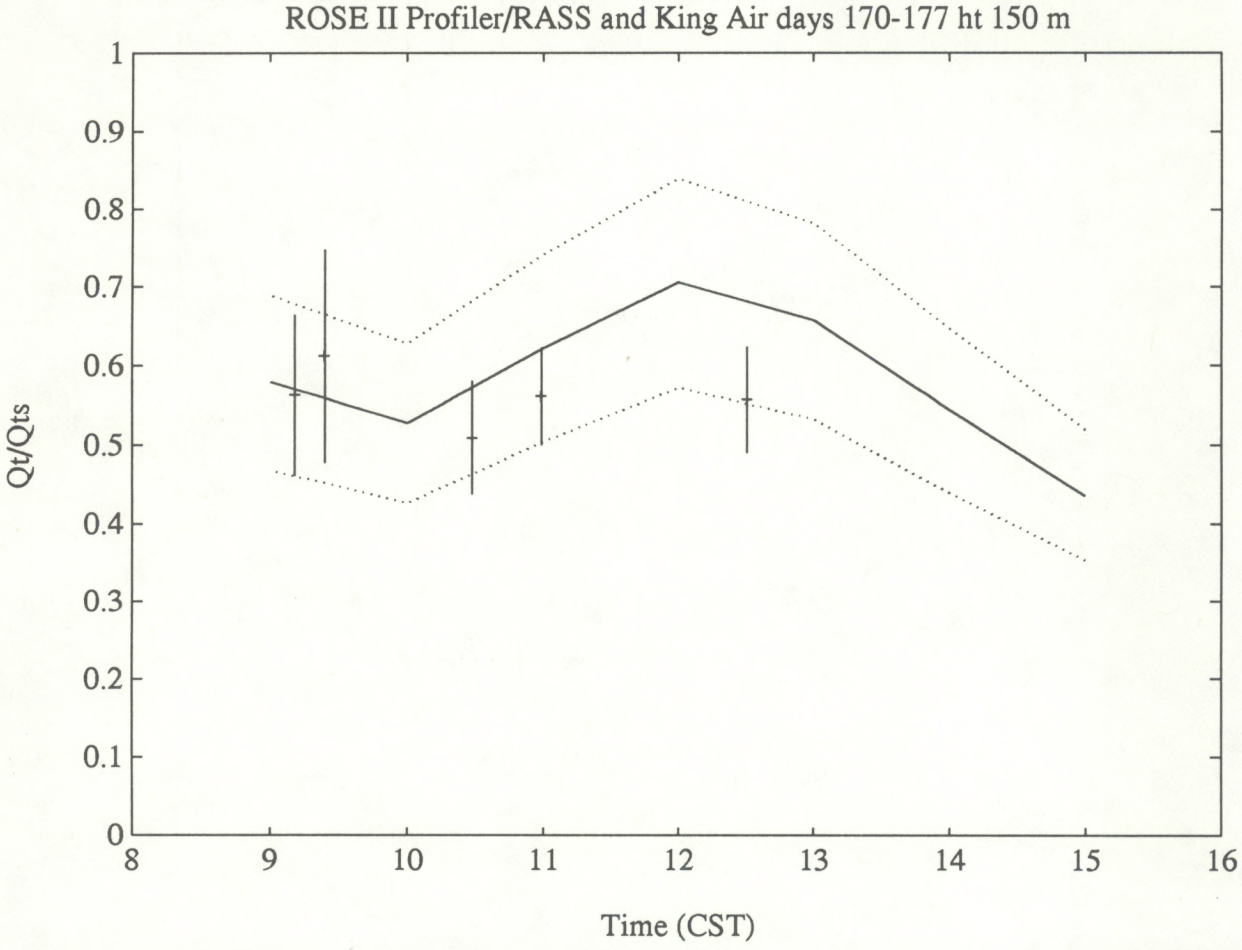

Figure 6.9: Comparison of profiler/RASS 7-day average and King Air flux normalized to surface flux. Solid: Profiler/RASS. Short horizontal lines: King Air. Dotted lines and vertical bars: Sampling uncertainty ($\pm 1\sigma$).

A numerical comparison of the five flight legs presented in figure 6.9 and one additional leg (7B) at 250 m appears in table 6.3. The mean relative difference is 0.09 and the standard deviation of the relative difference is 0.14. Averaging the scaled profiler measurements thus reduces both the systematic and random differences with respect to the aircraft measurements.

Table 6.3: Scaled virtual temperature flux comparison with 7-day average profiler/RASS measurements. Q_t is virtual temperature flux. Subscript p is profiler measurement, subscript s is surface (sonic anemometer) measurement, and subscript a is King Air measurement. The difference and the relative difference (normalized to the profiler flux) are also shown.

Leg	$\frac{Q_{tp}}{Q_{ts}}$	$\frac{Q_{ta}}{Q_{ts}}$	$\frac{Q_{tp}-Q_{ta}}{Q_{ts}}$	$\frac{Q_{tp}-Q_{ta}}{Q_{tp}}$
6D	0.67	0.56	0.11	0.17
7B	0.58	0.41	0.17	0.28
7C	0.62	0.56	0.06	0.09
8A	0.55	0.61	-0.06	-0.11
10A	0.56	0.56	0.00	0.00
10B	0.56	0.51	0.05	0.09
Mean				0.09
Std.Dev.				0.14

Some of the observed scatter in this comparison is explained by the fact that no allowance is made for the differences in PBL height from day to day (equation 2.7). Unfortunately, most of the flight legs were flown in the morning when the boundary layer height was changing rapidly. The earliest leg, leg 10A, was also short, just under 10 minutes.

6.3.3 Fitted profile comparison

As we discussed in chapter 2, the expected profile of virtual temperature flux in the convective mixed layer below about $0.8z_i$ is a straight line (equation 2.7). In this section, we present a comparison of the profiler/RASS and King Air measurements to the straight-line model. The boundary layer height z_i needed for scaling was determined from the profiler SNR (see below).

The measured profiles were determined by unweighted least-squares fitting. The relative height z/z_i was treated as the independent variable, that is, all uncertainty was attributed to the scaled flux measurement. The least-squares procedure acts to average the measurements, reducing the sampling uncertainty. A more straightforward averaging method cannot be used because the measurements occur at many different normalized heights.

Figure 6.10a shows all 2 h average profiler/RASS measurements below $0.8z_i$ during 18-25 June and the line fitted to them. Heights up to 750 m AGL (6 profiler range gates) are represented,

depending on the CBL height. Measurements from 2 h averages centered at times from 0900 through 1200 CST are included, since these encompass the flight times used in the comparison. The correlation coefficient (r) and standard deviation estimate (s) are shown for the fit. The correlation coefficient of -0.37 for the profiler/RASS fit is significant at a confidence level of more than 95%. Figure 6.10b is the same presentation for the 8 King Air flight legs (table 6.1). The correlation coefficient of -0.86 for the aircraft fit is significant at a confidence level of 99%.

Figure 6.11 shows the same fitted lines from figures 6.10a and b, with the addition of two lines from equation 2.7 with $\alpha = 1.2$ and $\alpha = 1.5$. The flux profiles measured by the profiler/RASS and the King Air agree exactly at the surface and differ by only 0.1 at 0.5 z_i. Both appear to underestimate the flux slightly with respect to the surface measurement. Alternatively, the surface flux could be in error.

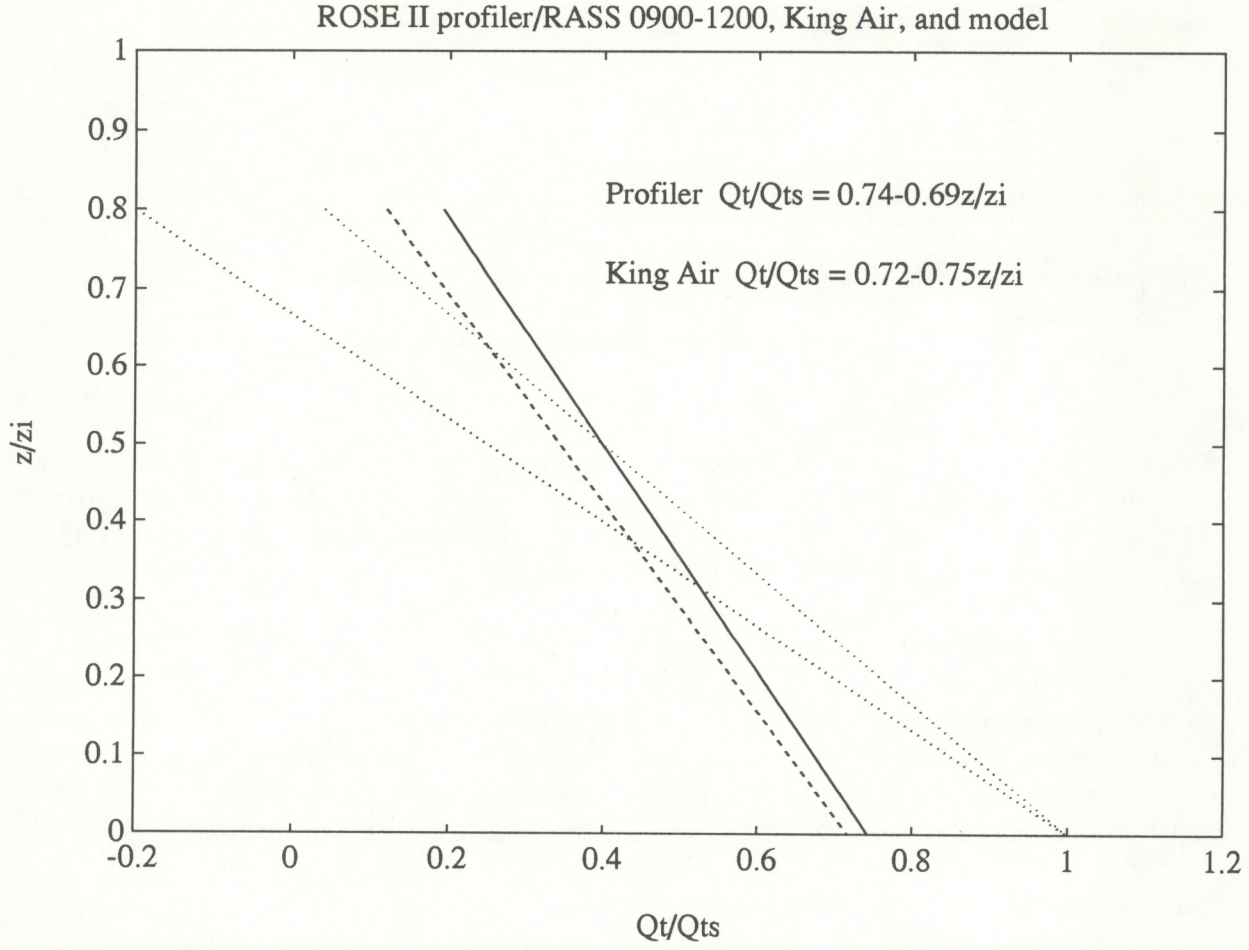

Figure 6.11: Fitted lines for profiler/RASS (figure 6.10a, solid) and King Air (figure 6.10b, dashed) compared to equation 2.7 with α=1.2 and α=1.5 (dotted).

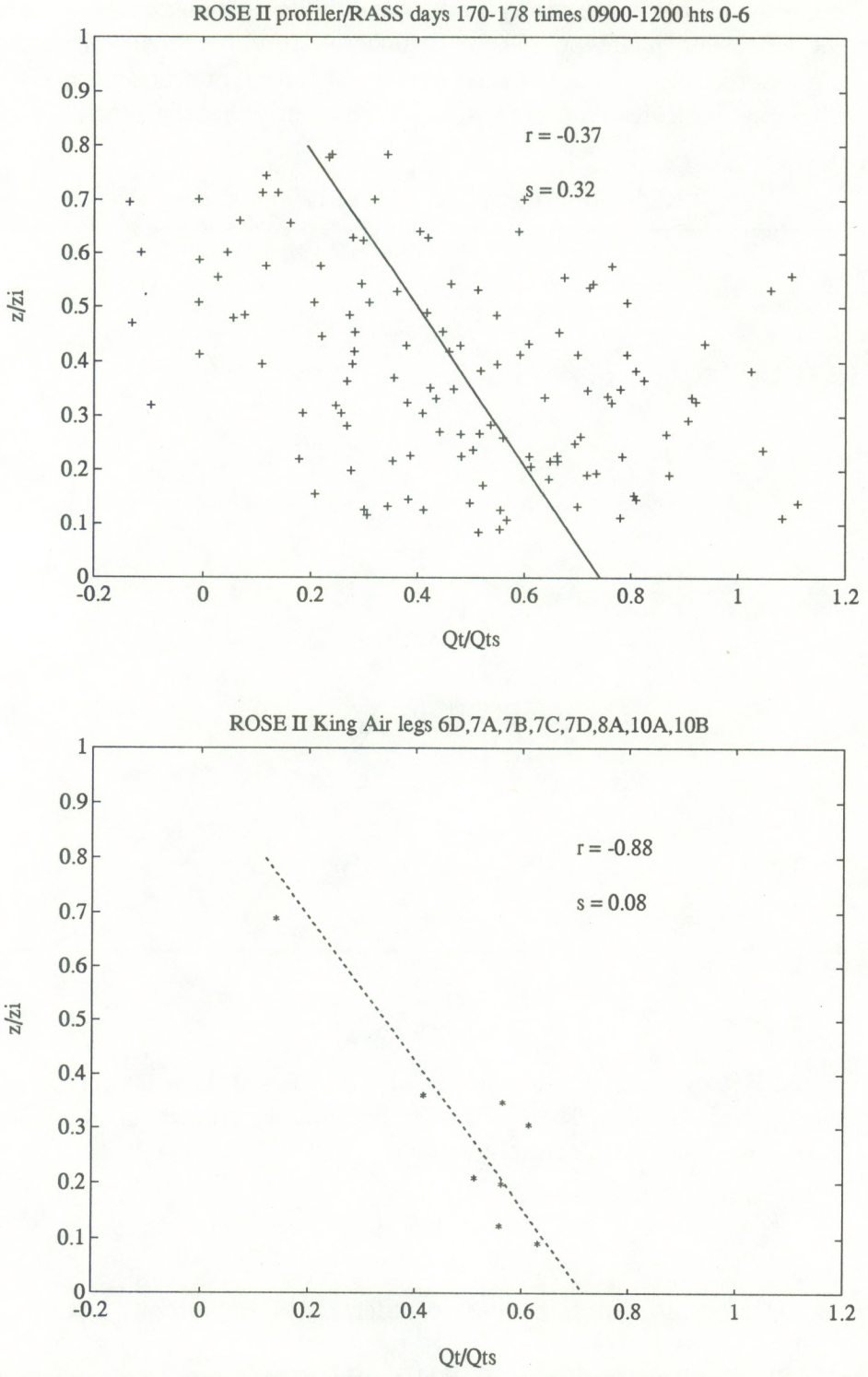

Figure 6.10: Virtual temperature flux from profiler/RASS for 2h periods centered at each hour from 0900-1200 CST (top) and for 8 King Air flight legs (bottom). Measurements below $0.8z_i$ are shown. See text for details.

Figure 6.12 shows the ±1σ uncertainty envelopes of the fits themselves, derived from the uncertainties of the slope and intercept. These fit uncertainties should not be confused with the uncertainty of the measurement. The substantial overlap of the ±1σ uncertainties of the fit, even at the higher scaled heights, indicates that there is some probability that the profiles do not differ.

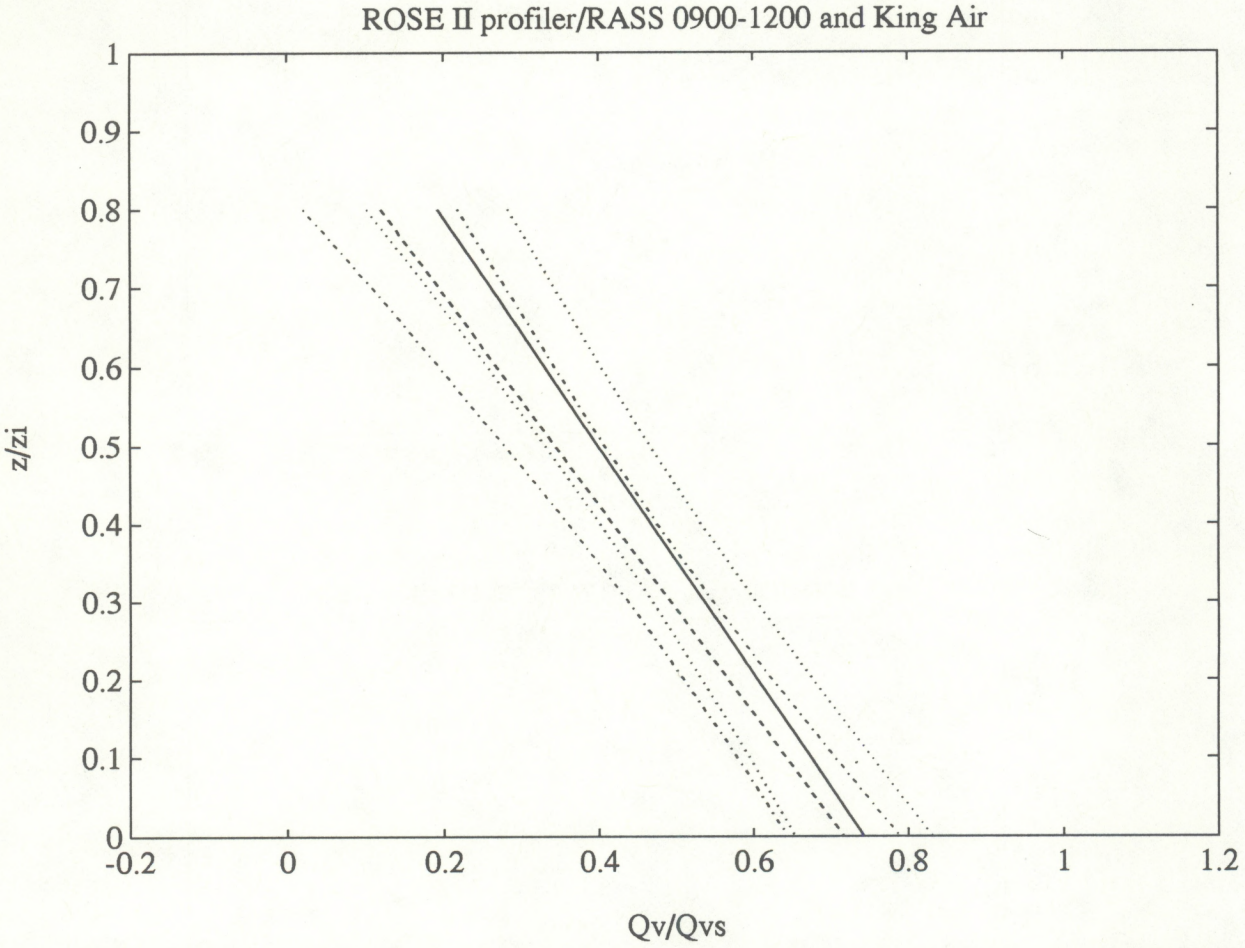

Figure 6.12: Fitted lines with ±1σ uncertainties of fits (derived from uncertainties of slope and intercept) shown. Solid: profiler/RASS fit. Dashed: King Air fit. Dotted: profiler/RASS uncertainty. Dash-dot: King Air uncertainty.

6.3.4 Uncertainties and differences between profiler/RASS and aircraft fluxes

The profiler/RASS technique measures virtual temperature fluxes that agree well (generally within the limits of sampling uncertainty) with aircraft measurements and with a simple model (equation 2.7). There is considerable scatter in the results, however, and there appear to be systematic differences between the profiler/RASS and aircraft measurements, and between those

measurements and the surface flux measurements.

The two techniques sample the atmosphere very differently. The profiler/RASS samples a vertical stack of volumes directly over the site for a time period varying (in these comparisons) from 2 to 14 (non-contiguous) hours. The aircraft samples a virtually one-dimensional path covering 50-100 km in 10-20 minutes. Both sampling methods have theoretical and practical problems. Under the light wind conditions present during this experiment, the profiler almost certainly does not sample a frozen turbulence field advected by the mean wind. Instead, it samples a turbulence field that is evolving on a time scale comparable to the time scale for advection of large eddies. In addition, any tendency for thermals to form preferentially over terrain inhomogeneities will result in a flux measurement that is not representative of the area average flux. The aircraft flight path passes over terrain that differs from that around the profiler site, including occasional roads and buildings, bringing into question the representativeness of the aircraft measurement. The single-point surface flux measurement used for scaling also may not be representative of the area as a whole.

The uncertainty due to sampling of turbulence was discussed in section 2.5. Tables 6.4 and 6.5 give information about the expected errors in these measurements calculated from equations 2.14 and 2.15. Table 6.4 shows the mean wind speed, normalized height, and variances of temperature and vertical wind observed on each flight leg. Table 6.5 shows the results of using those parameters to compute the integral scales in space (for the aircraft measurement itself) and in time (for the fixed profiler observation, assuming Taylor's hypothesis holds.) Table 6.5 also shows the relative error expected for the aircraft leg and for a 2 h average profiler/RASS measurement. We note again that this is the relative uncertainty due to sampling of the turbulence, not including any contribution from instrumental errors.

Comparing the relative uncertainty estimates for the profiler in table 6.5 with the relative differences between the profiler/RASS and King Air measurements in table 6.2 (individual day comparisons), we observe that the difference is less than the relative uncertainty for the profiler for all legs except 10A. There is a correlation between the differences and the uncertainty, legs with large uncertainties tending to have large differences. If the instrumental error were as large as the sampling uncertainty, the observed differences would be larger. The random instrumental error in the profiler/RASS must therefore be less than the sampling uncertainty. The instrumental error is certainly less than 40% and probably less than 30% when averaged over 2 h.

Table 6.4: Measured wind speed, height/PBL height, temperature variance, and vertical wind variance for King Air flight legs.

Leg	Wind speed, m/s	$\frac{z}{z_i}$	$\overline{T_v^2}$	$\overline{w^2}$ m^2s^{-2}
6D	2.1	0.13	0.06	0.82
7B	2.0	0.36	0.09	0.81
7C	2.0	0.20	0.05	0.95
8A	4.9	0.31	0.37	0.85
10A	1.2	0.35	0.06	0.64
10B	0.7	0.21	0.19	1.19

Table 6.5: Integral scales in space and time (using Taylor's hypothesis) and relative uncertainties ($\pm 1\sigma$) for King Air flight legs and surrounding profiler 2 h averages. Integral scales are computed from equation 2.10 and relative uncertainties are computed from equations 2.14 and 2.15.

Leg	Integral scale in space (λ), m	Integral scale in time (τ), s	Relative uncertainty for flight leg	Relative uncertainty for profiler
6D	102	48	0.12	0.28
7B	80	40	0.20	0.49
7C	79	41	0.11	0.30
8A	65	13	0.22	0.41
10A	51	42	0.18	0.43
10B	76	102	0.14	0.69

Estimating the sampling uncertainty for the multi-day average comparison of section 6.3.2 and table 6.3 is somewhat more complex. The estimate is based on the observation that the 7 days have roughly similar turbulence parameters, and the assumption that the parameters derived from the flight legs are representative of those days. We then compute a mean sampling uncertainty from the mean

values. For the six flight legs the mean integral scale in time is 48 s and the mean relative uncertainty for the aircraft is 0.16. Taking the profiler averaging time to be 14 h (7 days of 2 hour periods) for the multi-day comparison, the relative uncertainty for the profiler/RASS due to sampling is 0.19. The sampling uncertainty can be thought of as being based on the requirement to sample a reasonable number of the flux-carrying eddies, and since more eddies are represented in the 14 h composite average, the assumption of 14 h sampling time is reasonable. Alternatively, we could consider that we are estimating a mean sampling uncertainty for each 2 h period, then dividing by the square root of the number of samples (7) in the average to arrive at the uncertainty of the average. Either process yields the same numerical result. The standard deviation of the relative difference between the 7-day average profiler/RASS flux measurement and the flight legs is 0.14. This comparison also depends on the uncertainty of the surface flux measurement, which is estimated at 10-20% (D.L. Matt, private communication). Since it does not contribute to the observed uncertainty, the random instrumental error in the profiler/RASS flux measurement must be no more than 15% when averaged over 14 h.

The comparisons above show that the profiler/RASS measures 10-25% more flux than the aircraft in the lowest two profiler range gates (150 m and 250 m), depending on how the comparison is made. When the measurements are scaled and extrapolated by least-squares fitting (figure 6.11) the profiler/RASS and aircraft profiles agree extremely well at the surface. The disagreement increases slightly with height. The apparent systematic difference between the profiler/RASS flux measurement and the King Air measurement may be due to the differences in sampling (line vs. volume, short vs. long time, and horizontal inhomogeneity) mentioned above (Desjardins et al., 1992). In both the multi-day average (table 6.3) and the fitted profile (figure 6.11) comparisons, the mean difference is less than the standard deviation of the difference, and so the mean difference may not be significant.

The profiler/RASS and aircraft both measure less flux than the surface instrument (figure 6.10). The discrepancy is 25% of the surface value (figure 6.11). Part of the discrepancy is accounted for by the scales measured. Flux on scales less than about 100 m is not measured by either the profiler/RASS or the comparable block-averaged aircraft results. If all available scales (up to 10 Hz) are retained in the aircraft measurement, the extrapolated value at the surface is increased from 0.72 to 0.83 (relative to the surface flux), so the neglect of small scales results in approximately a 15% underestimate. This is about half of the apparent discrepancy. The remaining disagreement may again be due to sampling differences between the measurements, or to some other unknown cause. One possible cause is a +15% correction introduced in the surface sonic anemometer data because of wind-tunnel calibration done after the experiment (D.L. Matt, private communication). If this correction were not present, the agreement between the profiler/RASS and aircraft measurements and the surface measurement would be improved significantly.

A number of studies from the First ISLSCP Field Experiment (FIFE) relate to the comparison of aircraft and surface flux measurements. The FIFE experiment was conducted in a continental grassland. Sensible heat flux comparisons from FIFE are most comparable to the virtual temperature flux under discussion. Using sensible heat flux measurements from two aircraft, the National Research Council of Canada Twin Otter and the University of Wyoming King Air, Kelly et al.

(1992) show a disagreement of 30% with the flux measured by surface instruments when the aircraft fluxes are extrapolated to the surface. The authors attribute half of the disagreement to undersampling of high frequencies. The cutoff frequencies were lower than those of the NCAR King Air, so this effect should be less important in the current study. Betts et al. (1992) compare a different set of fluxes measured by the Twin Otter during FIFE and find an 18% underestimate, which they explain by the undersampling of both high and very low frequencies. The FIFE studies used short (15 km) flight legs, while the current study uses much longer (50-100 km) legs, and should not have undersampled low frequencies. Another FIFE study by Grossman (1992) using the same NCAR King Air as the current study observed no systematic difference between the aircraft sensible or latent heat fluxes extrapolated to the surface and the fluxes measured at the surface, but only 2 days were studied. It is also worth noting that the surface flux measurements in FIFE were averages over a large number of sites and that the differences between individual sites were substantial (Smith et al., 1992). These large differences are another indication that the single surface measurement site used in the current study may not be representative of the entire area.

6.3.5 Comparison to sensible and latent heat fluxes

In the light of the discussion of terminology in the introduction, it is interesting to compare the sensible, latent, and virtual heat fluxes measured by the aircraft. The profiler/RASS measures virtual temperature directly, but the aircraft measures temperature and humidity separately, so the sensible and latent heat fluxes (equation 2.3) can be calculated. Table 6.6 shows these fluxes for the eight flight legs of table 6.1.

Table 6.6: Sensible, latent, and virtual heat fluxes for King Air flight legs. Units are Wm^{-2}.

Leg	Sensible	Latent	Virtual
6D	65	512	104
7A	16	103	24
7B	33	508	72
7C	68	446	102
7D	100	295	123
8A	87	210	103
10A	36	375	64
10B	89	362	116

The latent heat flux is considerably larger than the sensible heat flux for each leg. This reflects the high humidity of the experiment environment. The difference between the sensible heat flux and the virtual heat flux varies from 20% to 115% of the sensible heat flux, so the virtual heat flux is not a good estimate of the sensible heat flux in this humid environment.

6.4 Boundary layer height and entrainment

The depth or height of the atmospheric boundary layer is a fundamental parameter for any boundary layer study or model, either physical or chemical. In the current study, it is needed for scaling of the virtual temperature flux. Traditionally, the boundary layer height has been measured by acoustic sounders (sodar), towers, aircraft, or radiosondes. Sodar and towers work well for low boundary-layer heights at night or during strong subsidence episodes. Aircraft or radiosondes can measure convective boundary layer (CBL) height, but aircraft are expensive and provide only occasional measurements. Sondes, because they measure at only one point in space and time, produce measurements that are likely to be unrepresentative. If the sonde rises through a thermal, it will measure a high inversion, while if it flies through a downdraft area it will measure a low inversion.

The boundary layer profiler can provide continuous measurements of CBL height with very good time resolution and good height resolution. These measurements were pioneered by White et al. (1991a,b). The work discussed in this section covers a larger number of convective cases and goes on to discuss the information that the profiler can provide about the degree of definition of the CBL top and the entrainment zone thickness.

The CBL height is deduced from the signal to noise ratio (SNR) recorded by the profiler. A clear-air radar such as the boundary layer profiler receives its return signal primarily from inhomogeneities of the radio refractive index. These inhomogeneities are characterized by the refractive index structure parameter C_n^2. The profiler SNR at a given range is directly proportional to C_n^2 (Ottersten 1969; VanZandt et al. 1978). Wyngaard and LeMone (1980) showed that C_n^2 peaks at the inversion atop a CBL due to mixing of relatively warm, dry air from above the boundary layer with cooler, more moist air below. Therefore, a peak in the range-corrected SNR indicates the CBL top z_i.

During ROSE II, the profiler collected a sample every 40 s, completing a cycle of all five beam positions every 200 s. SNR profiles from all beam positions are combined directly, since the error in height due to the 12° zenith angle is only about 44 m at a range of 2 km, well within the 100 m resolution of the profiler. The CBL height can be found automatically by two different algorithms. In the first, the peak SNR of each sample is found and then the median of the heights at which the peaks occur over some period is computed. Alternatively, the order can be reversed, taking the median of the SNR profiles first and then finding the height at which the peak occurs. The two algorithms give generally similar results, but the first (peak finding before median) produces slightly smoother time series of the CBL height and is used here. The median is used rather than the mean in order to give less weight to outliers, since no other data quality control is used. Contour plots of

the SNR can be used to find the CBL height by eye, and also indicate when the measurement is reliable and how well defined the CBL top is. The CBL height can be determined to within the profiler height resolution, which is 100 m in this experiment.

Four cases from the ROSE II experiment are shown in figures 6.13-6.16. For each day, the figure shows a contour plot of half-hour average range-corrected SNR from the profiler with the line of half-hour median peak SNR height superimposed. The minimum contour in each plot is 3 dB above the mean SNR over heights 150-550 m and times 1200-1600 CST, so the minimum contour shows a doubling of the SNR over the mean in the mixed layer during the afternoon. The contour interval is 2 dB. The lower plot in each figure shows virtual potential temperature (θv) and relative humidity (RH) for all radiosonde soundings between 0800 and 1600 CST on that day. The sonde launch times are indicated on the contour plot by asterisks, and the automatically determined CBL height from the nearest half-hour is plotted as a short horizontal line on the sounding profiles.

The CLASS rawinsonde system used has a specified accuracy of 0.5° C in temperature and 5% in relative humidity. The 5-mb interpolated data output was used for the comparisons presented here, so the height resolution is about 40 m in the boundary layer.

Figures 6.13 and 6.14 show results for 22 and 23 June 1992. On those days the CBL top was very well defined and z_i remained roughly constant after noon. The midday soundings show strong, sharp inversions with large $\Delta\theta_v$ over small Δz and abrupt drops in relative humidity at the CBL top. The air above the CBL was very dry. By the 1433 CST sounding on 23 June, the mixed layer had warmed enough to substantially erode the inversion.

The agreement between the CBL height as measured by the profiler and as measured from the sounding is excellent for these well-defined days. The profiler SNR peak tends to be somewhere in the middle of the inversion, near the height where the virtual potential temperature is equal to that at the surface, while the humidity peak from the sonde tends to indicate the inversion base.

In contrast to the previous two figures, figures 6.15 and 6.16 are from two days (19 and 25 June) when the CBL top was less well defined. The contours of profiler SNR are much more spread out, and the maximum SNR is less. The 0949 and 1205 CST soundings on 19 June (figure 6.15) show a weak but definite inversion, but the 1430 CST sounding does not show a definite inversion. On 25 June (figure 6.16) the inversion is strong (large $\Delta\theta v$) but gradual (large Δz.) The enhancements in radar SNR above 1500 m are probably due to the fair-weather cumulus clouds that were present on that day. Larger values of C_n^2 are expected in clouds because of increased turbulence within the cloud and enhanced mixing near cloud boundaries due to entrainment. The SNR measured by the radar may also be increased by scattering from cloud drops. In the presence of clouds, there is no commonly accepted definition of the boundary layer height. On both of these days the automatic CBL height finding algorithm produces height estimates that vary significantly from one half-hour to the next, and an estimate by eye from the contour plots differs from the automatic algorithm as well. However, estimating the CBL height from the soundings is also difficult on such days. The height estimates from the profiler are at least reasonable.

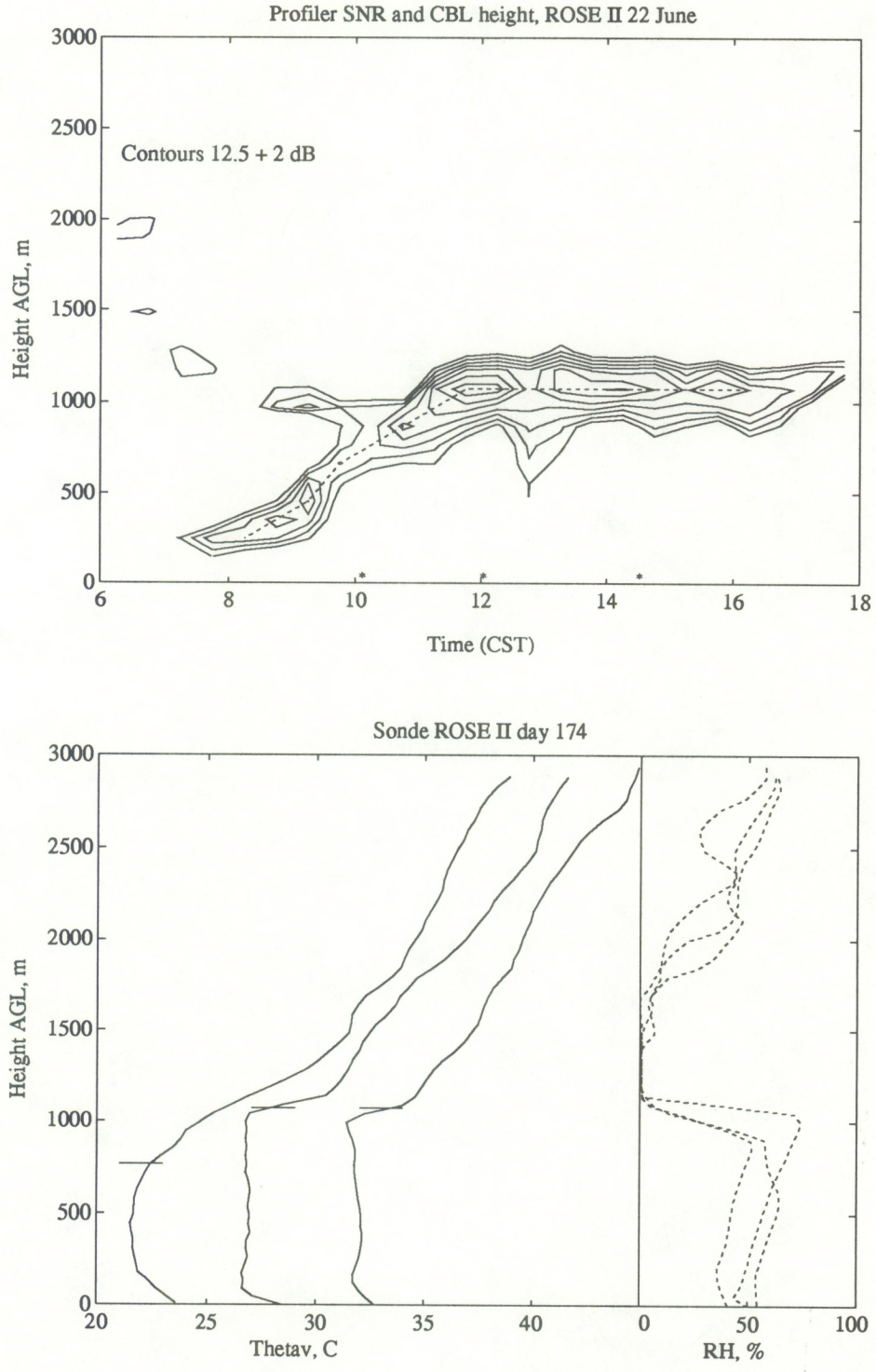

Figure 6.13: CBL height information for 22 June. Upper plot: Contours of profiler SNR and automatically determined CBL height (dashed). Lower plot: radiosonde profiles at launch times 1006, 1202, 1431 CST. Succeeding profiles are offset by 3°C.

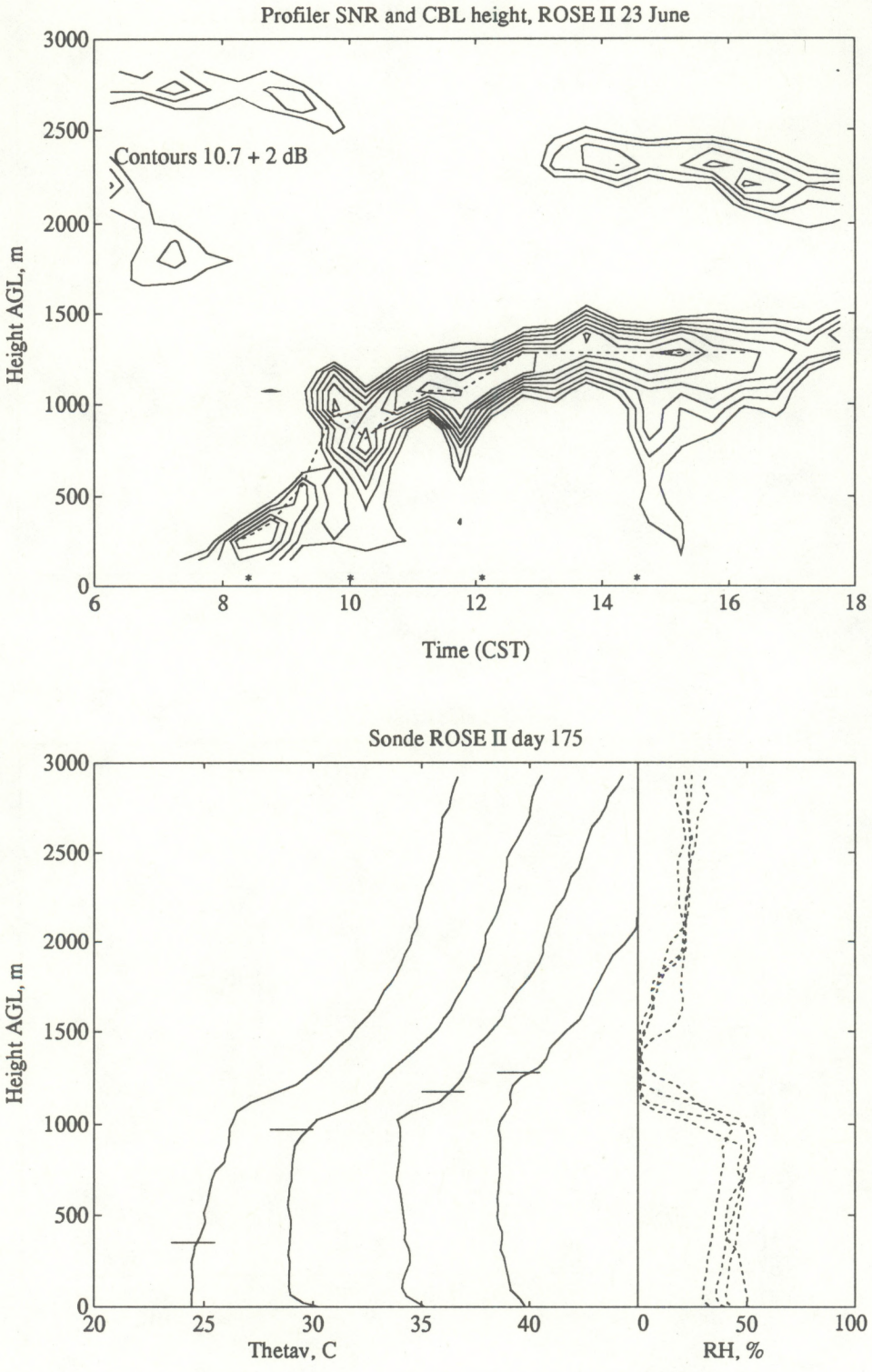

Figure 6.14: As figure 6.13 for 23 June. Four soundings are shown, launched at 0824, 1000, 1206, and 1433 CST.

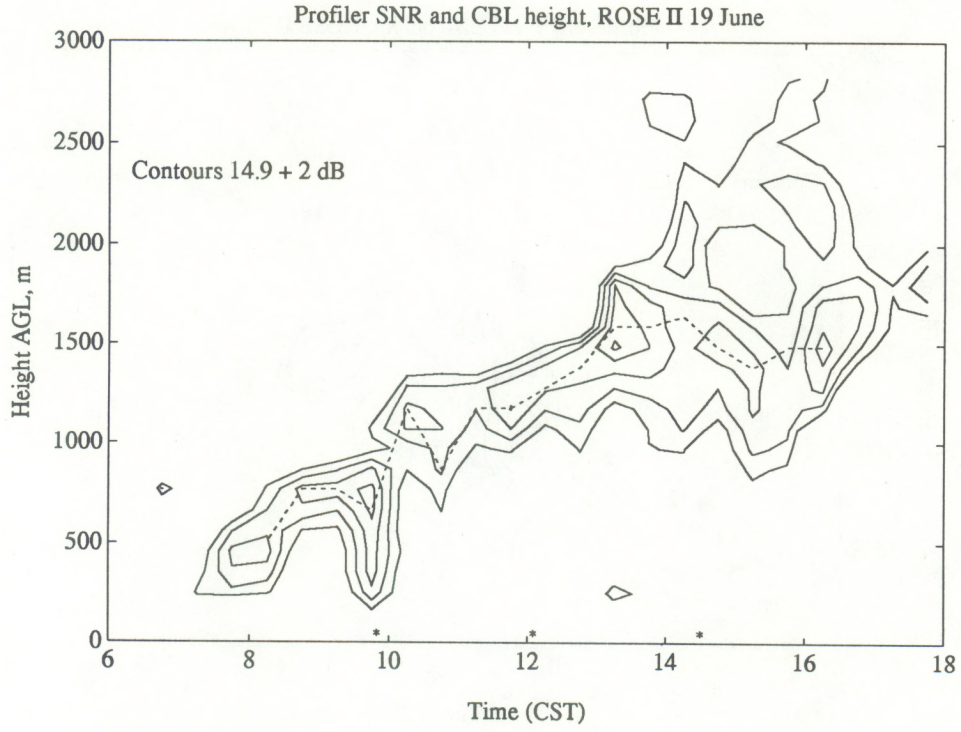

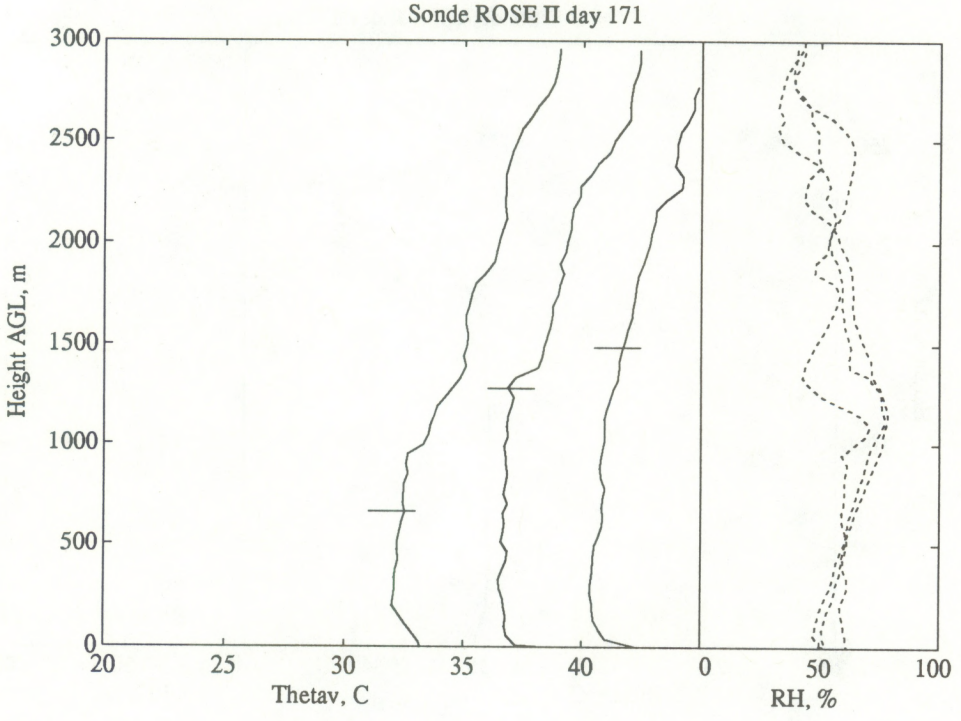

Figure 6.15: As figure 6.13 for 19 June. Three soundings are shown, launched at 0949, 1205, and 1430 CST.

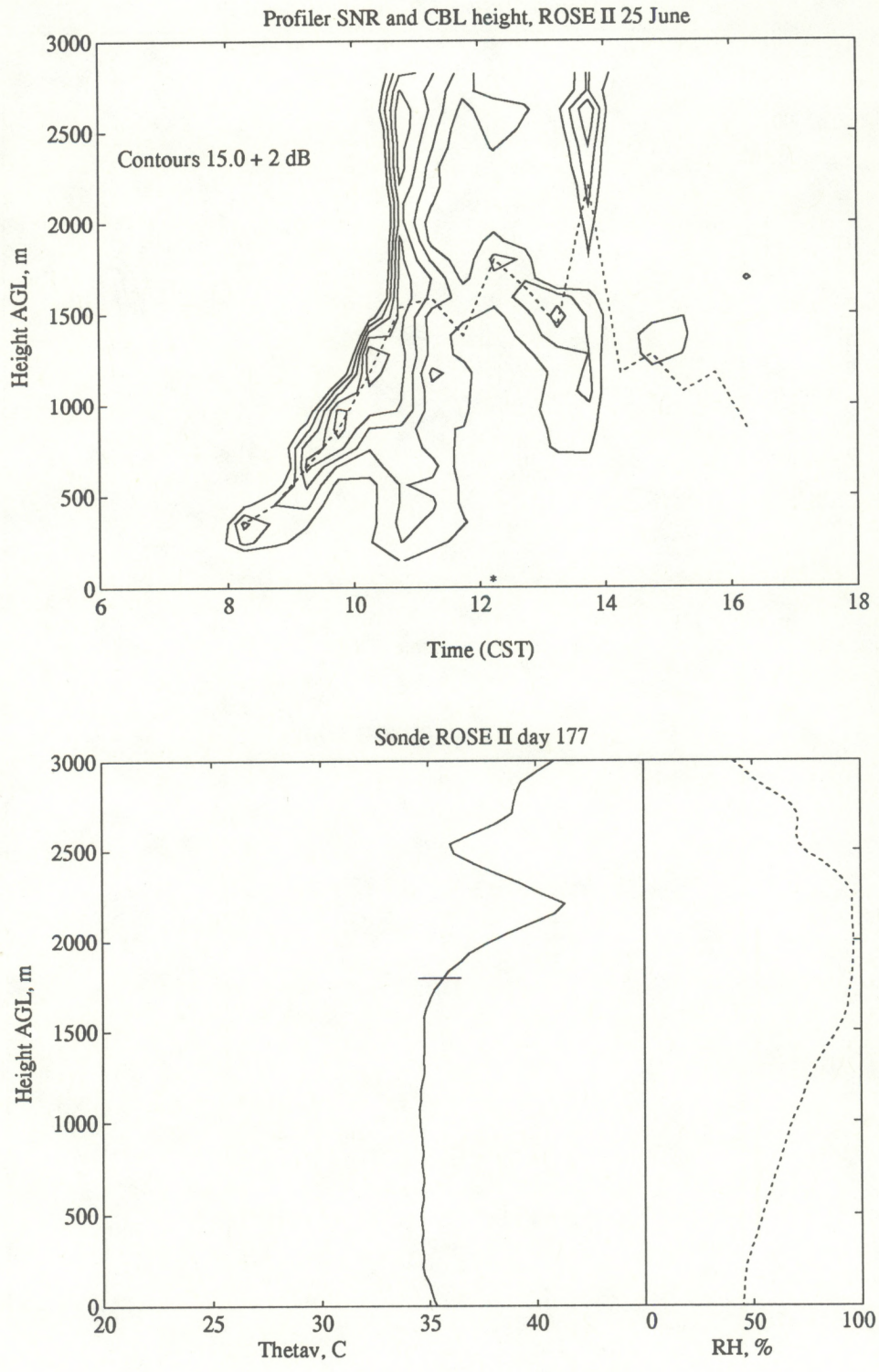

Figure 6.16: As figure 6.13 for 25 June. One sounding is shown, launched at 1212 CST.

Synoptic-scale subsidence appears to be the primary controlling mechanism of the strength of the inversion and therefore the boundary layer height. Subsidence causes significant drying (in relative humidity) above the boundary layer, strengthening the inversion, and also directly suppresses boundary layer growth. The CBL height is not controlled by the surface buoyancy flux in these examples, and in fact the highest surface buoyancy flux (figure 6.5) occurs on 23 June when the CBL height is rather low (1200 m AGL), and the lowest flux of the four days occurs on 19 June when the CBL reaches 1600 m AGL.

In addition to the boundary layer height, we would like to know the thickness of the entrainment zone. The spread of the profiler SNR contours provides an indication of the entrainment zone thickness. In the well-defined cases (figures 6.13 and 6.14) the thickness of the temperature inversion in the midday soundings can be measured, and is about 100 m. Note that the height resolution of the (5 mb interpolated) sonde record is approximately 50 m. We might take the thickness of the entrainment zone to be only the thickness of the temperature inversion, 100 m in the well-defined cases. Using that definition, we measure in figures 6.13 and 6.14 a corresponding decrease in profiler SNR of 2-3 dB at ±100 m from the maximum SNR at its peak.

It would be reasonable to argue, however, that all of the enhancement of SNR above the mean background level is due to entrainment. If we follow this line of reasoning, then the entire region within the contours in figures 6.13-6.16 was affected by entrained air. The well-defined cases have stronger gradients of temperature and mixing ratio in the inversion than the poorly-defined cases. Entrainment-induced mixing across these gradients produces larger temperature and humidity fluctuations, and thus higher peak values of SNR. Strong gradients also constrain air parcel movements more tightly, so that, in general, we expect the effects of entrainment to be more localized in height, as evidenced by the tight packing of contours in figures 6.13 and 6.14. The opposite is true for the poorly defined cases, where the gradients are weaker but parcels can move more freely over a larger height range. In these cases (figures 6.15 and 6.16), the peak values of SNR are smaller, but the contours surrounding the peaks are not as closely packed.

In both the well-defined and poorly-defined cases, we see a few regions of large SNR values in the mixed layer. These local increases in SNR may indicate episodes of deep entrainment, which creates strong horizontal and vertical gradients of humidity and temperature and therefore enhances reflectivity.

The measured mean SNR in the mixed layer is lower in the well-defined cases than in the poorly-defined cases. White et al. (1991a) observed a moderate correlation between the mean water vapor mixing ratio and C_n^2. Since the well-defined cases shown here have considerably lower mixing ratio (8 g/kg) than the poorly-defined cases (13-14 g/kg), the observed difference in mean SNR may be a reflection of the change in background humidity.

6.5 Momentum flux comparison

The vertical turbulent flux of momentum is defined by equation 2.9. It is calculated from the profiler and aircraft data as described in chapter 4. In this section, we compare the profiler and aircraft measurements of momentum flux.

The vertical flux of horizontal momentum calculated from the King Air and from the profiler is presented in figures 6.17 and 6.18. For the profiler, the dashed line shows the flux on scales greater than the resolution cell (equation 4.2) and the solid line shows the flux on all scales, the sum of the results from equations 4.2 and 4.3. The asterisks are the King Air measured flux on scales greater than 1 s and the pluses are the King Air measured flux on all scales. The asterisks should compare to the dashed line and the pluses to the solid line. The fluxes measured by the profiler were computed for two-hour periods centered every hour and then averaged over all days having surface data, so each point represents an average over 5 to 7 days of 2 h periods. Figure 6.17 shows the wind-aligned momentum flux, that is, the flux in the direction of the surface wind for each two-hour period. Figure 6.18 shows the momentum flux in the crosswind direction (+90° from the surface wind direction). The upper panel of each figure shows the flux computed from the clear-air velocities, while the lower panel shows the flux computed from the acoustic velocities.

The momentum fluxes measured by the King Air are small, as would be expected in the light winds prevalent at ROSE II. The fluxes measured by the profiler from the acoustic velocities are better behaved than those from the clear-air velocities. The wind-aligned acoustic momentum flux (figure 6.17 lower panel) is in rather good agreement with the King Air measurements. The other profiler measurements do not show good agreement with the King Air measurements, and often show unreasonably large magnitudes.

The sampling uncertainties for the momentum flux measurements, computed from equation 2.15, are about 0.03 m^2s^{-2} for the King Air measurements, but this represents a large relative uncertainty of approximately 50% due to the small values of the flux. The sampling uncertainties for 2 h profiler measurements derived from the uncertainty in measurement of the variances (equation 4.4) are approximately 0.2 m^2s^{-2} (for the total flux). The sampling uncertainty accounts for much of the poor quality of the profiler measurements. Larger discrepancies may be due to uncertainties in the instrument and/or in the technique. Because of the combination of uncertainties in the calculation, and because both large and small scale calculations contribute to the total flux estimate, an uncertainty of 0.1 m^2s^{-2} in each of the variances and mean square spectral widths will produce an uncertainty in the total flux estimate of 0.35 m^2s^{-2}. If such errors are instrumental, they may not be reduced by averaging. The observation that the acoustic velocities yield a better flux estimate, at least in the wind-aligned case, suggests that the cleaning algorithms (chapter 4) are not completely effective in removing contaminated data. The acoustic velocities are much less subject to contamination than the clear-air velocities, but they also give poorer height coverage.

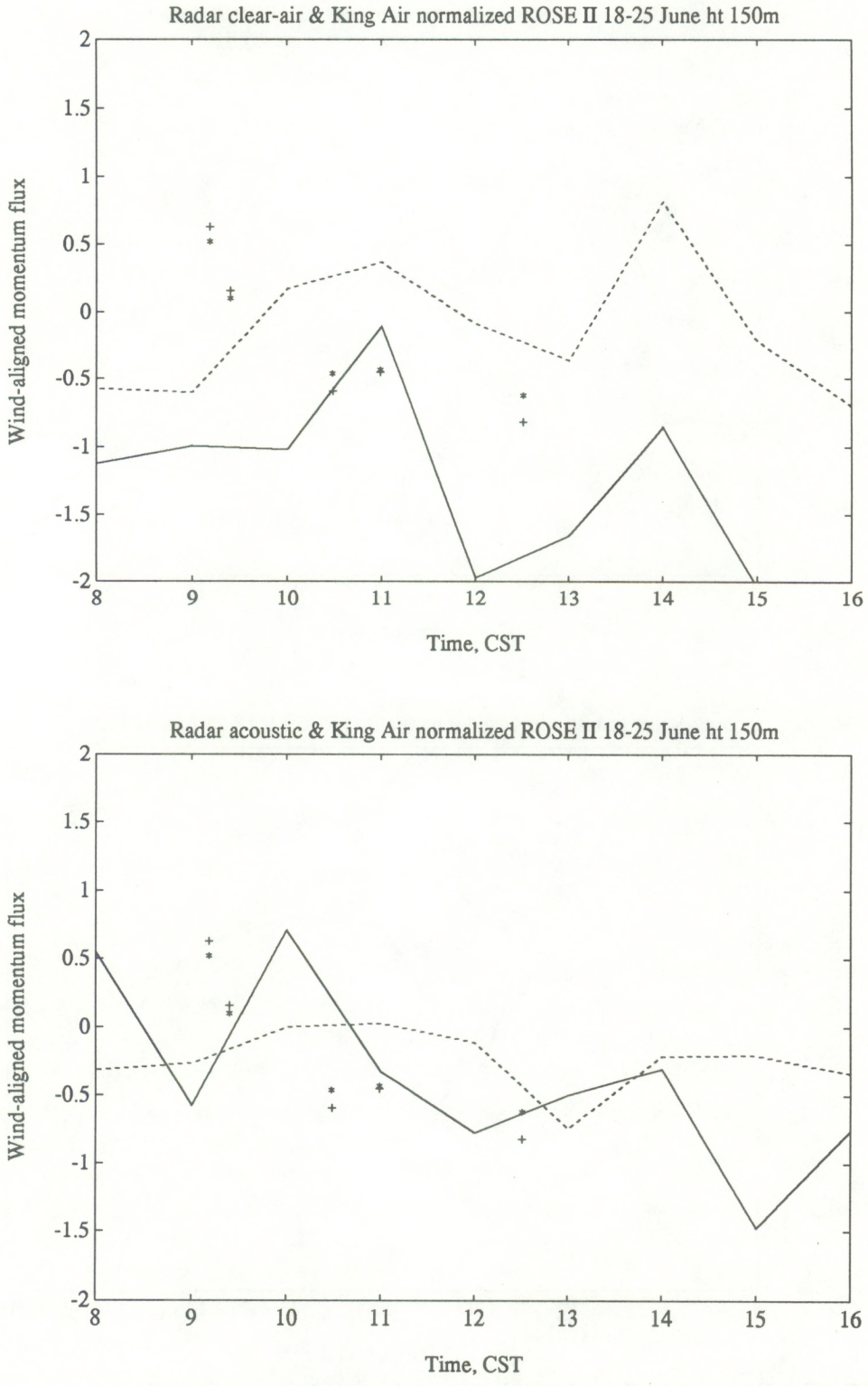

Figure 6.17: Comparison of wind-aligned momentum flux measured by profiler and King Air. Upper plot from clear-air, lower from acoustic velocities. See text for description of symbols.

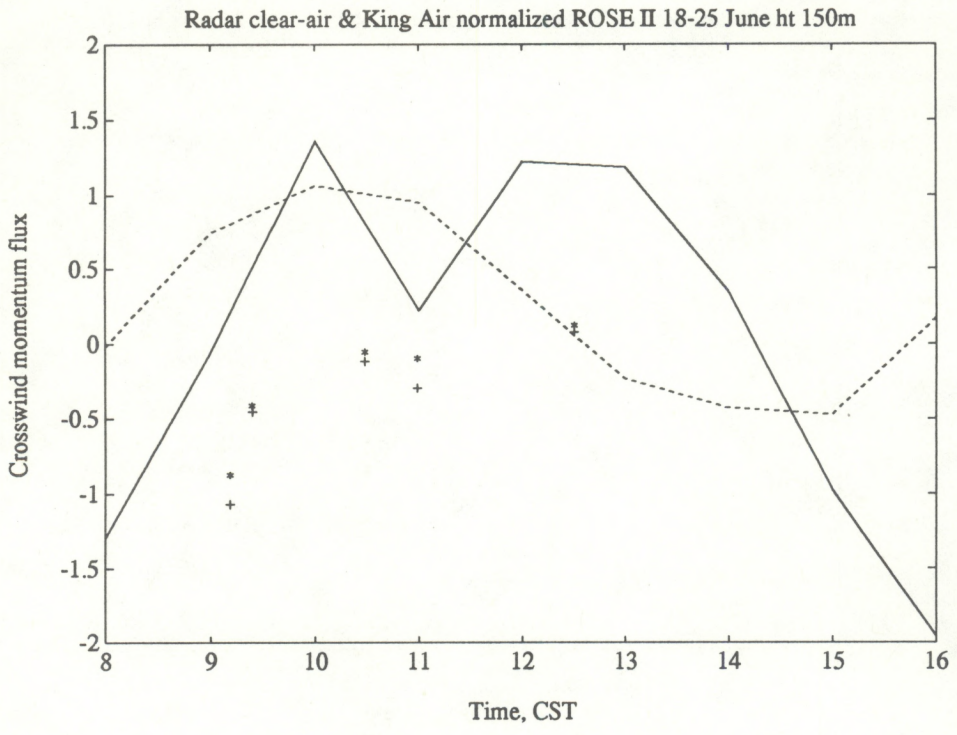

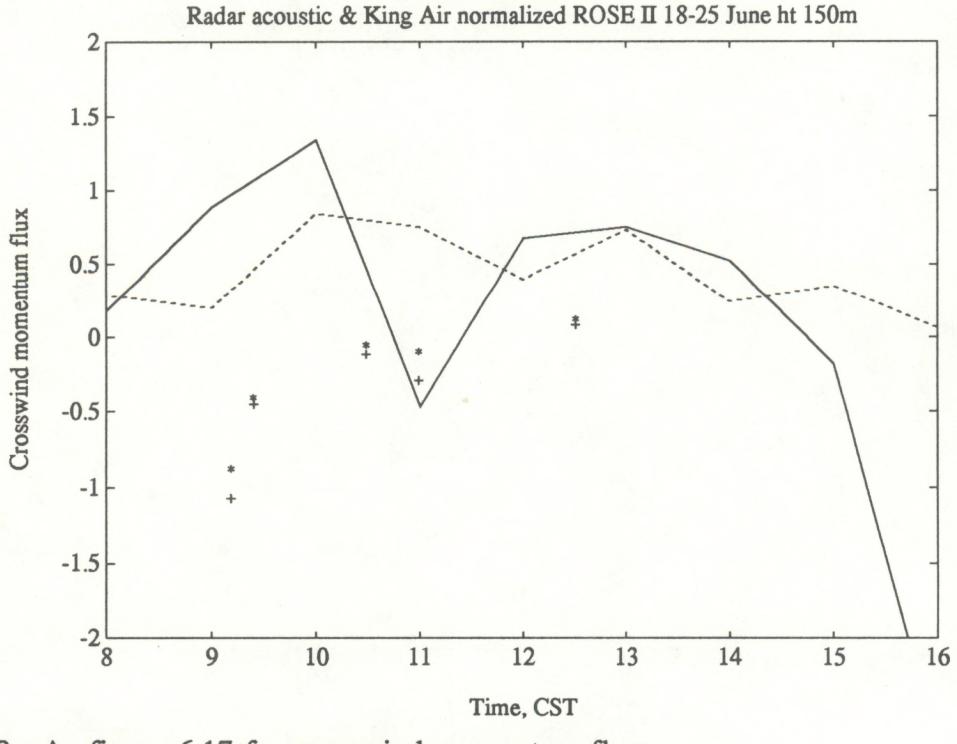

Figure 6.18: As figure 6.17 for crosswind momentum fluxes.

6.6 Summary of ROSE II results

The ROSE II experiment yielded good data for comparisons of the profiler/RASS heat flux to fluxes measured by aircraft and surface instruments. The data and weather conditions also lent themselves to an interesting and fruitful exploration of the potential for boundary layer height and entrainment zone measurements. The momentum flux results were not encouraging, probably due to light winds. The conclusions from the entire body of work are summarized in chapter 7.

7. Conclusions

We have studied the measurement of heat and momentum fluxes with the boundary layer profiler/RASS, and can now state some conclusions. The specific contributions of this work are a robust evaluation of virtual temperature flux measurements, including error estimates; software development and evaluation of the simultaneous measurement of winds and virtual temperature by RASS; development of the statistical cleaning algorithm for profiler data; and development and evaluation of automatic boundary layer height determination from the profiler data.

The profiler/RASS can measure virtual temperature flux in the convective boundary layer with results that compare well with aircraft and surface measurements and with model results. The profiler/RASS has several advantages over those other techniques. The primary advantage is that profiler/RASS flux measurements are continuous in time and height. The density of coverage in time and space is much better than with any other technique except the use of instrumented towers. A profiler/RASS, however, can be transported from one site to another relatively easily, is much less expensive than a tower several hundred meters high, and is not subject to severe siting constraints as towers are. In addition, the profiler/RASS provides mean temperatures to at least 600 m, mean winds to at least 2 km (much higher than towers), and information about the height of boundary layers that exceed tower heights, while also providing fluxes. Compared to surface flux instruments, the profiler/RASS flux measurements are more representative of the average characteristics of the surrounding area because the sample volume is larger and higher above the surface. On the other hand, the sampling uncertainty is less for surface measurements.

The precision of profiler/RASS flux measurements is limited primarily by the sampling uncertainty of the turbulence itself (equation 2.14). This is true for any instrument that is fixed in place and depends on the wind to advect the turbulence past its sample volume. The averaging time required for a given accuracy depends on the wind speed and the boundary layer height (through the integral scale of the turbulence). The maximum averaging time is limited by diurnal or synoptic changes in conditions. Longer effective averaging times can be achieved by making composites of several periods with similar conditions, and by using scaling (normalization) to remove some of the variation.

We can estimate the instrumental uncertainty of the profiler/RASS for heat flux measurements by observing that the observed uncertainty is less than the expected sampling uncertainty, and that therefore the instrumental uncertainty must also be less than the sampling uncertainty. The instrumental uncertainty is certainly less than 40% and probably less than 30% when averaging over 2 hours, and is no more than 15% when averaging over a composite of 14 hours.

This work has not established the feasibility of making momentum flux measurements with the profiler. This needs to be explored further in more favorable conditions, with stronger winds or smaller diurnal variation.

The statistical data quality control techniques devised for this study are adequate for heat flux

calculations. Some refinements to these techniques may be possible. For example, it may be better to assume a lognormal distribution for the spectral width and therefore use a multiplicative rather than additive limit. Smoothing the filter limits over several heights might also yield a small improvement.

Determination of the boundary layer height from the profiler SNR produces results that compare well with sonde measurements, but the profiler has the considerable advantage of providing a continuous record. The result is also likely to be more representative of the average height than sonde results. More exploration is needed to learn how to use the wealth of information that the profiler provides about the evolution and structure of the entrainment zone.

A boundary layer profiler/RASS is a very useful instrument when deployed alone, but is even more useful when deployed with a suite of other instruments. Basic surface meteorological instruments (wind, temperature, and humidity) can provide perspective for interpreting the profiler results and extend wind and temperature profiles to the surface. A sonic anemometer can provide surface fluxes for scaling and enable the user to make composite averages to reduce sampling uncertainty. A laser ceilometer could provide continuous measurements of cloud base height and thereby assist in interpreting the return signal profile from the profiler. Radiosonde soundings can provide calibrated humidity profiles, which also assist in interpreting the vertical structure of the boundary layer.

Acknowledgements

Many people contributed to the work described herein. First, and most important, I thank Dr. Kenneth Gage and the other members of the Tropical Dynamics and Climate Group of the NOAA Aeronomy Laboratory, especially David Carter and Warner Ecklund, for providing the environment and equipment to do this work. Thanks are also due to Dr. Fred Fehsenfeld for organizing and troubleshooting the ROSE II experiment, and to Dr. Michael Trainer, and Dr. Stuart McKeen for their help with sonde flights and discussions of the ROSE II results. Dr. Thomas VanZandt was always available to talk about this work, and gave wise and timely counsel on papers. All the members of the Aeronomy Laboratory deserve thanks for providing a pleasant environment that was highly conducive to good scientific work.

Dr. Susan Avery of the University of Colorado gave much useful advice.

Several people from other organizations provided concrete assistance in carrying out the experiments. Dr. Gregory Kok of NCAR provided the ROSE II aircraft data. The surface data from ROSE II were provided by Dr. Detleff Matt of the NOAA Air Resources Laboratory, Atmospheric Turbulence and Diffusion Division, Oak Ridge, Tennessee. Jim Jordan of the NOAA Wave Propagation Laboratory helped set up the profiler/RASS at ROSE II and provided the clutter fence. The Surface and Sounding Systems Facility of NCAR, under the direction of Dr. Walter Dabberdt, provided a CLASS sounding system for ROSE II in support of this research. Dr. Richard Strauch and Ken Moran of WPL allowed us to use the Platteville site.

Partial funding for this study was provided by the Department of Energy Atmospheric Radiation Measurement program. ROSE II was conducted in collaboration with the Southern Oxidant Study. This work was also supported in part by the National Science Foundation under grants ATM-8720797, ATM-9214657, and ATM-9214800.

References

Angevine, W.M., S.K. Avery, W.L. Ecklund, and D.A. Carter, 1993a: Fluxes of heat and momentum measured with a boundary-layer wind profiler radar - radio acoustic sounding system. *J. Appl. Meteor.*, **32**, 73-80.

Angevine, W.M., S.K. Avery, and G.L. Kok, 1993b: Virtual heat flux measurements from a boundary-layer profiler-RASS compared to aircraft measurements. *J. Appl. Meteor.*, **32**, 1901-1907.

Angevine, W.M., and W.L. Ecklund, 1993: Errors in radio acoustic sounding of temperature. *J. Atmos. Ocean. Technol.*, in press.

Angevine, W.M., W.L. Ecklund, D.A. Carter, K.S. Gage, and K.P. Moran, 1994: Improved Radio-Acoustic Sounding Techniques. *J. Atmos. Ocean. Technol.*, **11**, 42-49.

Arya, S.P., 1988: *Introduction to micrometeorology*. San Diego, Academic Press.

Betts, A.K., R.L. Desjardins, and J.I. MacPherson, 1992: Budget analysis of the boundary layer grid flights during FIFE 1987. *J. Geophys. Res.*, **97**, 18,533-18546.

Desjardins, R.L., P.H. Schuepp, J.I. MacPherson, and D.J. Buckley, 1992: Spatial and temporal variations of the fluxes of carbon dioxide and sensible and latent heat over the FIFE site. *J. Geophys. Res.*, **97**, 18,467-18476.

Ecklund, W.L., D.A. Carter, and B.B. Balsley, 1988: A UHF wind profiler for the boundary layer: Brief description and initial results. *J. Atmos. Ocean. Technol.*, **5**, 432-441.

Friehe, C.A., R.L. Grossman, and Y. Pann, 1986: Calibration of an airborne Lyman-alpha hygrometer and measurement of water vapor flux using a thermoelectric hygrometer. *J. Atmos. Ocean. Technol.*, **3**, 299-304.

Gage, K.S., 1990: Radar observations of the free atmosphere: Structure and dynamics. *Radar in Meteorology*, D. Atlas, ed., Amer. Meteorol. Soc., Boston.

Gal-Chen, T., M. Xu, and W.L. Eberhard, 1992: Estimations of atmospheric boundary layer fluxes and other turbulence parameters from Doppler lidar data. *J. Geophys. Res.*, **97**, 18,409-18,424.

Grossman, R.L., 1992: Convective boundary layer budgets of moisture and sensible heat over an unstressed prairie. *J. Geophys. Res.*, **97**, 18,425-18,438.

Harris, C.M., 1966: Absorption of sound in air versus humidity and temperature. *J. Acoust. Soc. Am.*, 40, 148-159.

Kelly, R.D., E.A. Smith, and J.I. MacPherson, 1992: A comparison of surface sensible and latent

heat fluxes from aircraft and surface measurements in FIFE 1987. *J. Geophys. Res.*, **97**, 18,445-18,454.

Kropfli, R.A., 1986: Single doppler radar measurements of turbulence profiles in the convective boundary layer. *J. Atmos. Ocean. Tech.*, **3**, 305-314.

Lataitis, R.J., 1993: Theory and application of a radio-acoustic sounding system (RASS). NOAA Tech. Memo. ERL WPL-230, NOAA Environmental Research Laboratories, Boulder, CO.

Lenschow, D.H., and B.B. Stankov, 1986: Length scales in the convective boundary layer. *J. Atmos. Sci.*, **43**, 1198-1209.

Marshall, J.M., A.M. Peterson, and A.A. Barnes, Jr., 1972: Combined radar-acoustic sounding system. *Applied Optics*, 11, 108-112.

Masuda, Y., 1988: Influence of wind and temperature on the height limit of a radio acoustic sounding system. *Radio Sci.*, **23**, 647-654.

May, P.T., R.G. Strauch, and K.P. Moran, 1988: The altitude coverage of temperature measurements using RASS with wind profiler radars. *Geophys. Res. Lett.*, **15**, 1381-1384.

May, P.T., R.G. Strauch, K.P. Moran, and W.L. Ecklund, 1990: Temperature sounding by RASS with wind profiler radars: A preliminary study. *IEEE Trans. on Geoscience and Remote Sensing*, **28**, 19-28.

Moeng, C., 1984: A large-eddy-simulation model for the study of planetary boundary-layer turbulence. *J. Atmos. Sci.*, **41**, 2052-2062.

North, E.M., and A.M. Peterson, 1973: RASS, a remote sensing system for measuring low-level temperature profiles. *Bull. Amer. Meteor. Soc.*, 54, 912-919.

Ottersten, H., 1969: Atmospheric structure and radar backscattering in clear air. *Radio Sci.*, **4**, 1179-1193.

Priestly, C.H.B., 1959: *Turbulent transfer in the lower atmosphere.* Chicago, U. of Chicago Press.

Pennell, W.T., and M.A. LeMone, 1974: An experimental study of turbulence structure in the fair-weather trade wind boundary layer. *J. Atmos. Sci.*, **31**, 1308-1323.

Peters, G., H. Hinzpeter, and G. Baumann, 1985: Measurements of heat flux in the atmospheric boundary layer by sodar and RASS: A first attempt. *Radio Sci.*, **6**, 1555-1564.

Rabin, R.M., R.J. Doviak, and A. Sundara-Rajan, 1982: Doppler radar observations of momentum flux in a cloudless convective layer with rolls. *J. Atmos. Sci.*, **39**, 851-863.

Reid, I.M., 1987: Some aspects of Doppler radar measurements of the mean and fluctuating components of the wind field in the upper middle atmosphere. *J. Atmos. Terr. Phys.*, **49**, 467-484.

Smith, E.A., A.Y. Hsu, W.L. Crosson, R.T. Field, L.J. Fritschen, R.J. Gurney, E.T. Kanemasu, W.P. Kustas, D. Nie, W.J. Shuttleworth, J.B. Stewart, S.B. Verma, H.L. Weaver, and M.L. Wesely, 1992: Area-averaged surface fluxes and their time-space variability over the FIFE experimental domain. *J. Geophys. Res.*, **97**, 18,599-18622.

Stull, R.B., 1988: *An introduction to boundary-layer meteorology.* Kluwer, 666 pp.

VanZandt, T.E., J.L. Green, K.S. Gage, and W.L. Clark, 1978: Vertical profiles of refractivity turbulence structure constant: comparison of observations by the sunset radar with a new theoretical model. *Radio Sci.*, **13**, 819-829.

Vincent, R.A., and I.M. Reid, 1983: HF Doppler measurements of mesospheric gravity wave momentum fluxes. *J. Atmos. Sci.*, **40**, 1321-1333.

White, A.B., C.W. Fairall, and D.W. Thompson, 1991a: Radar observations of humidity variability in and above the marine atmospheric boundary layer. *J. Atmos. Ocean. Technol.*, **8**, 639-658.

White, A.B., C.W. Fairall, and D.E. Wolfe, 1991b: Use of 915 Mhz wind profiler data to describe the diurnal variability of the mixed layer. *Preprints, 7th Joint Conference on Applications of Air Pollution Meteorology with AWMA.* Published by AMS.

Wyngaard, J.C., 1986: Measurement Physics. In *Probing the atmospheric boundary layer*, D.H. Lenschow, ed., Boston, Amer. Meteorol. Soc.

Wyngaard, J.C., and M.A. LeMone, 1980: Behavior of the refractive index structure parameter in the entraining convective boundary layer. *J. Atmos. Sci.*, **37**, 1573-1585.

Wyngaard, J.C., 1992: Atmospheric Turbulence. *Annual Reviews of Fluid Mechanics*, **24**, 205-233.

Xu, M., and T. Gal-Chen, 1991: Study of the convective boundary layer dynamics using single Doppler radar measurements. Submitted to *J. Atmos. Sci.*

*U.S. GOVERNMENT PRINTING OFFICE:1994-573-013/89068